DEVELOPMENT OF TIN SELENIDE AND BISMUTH TELLURIDE BASED GRAPHENE COMPOSITES FOR THERMOELECTRIC APPLICATIONS

A Thesis

by

FIZZA USMANI

Submitted to Office of Graduate and Professional Studies of
Texas A&M University
in partial fulfillment of the requirements for the degree of

MASTER OF SCIENCE

Chair of Committee,	Ahmed Abdala
Co-Chair of Committee,	Ibrahim Galal Hassan
Committee Member,	Konstantinos Kakosimos
Head of Department,	Arul Jayaraman

December 2020

Major Subject: Chemical Engineering

ABSTRACT

Thermoelectric (TE) materials convert thermal energy into electrical energy, and vice versa. Bismuth telluride (Bi_2Te_3) is a widely studied thermoelectric material with a high figure-of-merit. Moreover, tin (IV) selenide ($SnSe_2$) has recently attracted attention as thermoelectric material due to its predicted excellent TE properties and high performance. Nevertheless, to enable the commercialization of such thermoelectric materials, further improvement in TE performance is required. Nanocompositing is an excellent approach to enhances the properties of TE materials. Graphene is an excellent filler for nanocomposites due to its excellent electrical, thermal, and mechanical properties. In this thesis, pure Bi_2Te_3 and $SnSe_2$ and their graphene nanocomposites were synthesized using hydrothermal and solvothermal solution-based methods. Detailed analysis of the chemical composition, the structural morphology, the mechanical and thermal properties, and thermal conductivity of the synthesized thermoelectric materials and their graphene nanocomposites were carried out.

The successful synthesis of $SnSe_2$ and Bi_2Te_3 was confirmed by XRD and XPS analyses. The nanosize of $SnSe_2$ with confirmed by XRD and found to ~ 31.5 nm. The incorporation of graphene into the structure of SnSe2 has improved the mechanical properties of the nanocomposites and decreased the already low thermal conductivity of pure $SnSe_2$ (0.60 W/m.K) to 0.41 W/m.K, corresponding to a 31.7% reduction with 0.5 wt.% graphene. This decrease in thermal conductivity is expected to enhance the TE properties of $SnSe_2$.

On the other hand, Bi_2Te_3 and Bi_2Te_3-graphene nanocomposites were also successfully synthesized. The powders were found to have good thermal stability, as evident by the TGA and DSC. The calculated average crystallite size for Bi_2Te_3 was 33 nm. The addition of graphene reduced the grain size of the nanopowders. Our results show that the addition of graphene to these systems can be a promising method of improving the thermoelectric performance of the materials, and the improvement of mechanical properties may aid in device fabrication for commercial applications.

DEDICATION

Dedicated to my family and friends for their unwavering support, love, patience, and strength, without which this project would not have been possible.

ACKNOWLEDGMENTS

I would like to thank and show my gratitude to my supervisor and committee chair, Dr. Ahmed Abdala, for his support on with master's thesis. His continuous guidance helped me through all my research work and brought this research into success. Alongside Dr. Abdala, I would also like to thank the co-chair of my committee, Dr. Ibrahim Hassan, and my committee member Dr. Konstantinos Kakosimos for their intuitive comments, inspiration, and encouragement.

I am infinitely thankful to Dr. Yiming Wubulikasimu at the Central Materials Facility at TAMUQ for assisting me in running multiple characterization tests while also teaching me the basics and backgrounds of these techniques. I would also like to thank Dr. Mohamed Hassan and Dr. Khaled Youssef at Qatar University, and the rest of the CLU staff for assisting me in various testing throughout my thesis.

Furthermore, I would like to thank Dr. Zafar Ghouri for his irreplaceable guidance and experimental support, from the first day and throughout my experimental research work. I am also thankful to Dr. Usman Chaudhry for his guidance and for facilitating the thermal conductivity measurements. I am in debt of gratitude to the members of the Materials Research Group, specially Omnya Abdalla and Mehamad Ali, for their guidance and their continuous support. This accomplishment would not be possible without them.

I would also like to thank my fellow students, the department faculty and staff at Texas A&M University, for giving me lasting memories of this part of my academic life.

Lastly, I would like to thank to my parents and my brother for their endless support, patience, and love.

NOMENCLATURE

Cp	Specific heat capacity
DOS	Density of states
EDS	Energy Dispersive X-ray Spectroscopy
GO	Graphene oxide
PF	Power Factor
k	Thermal Conductivity
k_L	Lattice thermal conductivity
SEM	Scanning Electron Microscopy
σ	Electrical Conductivity
TE	Thermoelectric
TGA	Thermogravimetric Analysis
XPS	X-ray Photoelectron Spectroscopy
XRD	X-Ray Diffraction
ZT	Figure-of-merit

CONTRIBUTORS AND FUNDING SOURCES

Contributors

This work was supervised by the thesis committee consisting of Professors Ahmed Abdala [advisor] and Konstantinos Kakosimos of the Department of Chemical Engineering and Professor Ibrahim Hassan [co-advisor] of the Department of Mechanical Engineering.

Dr. Yiming Wubulikasimu at the Materials Research Facilities at TAMUQ has carried the XRD, SEM, EDS, and XPS measurements. Dr. Mohammad Ibrahim at the Central Laboratories Unit at Qatar University has carried the DSC analysis. TEM characterization was performed at the Qatar Environment and Energy Research Institute under the supervision of Dr. Said Mansour.

All other work conducted for the thesis was completed by the student independently.

Funding Sources

Graduate study was supported by a graduate assistantship from Texas A&M University at Qatar, and by Qatar National Research Fund under NPRP10-0206-170366. Its contents are solely the responsibility of the authors and do not necessarily represent the official views of the QNRF.

TABLE OF CONTENTS

Page

ABSTRACT ii

DEDICATION iv

ACKNOWLEDGMENTS v

NOMENCLATURE vi

CONTRIBUTORS AND FUNDING SOURCES vii

TABLE OF CONTENTS viii

LIST OF FIGURES x

LIST OF TABLES xiii

1. INTRODUCTION 1

2. LITERATURE REVIEW 4

2.1 Thermoelectric Fundamentals 4
2.1.1 Thermoelectric Coefficients 4
2.1.2 The figure-of-merit, ZT 7
2.1.3 Thermal Conductivity 9
2.1.4 Power Factor 11
2.2 Thermoelectric Materials 11
2.2.1 Semiconductors 13
2.2.2 Ceramics 14
2.2.3 Polymers 14
2.3 Techniques for Improving Thermoelectric Performance 16
2.3.1 Nano-structuring 17
2.3.2 Nanocomposites 19
2.3.3 Doping and Alloying 21
2.4 Materials Studied 24
2.4.1 Bismuth Telluride 24
2.4.2 Tin Selenide 29
2.4.3 Graphene 35

3. RESEARCH OBJECTIVES 42

4. METHODOLOGY 43

4.1 Tin Selenide Fabrication 43
4.1.1 Tin Selenide-Graphene Composite Fabrication 44
4.2 Bismuth Telluride Fabrication 45
4.2.1 Bismuth Telluride-Graphene Composites 46
4.3 Characterization 47
4.3.1 Chemical and Structural Properties 47
4.3.2 Thermal Properties 52
4.3.3 Mechanical Properties 54

5. RESULTS AND DISCUSSION 55

5.1 Tin Selenide and Tin Selenide-Graphene Nanocomposites 55
5.1.1 Chemical and Structural Properties 55
5.1.2 Thermal Properties 63
5.1.3 Mechanical Properties 69
5.2 Bismuth Telluride Based Materials 69
5.2.1 Chemical and Structural Properties 70
5.2.2 Thermal Properties 79

6. CONCLUSION AND FUTURE WORK 83

REFERENCES 85

APPENDIX A 102

Appendix A.1 102
Appendix A.2 106

LIST OF FIGURES

Page

Figure 1: Waste heat temperature distribution for different sectors. Adapted from Forman et al. (2016) [1] 1

Figure 2: TE generator (left) and TE refrigerator (right). Both are thermally connected in parallel and electrically in series. For the TE generator, a temperature gradient induces a potential difference that is used to generate energy. A current passes through the TE cooler, inducing a temperature difference, and the cold side absorbs heat. Adapted from Brinks & Huijben (2015) [7]. 6

Figure 3: Schematic of a TE generator. The thermal energy from the heat flow (provided from an external source) is converted to electrical energy. Note that the thermal elements are connected in parallel. Adapted from Saidur et al (2012) [9] 6

Figure 4: ZT and its constituents – Seebeck coefficient (denoted here as α), the electrical resistivity (ρ), and the thermal conductivity (κ). These parameters must be optimized by focusing on different aspects of the materials to enhance ZT, as illustrated in figure. Adapted from He & Tritt (2017) [3]. 8

Figure 5: Different scattering mechanisms and their variance with temperature. Adapted from Hooshmand et al. (2019) [15] 10

Figure 6: Projected applications of TE materials, according to their power consumption, performance (ZT), and efficiency (η). Adapted from Freer & Powell (2020) [2] 13

Figure 7: Evolution of ZT of various thermoelectric materials. Adapted from He &Tritt (2017) [3] 16

Figure 8: Decrease in k_L due to different point defects: (a) solid solutions, (b) vacancies (c) interstitials. Adapted from Zhou et al. (2018) [14] 19

Figure 9: Effect of resonance on k_L of Co_4Sb_{12}. Adapted from Nolas et al. (1998) [40]. 23

Figure 10: ZT along all axes of SnSe. The ZT is higher along the b and c axis than the a-axis, showing the anisotropy. Adapted from Zhao et al. (2014) [72] 30

Figure 11: Layered crystal structure of $SnSe_2$. Adapted from Saha et al. (2016) [83] 32

Figure 12: Various structures derived from graphene. Adapted from Kakaei et al. (2019) [92] 36

Figure 13: The relationship of power factor and electrical conductivity with PANI:GN ratio. Adapted from Du et al. (2012) [95] 37

Figure 14: Material illustration and figure of merit (ZT) for $CoSb_3$ samples. Adapted from Feng et al. (2013) [99] 39

Figure 15: Variation of ZT with temperature for LSTO-Graphene composites. The peak value of ZT is reached at room temperature, for the composite with 0.6 wt% graphene. Adapted from Lin et al. (2015) [100] 40

Figure 16: Flow chart of the methodology 43

Figure 17: Working principle of a TEM 51

Figure 18: Thermal conductivity testing equipment 53

Figure 19: Indenter and indentation made for the microhardness measurements. Adapted from Smallman & Ngan (2014) [113] 54

Figure 20: XRD of $SnSe_2$ and $SnSe_2$ Composites 56

Figure 21: Williamson-Hall linear fit for pure $SnSe_2$ nanopowders 57

Figure 22: Warren-Averbach linear fit for pure $SnSe_2$ nanopowders 58

Figure 23: (a) Survey spectra of the pure $SnSe_2$, (b) Sn 3d scan, (c) Se 3d scan 60

Figure 24: $SnSe_2$-0.50% GO: XPS spectra of (a) Se 3d, (b) Sn 3d, and (c) O 1s 60

Figure 25: SEM images of $SnSe_2$ and $SnSe_2$-Graphene composites 62

Figure 26: TEM images of (a,b) pure $SnSe_2$, (c,d) $SnSe_2$-0.05% GO, (e,f) $SnSe_2$-0.10% GO, (g,h) $SnSe_2$-0.25% GO, and (i,j) $SnSe_2$-0.50% GO 63

Figure 27: DSC thermograms of $SnSe_2$-GO composites, performed from ambient to 450 ˚C under N_2 atmosphere 65

Figure 28: TGA for $SnSe_2$ and $SnSe_2$-Graphene composites heated at 10 ˚C/min under N_2 atmosphere 66

Figure 29: Thermal conductivity, k, and thermal diffusivity, α, for the $SnSe_2$-graphene nanocomposites 67

Figure 30: Effect of graphene loading on the hardness of $SnSe_2$ 69

Figure 31: XRD patterns of pure Bi_2Te_3 and Bi_2Te_3-graphene composites. 71

Figure 32: Williamson-Hall linear fit for pure Bi_2Te_3 crystals 72

Figure 33: Warren-Averbach linear fit for pure Bi_2Te_3 crystals 73

Figure 34: (a) Survey spectra of the pure Bi_2Te_3, (b) Bi 4f scan, (c) Te 3d scan..... 74

Figure 35: XPS analysis of Bi_2Te_3-0.25% GO (a) Bi 4f scan, (b) Te 3d scan 75

Figure 36: SEM images of (a-c) pure Bi_2Te_3 with CTAB, (d-f) pure Bi_2Te_3 without CTAB, (g-i) Ag-doped Bi_2Te_3, (j-l) Bi_2Te_3-0.25% GO, and (m-o) Bi_2Te_3-0.25% GO 77

Figure 37: (a) SEM image of the needle-like structure in Bi_2Te_3-0.25% GO and corresponding EDS mapping on the surface for (b) Te, and (c) Bi. 78

Figure 38: (a) SEM image of the wood-like structure in Bi_2Te_3, and corresponding EDS mapping on the surface for (b) Te, (c) Bi, (d) O, and (e) C 79

Figure 39: DSC of various Bi_2Te_3 nanopowders, performed from ambient to 450 ˚C under N_2 atmosphere..... 80

Figure 40: TGA of Bismuth Telluride samples heated at 10 ˚C/min, under N_2 atmosphere 82

LIST OF TABLES

Page

Table 1: Properties of bismuth telluride [46] 25

Table 2: Methods of synthesizing bismuth telluride. Adapted from Mamur et al. (2017) [46] 26

Table 3: Thermoelectric properties of alloyed and doped bismuth telluride 28

Table 4: Thermoelectric properties of doped $SnSe_2$ 34

Table 5: Synthesis methods for $SnSe_2$ 35

Table 6: Mass of the precursors used for the synthesis of $SnSe_2$ and $SnSe_2$-graphene nanocomposites 45

Table 7: Mass of the precursors used for the synthesis of Bi_2Te_3-based materials 47

Table 8: Characterization tests performed on the synthesized materials 47

Table 9: Grain sizes for pure $SnSe_2$ and $SnSe_2$-Graphene composites obtained using Scherrer, Williamson-Hall, and Warren-Averbach methods 59

Table 10: Composition of $SnSe_2$ and $SnSe_2$-Graphene composites 61

Table 11: Thermal parameters for $SnSe_2$ and $SnSe_2$-GO composites obtained from DSC analysis 64

Table 12: Thermal conductivities of $SnSe_2$-based materials from literature 68

Table 13: Grain size of pure Bi_2Te_3 and Bi_2Te_3-based materials obtained using Scherrer, Williamson-Hall, and Warren-Averbach methods 73

Table 14: Elemental quantification of Bi_2Te_3 and Bi_2Te_3 composites 76

Table 15: Thermal parameters for Bi_2Te_3-based materials obtained from DSC analysis 81

1. INTRODUCTION

In the current era, fossil fuels are the primary source of power generation. However, energy generated from such sources produces significant amounts of waste heat. A significant component of this waste heat is low-grade waste heat, which is energy lost below a temperature of 230 ˚C. The power generation sector, followed by the transportation sector, are major contributors to this form of waste heat, as shown in Figure 1.

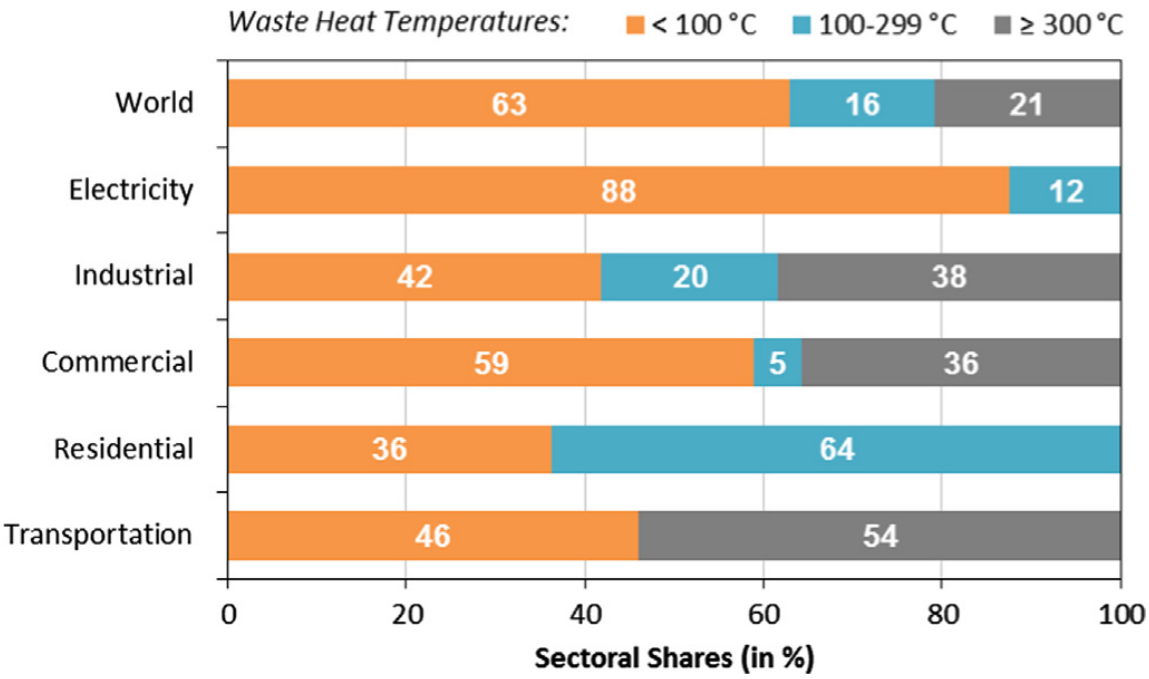

Figure 1: Waste heat temperature distribution for different sectors. Adapted from Forman et al. (2016) [1]

Despite a large amount of low-grade waste heat dissipated from all processes, the recovery of this heat is very low because of its low exergy. Additionally, Carnot's principle states that for a lower temperature gradient, the work available also decreases, which reduces the cost efficiency of the process too. Nevertheless, Rankine cycle-based processes are currently used to recover some of this heat and convert it into usable energy. As steam cannot be used at low temperatures, the working fluids used for these processes consist of benzene or R-134a, which are harmful and environmentally toxic [2]. Therefore, alternative routes must be explored to recover this heat. Due to their form factor adaptability, reliability, and simplicity, thermoelectric generators (TEG) are excellent candidates to be employed for this purpose.

TEGs are preferable as do not require moving parts as a mechanical cycle-based machine would, and they also have a much faster response time. Additionally, there is no chemical discharge during operation, further making them an attractive method for waste heat recovery. TEGs use thermoelectric (TE) materials to recover the waste heat. TE materials work by converting thermal energy – a temperature difference applied across the device – to electrical energy. The reverse effect also occurs. The performance of these materials is defined by a dimensionless number, the *figure-of-merit*, or ZT.

Tin (IV) selenide ($SnSe_2$) is an attractive material for TE applications due to its excellent electrical properties and low thermal conductivity. Tin (II) selenide has been found to have remarkable TE performance, but tin (IV) selenide has few studies. A high theoretical ZT of 2.95 has been predicted for $SnSe_2$, but experimentally this ZT has not

been reached. This prompts the need for additional studies to investigate methods of improving the properties of $SnSe_2$.

Bismuth telluride (Bi_2Te_3) is one of the most widely studied TE materials due to its excellent inherent electrical properties. It has been studied since the 1960s, and devices using Bi_2Te_3-based materials have been used for cooling modules in small-scale applications, for instance, solid-state refrigerators, thermal sensors, and electronic dehumidifiers. It is the best material for devices operated at room temperature. Some Bi_2Te_3 based materials have also been used to recover low-grade waste heat. The ZT of Bi_2Te_3-based materials has not yet reached 3, which the requirement for commercial applications. Therefore, an improvement in the performance is required to use these devices in large scale applications.

In this thesis, tin selenide and bismuth telluride nanocomposites will be synthesized with graphene using solution methods (hydrothermal and solvothermal). Most studies use solid-state methods, which require pure metals and are cost-intensive. Solution methods will be used for this research as they are cost-effective and easily scalable. The target is a reduction in grain size upon the addition of low amounts of graphene, which will produce materials that have potentially enhanced thermoelectric properties. Graphene is an excellent filler for thermoelectric nanocomposites due to its remarkable thermal and electrical properties. Additionally, the high strength of graphene could improve the quality of the materials for device manufacturing. This thesis aims to enhance the properties by adding graphene and synthesizing the nanocomposites using scalable solution methods.

2. LITERATURE REVIEW

2.1 Thermoelectric Fundamentals

2.1.1 Thermoelectric Coefficients

The thermoelectric effect that is the basis for the function of TE materials is a combination of three phenomena: the Seebeck, the Peltier, and the Thomson effects. Coefficients corresponding to these phenomena define the behavior of the materials [3].

In 1821, the German scientist Thomas Seebeck noted that when a temperature difference was applied to a circuit made from dissimilar metals, it deflected a compass needle nearby. This phenomenon, known as the Seebeck effect, can be explained by electrons flow from the hot side to the cold side induced by the applied temperature difference. That flow of electrons produces a current in the circuit, and therefore a magnetic field [4, 5]. Seebeck coefficient, S, is defined as the ratio of the voltage to the temperature difference in the system [6]:

$$S = \frac{V}{\Delta T} \tag{1.1}$$

The units of the Seebeck coefficient are V/K but usually reported in μV/K [6, 7].

In 1836, French scientist Jean Charles Peltier observed that when current passes through a circuit, heat can either be absorbed or dissipated at the junction. This phenomenon is known as the Peltier effect, which is the basis for the TE refrigerators [4]. The Peltier coefficient, π, is defined as the ratio between the current *I* passing through the system, and the heat *q* [6, 8]:

$$\pi = \frac{I}{q} \tag{1.2}$$

The units of the Peltier coefficient are watts/amp (W/A) or V.

The Seebeck and Peltier coefficients are related through the relation [6]:

$$S = \frac{\pi}{T} \tag{1.3}$$

Lastly, the Thomson effect is related to the rate of generation of reversible heat occurs when current passes through a circuit. The Thomson coefficient, β, is defined as [6]:

$$\beta = \frac{q}{I\Delta T} \tag{1.4}$$

The units for the Thomson coefficient are the Seebeck coefficient units, V/K. The Thomson coefficient, however, is negligible compared to the Seebeck and Peltier coefficients and is often not included when studying thermoelectric materials and their applications [7].

Figure 2 illustrates the circuits within a TE generator and refrigerator, while Figure 3 shows a thermoelectric device.

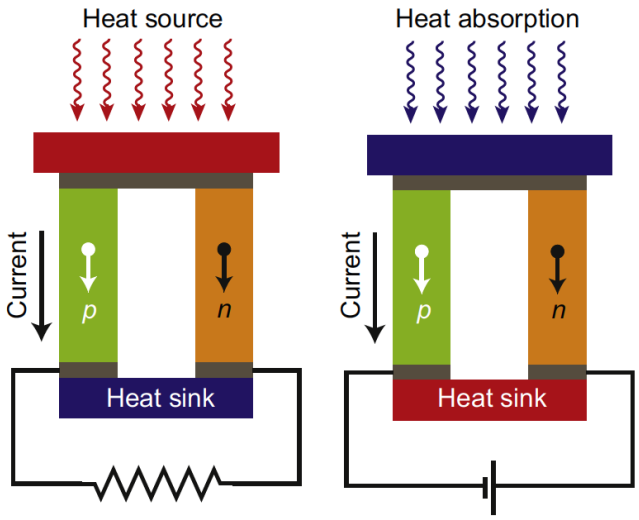

Figure 2: TE generator (left) and TE refrigerator (right). Both are thermally connected in parallel and electrically in series. For the TE generator, a temperature gradient induces a potential difference that is used to generate energy. A current passes through the TE cooler, inducing a temperature difference, and the cold side absorbs heat. Adapted from Brinks & Huijben (2015) [7].

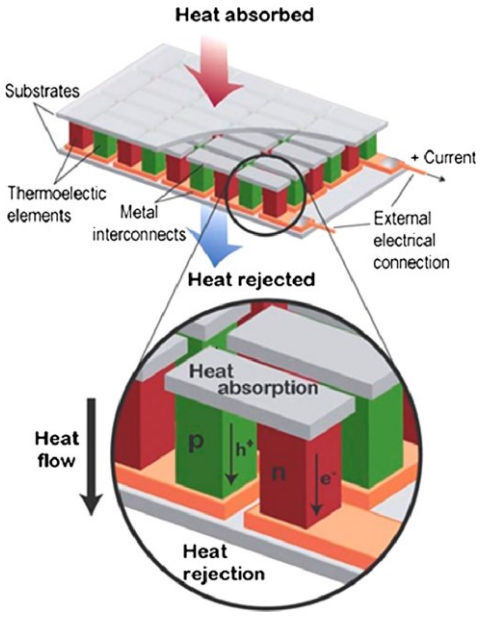

Figure 3: Schematic of a TE generator. The thermal energy from the heat flow (provided from an external source) is converted to electrical energy. Note that the thermal elements are connected in parallel. Adapted from Saidur et al (2012) [9]

2.1.2 The figure-of-merit, ZT

As with any other power generator, a vital aspect of TE devices is the efficiency of the device. The TE performance of a material is measured by the dimensionless figure-of-merit, ZT, which is defined by [5-8]:

$$ZT = \frac{S^2\sigma}{\kappa} \tag{1.5}$$

where σ is the electrical conductivity, κ is the total thermal conductivity of the material encompassing both lattice (κ_L) and electronic (κ_e) contribution, and T is the absolute temperature at which the properties are measured. Figure 4 illustrates the constituents of ZT and the structural properties that should be optimized for ZT enhancement.

For materials with similar thermal conductivities, the performance can be represented by the *power factor (PF)* defined as [10]:

$$PF = S^2\sigma \tag{1.6}$$

The maximum efficiency of a TE generator (η) can be determined from ZT using the relation [7]:

$$\eta = \frac{T_H - T_C}{T_H}\frac{\sqrt{1+ZT}-1}{\sqrt{1+ZT}+\frac{T_C}{T_H}} \tag{1.7}$$

where T_H and T_C are the temperature of the hot and cold junctions, respectively.

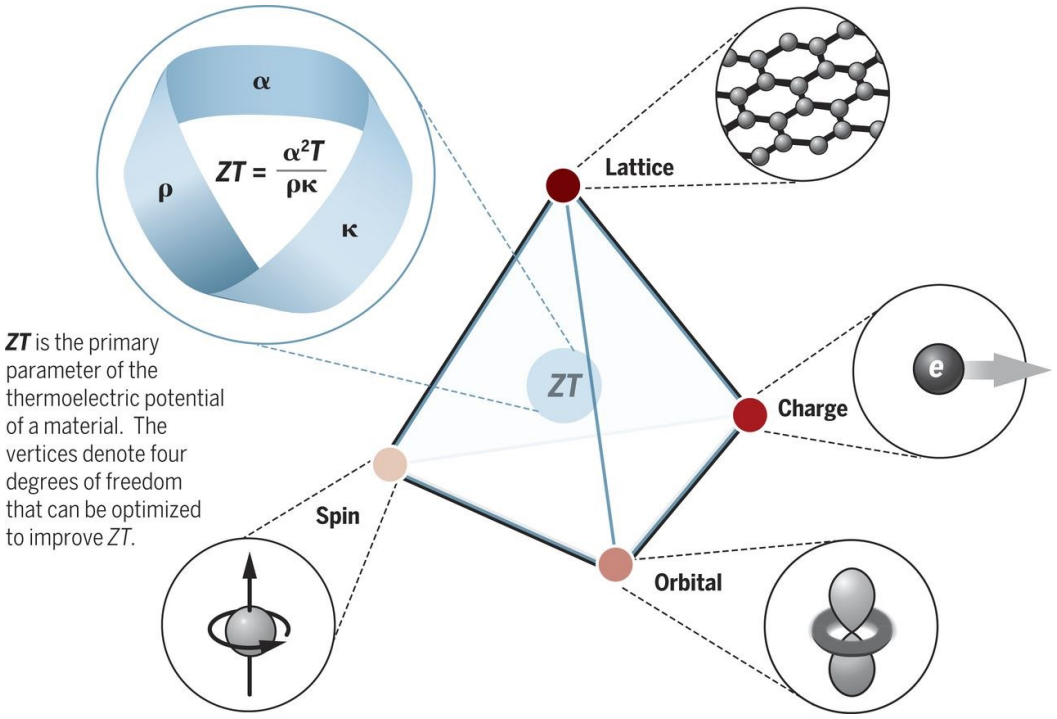

Figure 4: ZT and its constituents – Seebeck coefficient (denoted here as α), the electrical resistivity (ρ), and the thermal conductivity (κ). These parameters must be optimized by focusing on different aspects of the materials to enhance ZT, as illustrated in figure. Adapted from He & Tritt (2017) [3].

For commercial applications, a ZT of at least three is required [7]. ZT can be maximized by increasing the Seebeck coefficient and electrical conductivity and decreasing the thermal conductivity. High electrical conductivity ensures the flow of current, and the low thermal conductivity means a large temperature gradient can be maintained [5]. However, it is not easy to obtain materials with high electrical conductivity and low thermal conductivity. According to the Wiedemann-Franz Law, the electrical and thermal conductivities are inversely proportional. i.e. λ/σ = constant [11]. Additionally, another problem that arises in increasing the ZT is attributed to the Pisarenko relation -

increasing the electrical conductivity (and hence the concentration of charge carriers) impacts the Seebeck coefficient negatively [12]. Therefore, an "optimum" ZT must be targeted. Section 2.3 Techniques for Improving Thermoelectric Performance discusses the different approaches to improve the ZT of thermoelectric material.

2.1.3 Thermal Conductivity

The thermal conductivity (κ) is an important property that can be tuned for enhancing the TE properties. κ is the sum of the lattice thermal conductivity (κ_L) and the electronic thermal conductivity (κ_e). Phonon heat distribution is responsible for k_L, while heat movement by charge carriers is represented by κ_e ($\kappa_e = L\sigma T$, where L is the Lorenz number from Wiedemann-Franz Law, and T is the temperature) [13].

Most TE materials have low electrical conductivity, and heat transfer is dominated by phonon energy transfer. κ_L described by:

$$\kappa_L = \frac{1}{3} C_v v_g l \qquad (1.8)$$

where C_v is the specific heat, v_g is the group phonon velocity, and l is the phonon mean-free path. To reduce κ_L, l can be decreased, which is done through various approaches that enhance phonon scattering, such as point-defect scattering, dislocation scattering, boundary scattering, and phonon-phonon Umklapp scattering. Point-defect scattering impacts high-frequency phonons. Dislocation scattering affects middle-frequency phonons, and interface scattering affects low-frequency phonons. These scattering mechanisms can be employed by either forming a solid solution through substitution one atom in the host with an impurity atom or by introducing an interstitial atom (point-defect

scattering), by creating dislocations via plastic deformation or clustering of vacancies or interstitial atoms (dislocation scattering), and through forming nanoscale precipitates or nanocomposites, or reducing the grain size (interface scattering). Thus, through microstructure control, phonons in all frequencies can be targeted to reduce the k_L of a material. It should also be noted that different scattering methods are dominant at different temperatures, as the frequency distribution of phonons varies with temperature. Figure 5 shows how scattering mechanisms vary in their dominance at different temperatures [14]. The decrease in k_L and its effect on the TE performance is discussed in Sections 2.3.1 Nano-structuring and 2.3.2 Nanocomposites

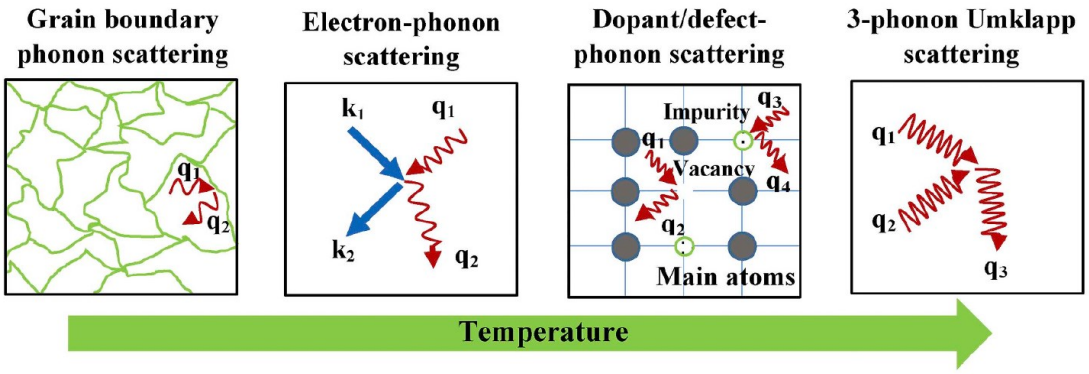

Figure 5: Different scattering mechanisms and their variance with temperature. Adapted from Hooshmand et al. (2019) [15]

2.1.4 Power Factor

The power factor, PF, is defined as $S^2\sigma$ and as observed in Equation (1.5), a higher PF means that a higher ZT can be obtained. The carrier concentration *n* can be used to optimize the PF to a satisfactory level. At a higher *n*, σ increases, but S decreases rapidly. Hence, within a range of *n* (10^{19} – 10^{20} cm^{-3} for most semiconductors), a maximum PF can be reached by tuning S and σ optimally, giving n^*, the optimal carrier concentration [16]. Band structure engineering, carrier concentration optimization, and increasing carrier mobility are used to increase the PF and can all be employed through doping [14]. The mechanism of enhancing the PF via doping is discussed in Chapter 2.3.3 Doping and Alloying

2.2 Thermoelectric Materials

After discovering the TE phenomena, British physicist John William Rayleigh was the first to attempt to use it for power generation in 1885. His results were inaccurate; however, this was followed by several TE devices being developed in the 19th century [17]. These devices were called thermoelectric generators (TEGs), and they consisted of conductors connected in series electrically and parallel thermally. Among these were Cox's pile, made up of zinc, antimony, and tinned iron; the Gulcher and Clammond thermopiles were made up of bismuth, antimony, and iron [18].

However, it was the discovery of the semiconductor technology that advanced the development of TE devices because it led to achieving higher conversion efficiency. In 1947, Maria Telkes at the Massachusetts Institute of Technology constructed a TEG based on lead sulfide (PbS) and zinc antimonide (ZnSb), which achieved an efficiency more than

5% with operation under a temperature difference of 400 K. This was followed by the use of bismuth telluride (Bi_2Te_3) thermocouples for cooling at 273 K [17].

Due to their low efficiency, TE devices were not as successful as commercial devices than conventional engines. These were developed for space crafts, as they did not require high efficiency but did require low maintenance and no mechanical moving parts. Despite the numerous possible applications for TE materials, high enough efficiencies have not been reached for these materials. Therefore, they are not used widely used across all areas. However, they have been successfully implemented in smaller applications, for instance, in thermocouples, laser diode coolers, conventional coolers, telecom lasers, and infrared night vision equipment, among others [7, 19]. A significant breakthrough happened for TE devices when radioisotope thermoelectric generators (RTGs) were developed. The first RTG commissioned was SNAP 3 in 1961, for the Navy Transit 4A. An RTG was also used in several other spacecraft, for instance, Apollo 12, Voyager 1, Voyager 2, and the Curiosity rover on Mars [17]. RTGs use the heat from the decay of a radioisotope used for the device to make electricity. Figure 6 shows the different applications of TE materials.

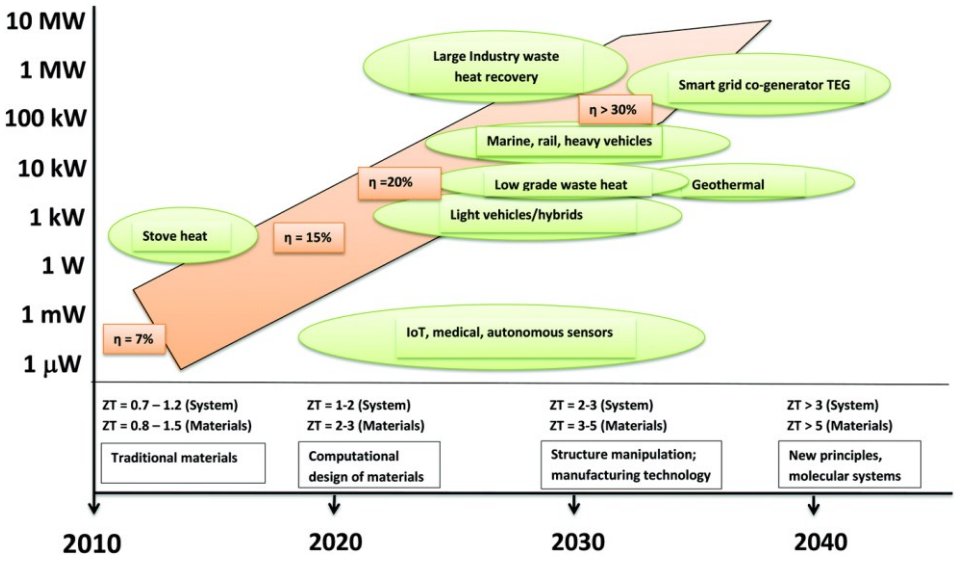

Figure 6: Projected applications of TE materials, according to their power consumption, performance (ZT), and efficiency (η). Adapted from Freer & Powell (2020) [2]

Materials most commonly used in the manufacturing of TE devices are semiconductors, polymers, and ceramics. Lead, tellurium, and germanium have been often used in TE devices, but new classes of materials are being investigated as these metals are either rare and/or toxic. The properties of the three classes of TE materials – semiconductors, ceramics, and polymers – are summarized in the next sections.

2.2.1 Semiconductors

Semiconductors are perhaps the most widely studied material for TE devices, due to their high Seebeck coefficients. Inorganic semiconductors like Bi_2Te3 and its alloys have high ZT due to its high molecular weight that decreases sound velocity and thus decreases thermal conductivity [20]. Materials with a small bandgap are desirable for use in TE devices. In addition to inorganic semiconductors (PbTe, Bi_2Te_3, Mg_2Si), organic

semiconductors are also being studied. These include p-type conducting polymers like poly(3,4-ethylene dioxythiophene) (PEDOT) and n-type conducting polymers such as poly(metal-ethene tetrathiolate) [21]. However, their ZT is not yet high enough for their use in TE devices.

Semiconductor TE materials can also be classified into three types, according to their use-temperature ranges [4]:

- **Bi_2Te_3 based low-temperature materials:** Used below 400 K
- **PbTe based middle-temperature materials:** Used between 600 and 900 K
- **Silicon-Germanium, SiGe, based high-temperature materials:** Used at or above 900 K.

2.2.2 Ceramics

Compared to commonly used semiconductors, metal oxides have higher chemical stability, oxidation resistance, and lower toxicity, making them very desirable candidates for TE devices. Cobalt oxides and cadmium oxides are commonly used as p-type and n-type semiconductors in TE devices, as they have desirable TE properties with a maximum of ZT of 0.21 at 973 K for $Ca_{0.96}Dy_{0.02}Bi_{0.02}MnO_3$, which is still lower than the ZT for alloys of inorganic semiconductors [20].

2.2.3 Polymers

Polymers have inherently low thermal conductivity, which is an advantage for TE materials. They are also readily available and have low costs of production. They have been studied for use at body temperature to power wearable electronics. Elmoughni *et al.*

[22] used poly[Na(Ni-ett)] filled with PEDOT based TE integrated into textiles to harvest body heat. Nevertheless, there are still considerable drawbacks to the use of polymer in TE due to, for instance, the electrical resistance of the fabric and the limited power output. Composites of polymers with Bi_2Te_3, carbon nanotubes, tellurium powders have been studied [20]. However, high ZT has not yet been reached for polymer-based TE devices.

Due to the low ZT of ceramic and polymer-based TE devices, semiconductors are still the front runners in TE devices. Therefore, this study focuses on two semiconductors: bismuth telluride and tin selenide.

Based on their ZT, TE materials can also be divided into three generations [4]:

- **First-generation:** ZT is about 1, and the power conversion efficiency for TE devices is between 4-5%.
- **Second generation:** ZT increased, and power conversion efficiency increased to 11-15%. In this generation, the ZT increased due to the introduction of nanostructures in TE materials. It was suggested that low dimensionality could give a higher $S^2\sigma$ and a low κ and multiple sources found the ZT for 2D bismuth telluride higher than 3D bismuth telluride [23].
- **Third generation:** ZT has been increased to almost 1.8, with the power conversion efficiency levels estimated to reach 15-20%. This breakthrough was made due to several different techniques: band engineering – either doping or distortion of structure or density of states [24, 25], producing quantum materials [26-28], or multi-scale structure tuning to improve lattice conditions (by changing the phonon scattering) [29].

Figure 7 depicts the evolution of ZT of different TE materials.

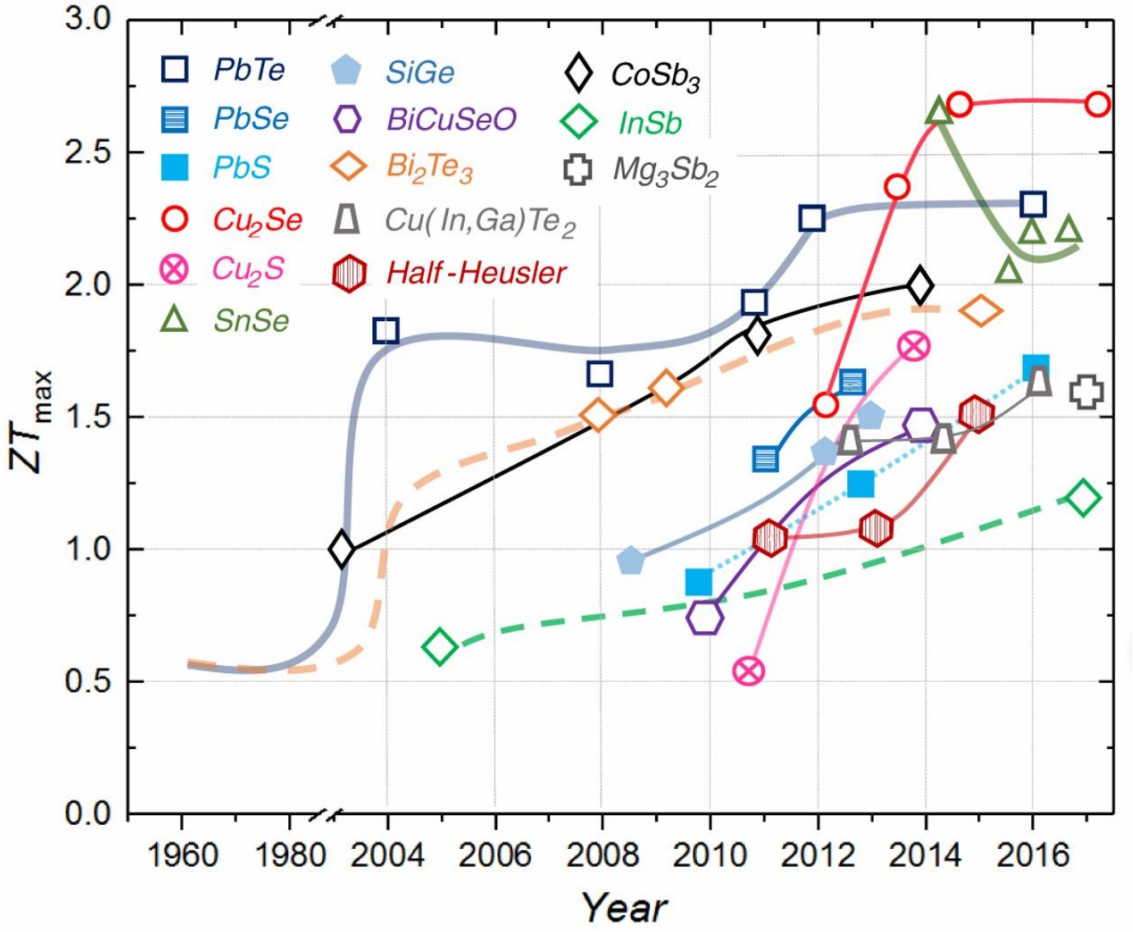

Figure 7: Evolution of ZT of various thermoelectric materials. Adapted from He &Tritt (2017) [3]

2.3 Techniques for Improving Thermoelectric Performance

Several methods have been investigated to increase the performance of TE materials, i.e., increasing ZT. As increasing the electrical conductivity while

simultaneously decreasing the thermal conductivity, κ_L, is limited by the Pisarenko relation, enhancing the performance can be quite challenging. However, several approaches have been developed to enhance the performance of TE materials. These approaches are summarized as follows:

2.3.1 Nano-structuring

Dresselhaus and Hicks first introduced the concept of nanostructures in 1993, when they discovered that zero-dimensional (0D), one-dimensional (1D), and two-dimensional (2D) could theoretically produce excellent electrical properties as compared to the bulk material. Subsequently, 2D structures such as superlattices, 1D structures such as nanowires, and 0D structures such as quantum dots were prepared, and high ZT were reported for these structures. All of these materials were reported to have low lattice thermal conductivities [5]. In low-dimensional structures, κ_L can be reduced significantly, while the electrical conductivity can be increased to a much more considerable amount than possible in the bulk material [21]. In a Bi_2Te_3/Sb_2Te_3 thin film, a thermal conductivity lower than the 'alloy limit' was achieved. The alloy limit was thought to be the lowest achievable thermal conductivity for bulk material through alloying [30].

Nanostructuring improves the thermoelectric performance by one of two ways. It can improve the thermopower by enhancing the density of states (DOS) near the Fermi level through quantum confinement [30]. The DOS increases with a decrease in the dimensionality [31]. The electron energy bands get narrower as the dimensionality decrease, which improves the Seebeck coefficient due to the increase of high effective masses as a result of the narrow banding [32]. It was found theoretically in 2D multiple-

quantum-well structures, and the quantum-well width decreased compared to the bulk material [33]. A PbTe/$Pb_{1-x}Eu_xTe$ system studied by Hicks *et al.* was the first to prove the quantum-well effect experimentally. They found that the power factor increased several times over that of the bulk material [26].

Decreasing k_L due to increased phonon scattering is another way nanostructuring improves TE performance. As most heat in TE materials is transported by phonons [14], this method does not affect the electrical conduction within the material [30]. Phonon scattering can be enhanced by introducing surfaces or defects into the structure to suppress the mean-free path (mfp) of the photons. The introduction of point-defects to the crystal structure can successfully reduce κ_L. Point-defects can arise from substitution in solid solutions, and it is the mass field and strain field fluctuations between the primary and substituted atoms that contribute to the decrease in κ_L. For CoSbS, the intrinsic thermal conductivity is high due to the stiff chemical bonds between the atoms – however, the introduction of Se in the structure decreases the k_L by 43%. Half-Heusler compounds show a similar pattern upon solid solution formation. A more considerable difference in the atomic masses and radii of the host and substituted atoms is preferable [34]. Vacancies within a structure can also act as point-defects. They can be intrinsic but can also be formed in a solid solution where the substituted compound has a smaller cation-to-anion ratio than the matrix [14]. In a study carried out by Tan *et al.,* it was found that k_L for SnTe decreased by introducing $InTe_3$ due to the intrinsic high cationic vacancies present in the In_2Te_3 crystals [34]. Figure 8 illustrates the changes in the κ_L of CoSbS, $CuZnSnSe_4$, and SnTe due to different point defects.

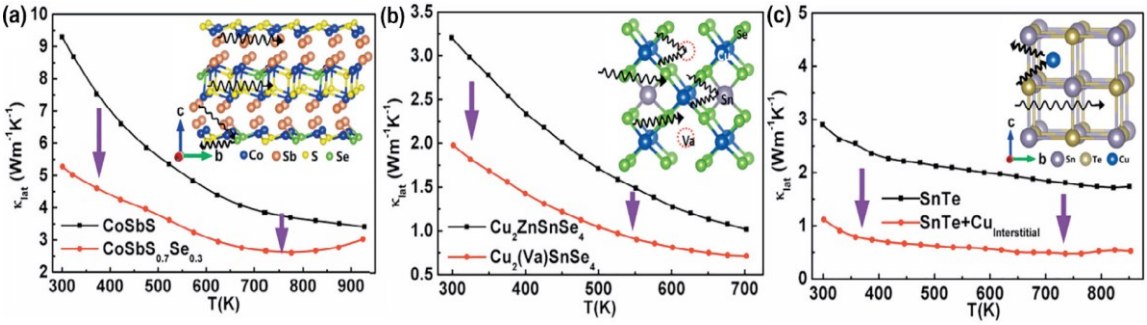

Figure 8: Decrease in k_L due to different point defects: (a) solid solutions, (b) vacancies (c) interstitials. Adapted from Zhou et al. (2018) [14]

Introducing interfaces into a material is an effective way of reducing k_L. Phonon scattering is significantly increased at the site of the interfaces. These interfaces can arise from having nanoscale precipitates within the structure. A reduction in the grain size can increase the interfaces within a material and lead to higher phonon scattering. A high number of small-angle grain boundaries was achieved in a study conducted by Yang *et al.* on Cu_2Se with a high density of dislocations in the structure, enhancing the phonon scattering. Due to this, a κ_L around 60% lower than that of bulk Cu_2Se was obtained [35]. Reducing grain size can be achieved by preparing nanoscale powders by several methods, including ball-milling, melt-spinning, and colloidal synthesis [14]. Bulk quantities of nanostructured materials can be formed by hydrothermal and solvothermal synthesis [36].

2.3.2 Nanocomposites

Most nanostructured materials are prepared by methods that are expensive and hard to scale up for commercial use. The use of nanocomposite-based TE materials was introduced to overcome these obstacles. Nanocomposites are essentially bulk materials

made up of nanostructured constituents. Nanocomposites are cheaper to produce in large quantities, easier to handle, both in characterization and device fabrication and can be shaped in the desired geometry [28].

To produce nanocomposites with enhanced thermoelectric performance, the aim is to create interfaces that decrease the thermal conductivity by phonon scattering, while not impacting the electrical conductivity negatively. Such interfaces must be carefully selected to ensure the increase in the Seebeck coefficient (through quantum confinement) must be higher than any decrease in the electrical conductivity that improves the power factor, and together lead to the increase of ZT of the TE material [28].

The nanocomposite material, in a powder form, can be obtained through hydrothermal and solvothermal methods, wet-chemical synthesis, high energy ball-milling, and self-precipitation techniques. This powder material is then compacted at a temperature below the melting point to fabricate dense TE material [37]. The resulting material does not usually have the ideal morphology that typical nanostructured materials (nanowires, thin films) have, but do have the required thermal and electrical properties [5].

In a study carried out by Poudel *et al.* found an increase of around 40% in the ZT of p-type BiSbTe nanocrystalline alloy as compared to the bulk material. The nanopowders were produced using ball milling, following which they were hot-pressed. The improvement in the ZT was contributed to the decrease in the thermal conductivity due to increased phonon scattering. The presence of a high number of interfaces from the nanograins within the material enhanced the scattering. The ZT at room temperature was

1.2 and 0.8 at 250 ˚C, suggesting that it would be an optimal candidate for cooling and low-temperature waste heat recovery applications [38].

Joshi *et al.* prepared bulk p-type SiGe alloy nanostructured material by ball-milling of boron, silicon, and germanium followed by hot-pressing to produce cylindrical pellets. Boron was added for doping the nanopowders. The grains had a mean size of 15 nm. The thermal conductivity, Seebeck coefficient, power factor, and ZT were all higher than that of bulk alloy SiGe. The ZT improved by 50% over the previously recorded value of 0.65, reaching 0.95 at 800 ˚C. SiGe alloys are used in radioisotope thermoelectric generators (RTG) at temperatures of 1000 ˚C, and the materials fabricated by Joshi *et al.* obtained a 90% increase in the ZT as compared to the commercially used SiGe alloy. As with the BiSbTe alloy, the high ZT for SiGe was attributed to increased phonon scattering due to the high density of interfaces within the nanocomposite [39].

Nanocomposites of thermoelectric materials with graphene have very favorable results. Graphene is an excellent candidate for use in TE materials as it has high electrical conductivity and excellent mechanical strength, which is a favorable property for being used in devices as well be discussed in detail in Section 2.3 and 2.3.1.

2.3.3 Doping and Alloying

When a foreign element is introduced into the crystal structure of a metallic system, a few lattice sites of the metallic system will be substituted by that foreign element changing the structure of the material and increasing the phonon scattering. The increase in the phonon scattering reduces the thermal conductivity of the material, improving the thermoelectric performance. Doping aims to improve the Seebeck coefficient of the

material through band engineering. A high Seebeck coefficient can be attributed to a high DOS with a high effective band mass. However, having a high band mass can negatively impact the mobility of the charge carriers and decrease the conductivity, leading to a net result of no change in the ZT even if the Seebeck coefficient is improved. Hence, the goal of doping is to increase the DOS while keeping the effective band mass low to ensure the electrical conductivity does not decrease [24].

Doping can create resonant levels within the original material, which leads to distortion of the density of states near the Fermi level when the dopant has energy levels in a band of the host material. This distortion can significantly improve the thermopower. Heremans *et al.* [25] doped PbTe with thallium and obtained an increased Seebeck coefficient due to the distortion of states, and ZT of 1.5 at 773 K for p-type $Tl_{0.02}Pb_{0.98}Te$, which was 100% higher than the ZT of conventional PbTe alloys (maximum ZT of 0.71 was obtained for $Na_{0.01}Pb_{0.99}Te$). Heremans *et al.* [25] also noted that the addition of other group 3 elements, germanium, and indium could also create resonant levels within the original material. The carrier concentration decreases, improving the thermoelectric properties of the material.

Co_4Sb_{12} was doped with La in a study conducted by Nolas *et al*. [40]. The La atoms are loosely bound to the Sb atoms, and the vibration of these atoms scatter phonons that have a similar frequency. This phenomenon is called the resonance scattering mechanism. Resonance can have a significant impact on the κ_L of Co_4Sb_{12}, as shown in Figure 9. Nolas *et al.* also found that a partially filled structure gave better results than a filled structure, as a heavily filled structure increases the carrier concentration but decreases the mobility.

A partially filled structure increases both the carrier concentration and the mobility because of the random distribution of the La atoms within the structure.

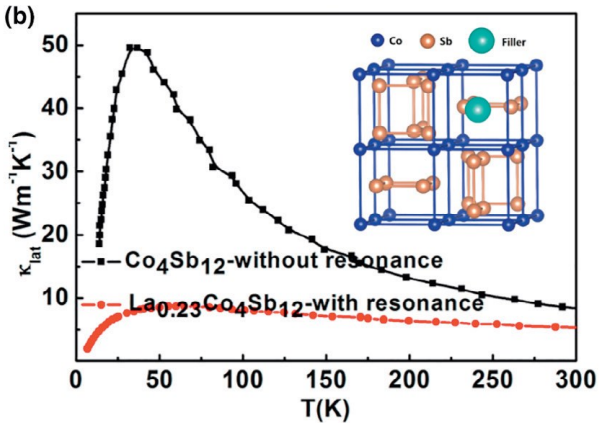

Figure 9: Effect of resonance on k_L of Co_4Sb_{12}. Adapted from Nolas et al. (1998) [40]

While increasing the phonon scattering decreases the thermal conductivity, it can also negatively impact the electrical conductivity. To overcome this, carrier concentration can be tuned. Alloying is an excellent way to tune carrier concentration, which was also achieved in the PbTe system. Pei *et al.* alloyed the PbTe with Mg allowed to increase the bandgap, which decreased the required optimal carrier concentration.

Additionally, doping the material with 2%, Na enhanced the performance further. The temperature dependence of the carrier concentration also decreased, leading to an average ZT that is 40% higher than that of previously reported PbTe system. The maximum ZT achieved by Pei *et al.* was 1.7 at 870 K [41].

Band convergence can positively impact the ZT of the material by increasing the degeneracy states of the material, which increases the effective mass (enhancing the Seebeck coefficient) without impacting the mobility [42]. Li *et al.* [43] doped SnTe with Ge and Sb and noted ZT increase by more than 150% for the sample doped with Ge and Sb compared to the ZT for pure SnTe. It worth noting that the addition of Sb alone did not produce much improvement. A maximum ZT of around 0.85 was reached at 850 K for $Sn_{0.92}Ge_{0.04}Sb_{0.04}Te$. However, the lattice thermal conductivity of 1.01 $Wm^{-1}K^{-1}$ was still higher than the amorphous conductivity limit (0.4 $Wm^{-1}K^{-1}$) of that composition. To reduce the thermal conductivity, the material was alloyed with 5% Cu_2Te, and the combination of co-doping and alloying reduced k_L to 0.27 $Wm^{-1}K^{-1}$ and increased ZT to a maximum of 1.5 at 873 K [43].

2.4 Materials Studied

Two materials were studied for this project: bismuth telluride and tin (IV) selenide. They are discussed in detail in the following sections.

2.4.1 Bismuth Telluride

Bismuth telluride (Bi_2Te_3) is one of the most widely studied TE materials. Tellurium belongs to the chalcogenide group of metals. Chalcogenide metals are semiconductors that have a bandgap of 1-3 eV. Bismuth has one of the lowest thermal conductivities of any metals, which is an attractive quality for a possible TE material. Bi_2Te_3 has a quasi-layered lattice structure [44]. The TE performance Bi_2Te_3 was first discovered in the 1950s. Since then, it has been studied extensively and used widely.

Bi_2Te_3 based alloys are widely used in cooling modules used for solid-state refrigerators, thermal sensors, thermopiles, and electronic dehumidifiers [6, 45]. Additionally, nanostructured Bi_2Te_3 can give ZT > 1, which can be used to recover low-temperature waste heat and solar heat [38, 44]. Table 1 summarises the main properties of Bi_2Te_3:

Table 1: Properties of bismuth telluride [46]

Parameter	**Properties**
Crystal structure	Hexagonal-rhombohedral phase
Average lattice constant	α = 4.392 Å, and c = 30.438 Å
Average crystalline size	~ 97 nm
ZT value	0.58 to 1.16
Average diameter	100 – 600 nm
Average width/length	0.1 – 15 μm
Average thickness	10 – 50 nm
Electron affinity	1.87 – 3.44 eV
Band gap	~ 0.15 eV

After discovering that low-dimensional materials can have excellent TE properties, the research on Bi_2Te_3 has focused on producing it in different nanoforms, i.e., nanotubes, nanosheets, nanoflowers, and nanorods. Production of nano-sized Bi_2Te_3 can be achieved through several methods including solvothermal, hydrothermal, mechanical alloying, water-based chemical reduction, chemical oxidation, wet chemical method, and refluxing [46]. These different methods for the production of Bi_2Te_3 give different

structures. The characteristics of the chemical and mechanical methods for the preparation of bismuth telluride are summarised in Table 2.

It is evident from Table 2 that the highest ZTs were obtained with samples synthesized via solvothermal or hydrothermal methods or using large-scale zone melting. For this research, a solvothermal method was selected to synthesize bismuth telluride because it is cost-effective, and the potential of the resulting materials having high ZT.

Table 2: Methods of synthesizing bismuth telluride. Adapted from Mamur et al. (2017) [46]

Synthesis Technique	**ZT**	**Cost-**	**Device-quality**	**Developed Size**	**Comments**
Solvothermal /hydrothermal	1.16	Low	Best	~ 10 nm	Cost-effective
Straight forward arc-melting	Low	Low	Fair	Pellets	Microstructural characterization difficult
Bridgman	Low	High	Fair	Single crystal	Difficult for device application
Mechanical alloying	Medium	High	Good	~ 10 nm	High temperature and pressure
Polyol	Medium	Medium	Poor	~ 200 nm	Uses toxic chemical
Water-based chemical reduction	Low	Medium	Poor	~ 300 nm	Particle size cannot be controlled
Chemical oxidation	Low	Medium	Poor	Not uniform	Electrical properties cannot be improved
Wet chemical	Medium	Low	Good	~ 30 nm	Uses toxic chemical
Refluxing	Medium	Medium	Good	~ 15 nm	Has to be handled very carefully
Cryogenic grinding	Medium	Medium	Poor	~ 70 nm	Not suitable for devices
Large-scale zone melting	ZT = 1.15	Medium	Good	Nano-structure	Microstructural characterization difficult

Table 2 Continued

Synthesis Technique	ZT	Cost	Device-quality	Developed Size	Comments
Facile solution	Medium	Medium	Fair	~ 22 nm	Uses toxic chemical

Solution-based methods are also easily scalable compared to solid-state methods. Additionally, Solution synthesized materials give the best device quality material, which is a favourable attribute as the material will eventually be used in a device. A templating ligand can be employed in hydrothermal/solvothermal synthesis to produce unique morphologies – the ligand acts as a chelating agent, which removes any ionic impurities from precursors be present within the final product. Additionally, uniformly sized nanoparticles can be produced using a templating ligand. Commonly used templating ligands include EDTA (ethylenediaminetetraacetic acid), ethylenediamine, polyvinylpyrrolidone, and pyridine [36].

As mentioned in Section 2.3 Techniques for Improving Thermoelectric Performance, an excellent way of improving the TE performance is through doping or alloying. Therefore, tremendous research has been done over the years on doping Bi_2Te_3 and observing the effect on its TE properties. It was found that doping Bi_2Te_3 improved the TE performance as compared to pure Bi_2Te_3. Samat *et al*. [47] reported an increase of 300% in ZT of Pt doped Bi_2Te_3 compared to pure Bi_2Te_3 because of the enhancement in the phonon scattering due to the change of the grain size and the existence of defects in the crystal lattice, which decreased the thermal conductivity. An improvement of ~ 300% in ZT was also reported by An *et al.* [48] via doping with copper. While the electrical

conductivity decreased upon doping with copper, the thermal conductivity decreased much further, leading to an increase in ZT. Other studies also reported a decrease in thermal conductivity. Bohra *et al.* [49] reported a 25% improvement in ZT and lowered the thermal conductivity of the lead doped Bi_2Te_3 than that of pure Bi_2Te_3. For Bi_2Te_3 produced via the hydrothermal route, Yang *et al.* [50] reported ZT of 1.7 for the lutetium doped Bi_2Te_3, corresponding to a 90% increase in lutetium doped Bi_2Te_3. This enhancement was attributed to increased phonon scattering due to the small grains within the Bi_2Te_3 grains. Other similar systems are summarized in Table 3, with their TE properties (ZT, thermal conductivity – k, and power factor – PF):

Table 3: Thermoelectric properties of alloyed and doped bismuth telluride

Filler	Preparation Method	κ W/m.K	PF μW/m.K^2	ZT	T K	Ref.
Platinum	Electrodeposition	1	1780	0.65	298	[47]
Copper	Reflux disproportionation and SPS	0.8	1450	0.67	415	[48]
Lead	Vacuum melting	1.62	-	0.63	386	[49]
Lutetium	Hydrothermal and hot pressing	0.62	2850	1.7	373	[50]
CNT	Sonication and ball-milling	1.1	-	0.25	300	[51]
Amorphous Carbon		1.1		0.25		
Silver	Thermal co-evaporation	-	216	-	523	[52]
Silver	Zone melting & hot deformation	1.2	-	1.1	350	[53]
Chromium	Annealing	1.85	950	0.37	400	[54]
Copper	Ball milling and SPS	0.9	-	~0.82	380	[55]
Aluminum oxide	Polyol reduction and SPS	0.85	-	0.2	300	[56]
CNT	Sonication and compression molding	0.43	-	$3x10^{-5}$	298	[57]
UHMW PE						
Lead	Magnetron sputtering and annealing	0.83	2150	1.23	473	[58]
GQD	Solution and SPS	0.65	880	0.55	425	[59]

Table 3 Continued

Filler	Preparation Method	κ W/m.K	PF μW/m.K^2	ZT	T K	Ref.
Germanium ($Bi_{39}Ge_1Te_{60}$)	Mechanical alloying and annealing	1.6	3900	0.9	325	[60]
Germanium ($Bi_{32.5}Ge_{10}Te_{57.5}$)		1.2	1200	0.45	525	[60]
Copper ($Bi_{1.99}Cu_{0.01}Te_3$)	Mechanical alloying and Annealing	2	7750	1.2	300	[61]
Copper $(Cu_2Te)_{0.09}(Bi_2Te_3)_{0.9}$		1.8	250	1.09	363	
Cerium	Hydrothermal and hot pressing	0.5	-	1.29	398	[62]
Iodine	Hydrothermal and hot pressing	0.8	1980	1.1	448	[63]
Selenium	Ball milling and hot pressing	1.15	2500	1.2	445	[64]
Antimony		1.2	-	1.3	380	
Selenium	Hydrothermal and SPS	0.65	1280	0.7	485	[65]
Lanthanum	Hydrothermal and hot pressing	1.5	-	0.58	480	[66]
Graphene	Ball milling and high-frequency induction heating sintering	1.1	1150	0.55	~500	[67]
Graphene	Reflux and pressure pressing	1.575	-	0.37	345	[68]
MWCNT	Hydrothermal and hydrothermal pressing	0.92	-	0.37	333	[69]

2.4.2 Tin Selenide

Tin selenide exists in two forms: tin (II) selenide, SnSe, and tin (IV) selenide, $SnSe_2$. They belong to the IV-VI family. SnSe is a p-type semiconductor (conduction is mainly due to the movement of positive holes), while $SnSe_2$ is an n-type semiconductor (conduction is mainly due to the movement of negative electrons). Tin selenide also has other applications in addition to TE applications. Metal selenides have been used for electrodes for sodium-ion batteries, as they are earth-abundant and have a high specific

capacity [70]. Therefore, tin selenide is also a promising candidate for battery applications. The uses of tin selenide also extend to solar energy applications, infrared optoelectronics, photovoltaic cells, and supercapacitors [71].

The potential of SnSe to be used as a TE material was only realized in 2014 when the ZT along the *b*-axis in p-type orthorhombic single-crystal SnSe was found to be 2.6 by Zhao *et al*. at 923 K. This was a record high in bulk TE material. Zhao *et al.* also reported a ZT of 2.3 ± 0.3 along the *c*-axis and a ZT of 0.8 ± 0.2 along the *a*-axis. At room temperature, the ZT along the *b*-axis was in the range of 0.12 – 0.15 [72, 73]. The ZT of SnSe increases as it goes through its transition temperature of 750 K. At this temperature, the structure of orthorhombic SnSe changes from *Pnma* to *Cmcm* [74]. Figure 10 shows the change of ZT with temperature across all three axes.

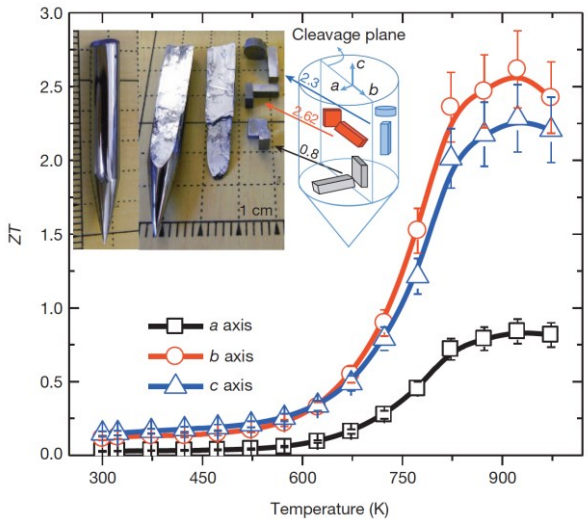

Figure 10: ZT along all axes of SnSe. The ZT is higher along the b and c axis than the a-axis, showing the anisotropy. Adapted from Zhao et al. (2014) [72]

The ZT of tin selenide at room temperature was found to be improved via doping. Doping with silver (Ag) yields a ZT (0.65), which is higher than that of pure SnSe at 750 K. As the concentration of Ag increases, so does the electrical conductivity. But the Seebeck coefficient and thermal conductivity decrease with an increase in the Ag concentration. The ZT is not high enough to promise good performance [29]. Sodium (Na) doped SnSe posed as a promising TE material – with the increase in the concentration of Na, the thermal conductivity decreases, and the power factor of Na-doped SnSe is higher than that of the pure crystal [75, 76]. However, it is not applicable for devices as the thermal cycle stability of Na-doped SnSe is not great. Recently, germanium (Ge) doped SnSe is being studied. Ge-doped SnSe shows an increased Seebeck coefficient [77].

Although high ZT for SnSe was predicted, these high ZT was based on single-crystal SnSe that is hard to produce. Polycrystalline SnSe does not have ZT as high as that of a single crystal SnSe, limiting the usage of SnSe in large scale applications [78]. Tin (IV) selenide has not been studied as extensively as tin (II) selenide, but it is a promising thermoelectric material. The crystal structure for tin (IV) selenide is hexagonal close-packed, with lattice parameters of a = 3.811 Å and c = 6.137 Å [79]. The band-gap for this compound is between 0.9-2.04 eV, along with a carrier concentration of $10^{17} – 10^{19}$ cm^{-3}, and electron mobility between 0.6-85 $cm^2/V.s$ [80].

A few studies have been performed on $SnSe_2$, both experimental and theoretical. In the first-principles study carried out by Sun *et al.*, a peak ZT value of 0.88 at 800 K was found. A low lattice thermal conductivity of 0.55 $Wm^{-1}K^{-1}$ has been predicted for $SnSe_2$ with a power factor of 1172 μ $Wm^{-1}K^{-2}$. The study also found that the lattice thermal

conductivity increased very slightly with an increase in temperature, which is favorable for TE performance [81]. Furthermore, theoretical studies reported a ZT of 2.95 in the a-axis, and a ZT of 0.68 in the c-axis for n-type $SnSe_2$ [82]. $SnSe_2$ has a layered structure, which leads to highly anisotropic properties, such as electrical conductivity. The ratio of electrical conductivity in the a-axis to the c-axis σ_a/σ_c was 6.92 at 300 K [81]. The layered structure can also improve the TE performance of the material as the thermal and electrical properties can be tuned effectively by controlling the interlayer and layer spacing independently [82]. An illustration of the structure can be seen in Figure 11.

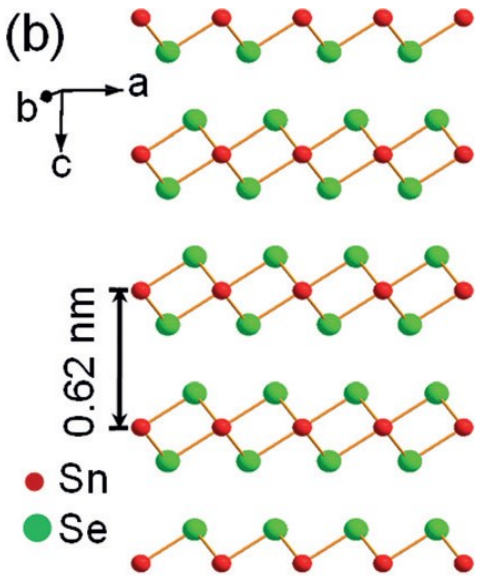

Figure 11: Layered crystal structure of $SnSe_2$. Adapted from Saha et al. (2016) [83]

Sun *et al.* [78] *synthesized* flower-like nanostructured $SnSe_2$ via the solvothermal method and obtained ZT of 0.57 at 550 K. This ZT was higher than the ZT reported for other pure $SnSe_2$. Saha *et al.* [83] reported a maximum ZT of 0.15 at 610 K, and Luo *et al.* [84] also reported the same ZT for pure $SnSe_2$ nanoplates at 773 K. A room temperature lattice thermal conductivity of a value of 0.67 $Wm^{-1}K^{-1}$, which is close to the theoretical minimum lattice thermal conductivity, was reported by Saha *et al.* [83]. This low thermal conductivity was achieved through doping the synthesized $SnSe_2$ with chlorine. Doping is a successful way to improve the TE performance of $SnSe_2$over that of pure $SnSe_2$. The highest ZT was reported by Liu *et al.* through silver nanoprecipitation and chlorine doping. Ag is present within the nano-precipitates of $AgSnSe_2$, and Ag^+ ions insert themselves in the gaps between the layers. Cl doping was performed because the addition of Ag alone is insufficient for optimal carrier concentration. Cl replaces the Se atoms in the structure. Cl doping increases the carrier concentration and the carrier mobility, significantly enhancing the electrical conductivity and, consequently, the power factor. Liu *et al.* also noted a decrease in the thermal conductivity due to Ag presence in the system, which produced significant defects, enhancing the phonon scattering [85]. The TE properties (ZT, thermal conductivity – k, and power factor – PF) of other doped $SnSe_2$ systems are summarized in Table 4.

Table 4: Thermoelectric properties of doped $SnSe_2$

Filler	Preparation Technique	*K* W/m.K	PF mW/m.K²	ZT	T K	Ref.
Chlorine	Solution-based synthesis and hot pressing	0.4	145	0.22	610	[83]
Silver introduction and chlorine doping	Hydrothermal synthesis and SPS	0.6	600	1.03	789	[85]
Chlorine	Hydrothermal synthesis and SPS	1.95	1013	0.3	573	[86]
Chlorine	Solid-state method and SPS	1.25	560	0.56	773	[87]
Silver	Ball milling	1	350	0.4	773	[88]
Silver Chloride	Hydrothermal synthesis and SPS	0.6	275	0.35	673	[89]
Bromine	Melting, quenching, and hot pressing	1.7	-	0.62	750	[90]
Chlorine	Vacuum melting and hot pressing	0.9	400	0.4	673	[91]

As with bismuth telluride, there are several ways to prepare tin selenide. These include both chemical (hydrothermal/solvothermal, solution-based) methods and mechanical methods. Generally, hydrothermal and solvothermal approaches are preferred due to the ease of controlling the shape, size, and crystallinity of the products by manipulating the process conditions – the temperature at which the synthesis is performed, the synthesis time, the precursor type, and the solvent type [36]. Table 5 summarizes the different methods, the size of the products obtained from those methods, and comments about the process. As nanostructures are better for TE properties, all the methods summarized in the table give a favorable size. The highest ZT was obtained by Sun. *et al.* [78], who followed a hydrothermal approach. As this research focuses on solution-based methods, a hydrothermal approach will be followed.

Table 5: Synthesis methods for $SnSe_2$

Preparation Technique	ZT	Developed Size	Comments	Ref.
Hydrothermal synthesis	0.57	10 nm	Cost-effective method, easy to control parameters	[78]
	0.15	4.5 nm		[85]
	0.02	130 nm		[86]
Solvothermal synthesis	0.15	20 – 45 nm		[89]
Solution-based synthesis and hot pressing	0.15	3 – 5 nm	Low-cost and low temperature	[83]
Melting and quenching	0.09	Ingots	High temperature required	[87]
	0.02			[90]
Ball milling	0.028	50 – 100 nm	Low cost method	[88]
Vacuum melting and hot pressing	0.01	Ingots pressed to 11 mm cylinders	High temperature and pressure required	[91]

2.4.3 Graphene

Graphene is the building block of graphite – graphite is made up of layers of graphene stacked on top of each other. It is essentially a layer of sp^2 hybridized carbon atoms, arranged in a honeycomb (hexagonal) lattice structure. Graphene has excellent thermal and electrical properties – it has a thermal conductivity of 3000 – 5000 $Wm^{-1} K^{-1}$, and high mechanical strength of around 40 Nm^{-1}, with Young's modulus of 1 TPa. It also has a specific area of around 2600 $m^2 g^{-1}$, and carrier mobility of ~10,000 $cm^2 V^{-1}s^{-1}$ at room temperature – contributing to the high electrical conductivity of 10^6 Scm^{-1} [92, 93]. Graphene can be used to make carbon materials of different shapes – 0D fullerenes, 1D nanotubes, and 3D graphite. Figure 12 visualizes this.

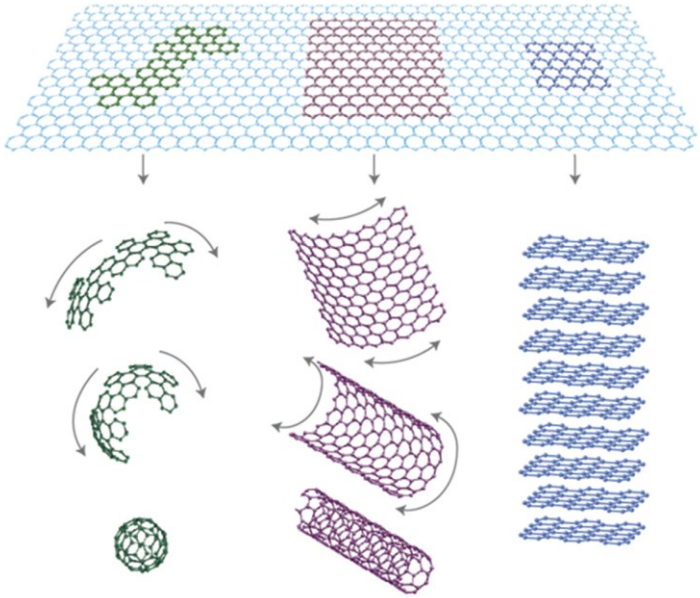

Figure 12: Various structures derived from graphene. Adapted from Kakaei et al. (2019) [92]

Due to its excellent properties in all the various categories, graphene has a wide range of uses. These include chemical sensors, electronic devices, catalysts, energy storage and conversion, green energy applications, etc. Graphene is also being increasingly used to dope metal oxides and producing composited with [92, 93]. As discussed by Heremans *et al.* [23], nanostructures can make excellent TE materials – graphene shows this kind of low dimensionality. However, there are some drawbacks to using graphene – it has a very high thermal conductivity, which negatively impacts the thermoelectric performance as the ZT was relatively low. This problem, however, can be solved in multiple ways as introducing controlled defects, introducing rough edges, edge passivation using hydrogen, patterning, and hybrid nano-structuring [94].

The positive impact of graphene on thermoelectric performance has also been observed in other systems. One such system includes the one studied by Du *et al.* [95]. Polyaniline (PANI) is a conducting polymer with a low thermal conductivity and can be quickly and cost-effectively processed. However, due to its unfavorable electrical properties, it has not been possible to use it as a TE material. The addition of graphene can solve this problem. Graphene nanosheets (GN) were added to the polyaniline in the ratios of 4:1, 3:1, 2:1, and 1:1 (PANI: GN) to prepare pellets and films. As the concentration of GN increased, the electrical conductivity and the Seebeck coefficient of both pellets and films increased. The carrier mobility also increased significantly when the GN concentration was increased, suggesting that this was why the thermoelectric performance improved upon the addition of graphene. The difference in the carrier concentration, however, was not significant. As observed from Figure 13, both the power factor and electrical conductivity (σ) are highest for an equal weight of GN and PANI.

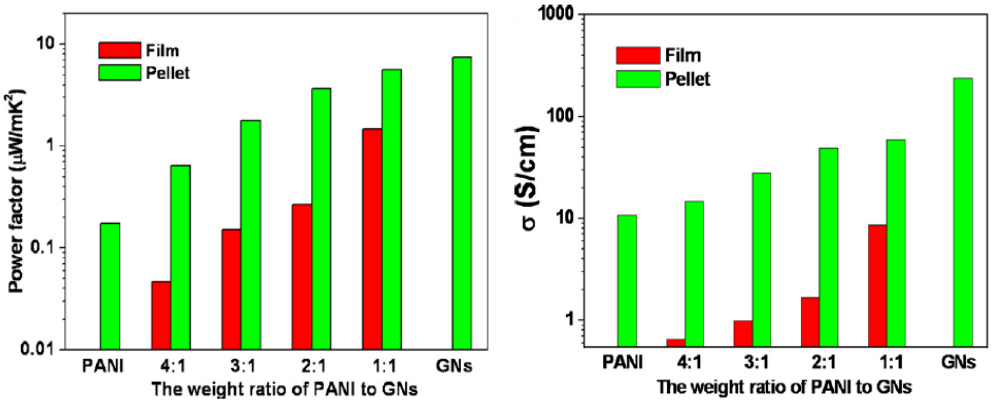

Figure 13: The relationship of power factor and electrical conductivity with PANI:GN ratio. Adapted from Du et al. (2012) [95]

2.4.3.1 Nanostructured Thermoelectric Material-Graphene Composites

Graphene has been added with and without other dopants to TE materials to improve their performance. Yang *et al.* [96] found that adding molybdenum disulfide with graphene (MoS_2/G) improves the thermoelectric performance of SnSe. A maximum ZT of 0.98 was achieved at 810 K. Also, the lattice thermal conductivity was decreased due to the introduction of grain boundary scattering.

Thermoelectric properties of Bi_2Te_3 were also found to have improved upon the addition of graphene. In studies carried out by Ahmad *et al.* [67], Liang *et al.* [97], and Ju *et al.* [98], the addition of graphene to Bi_2Te_3 was found to improve the thermoelectric performance. All studies showed a peak at one concentration of graphene, which differed for all three studies. Nevertheless, the addition of graphene improved the performance of Bi_2Te_3, proving that the addition of graphene should be favorable for TE materials.

Feng *et al.* [99] found that graphene was able to enhance the thermoelectric properties of $CoSb_3$, which is a very attractive TE material due to its favorable carrier motility and reasonable band gaps. The limitation of its high thermal conductivity was overcome by introducing a second graphene phase into the $CoSb_3$ nanostructure matrix in situ. It was found that adding 1.5 wt% graphene to the matrix dramatically improves the figure of merit without a significant adverse effect on the Seebeck coefficient. The variance of ZT is shown in Figure 14.

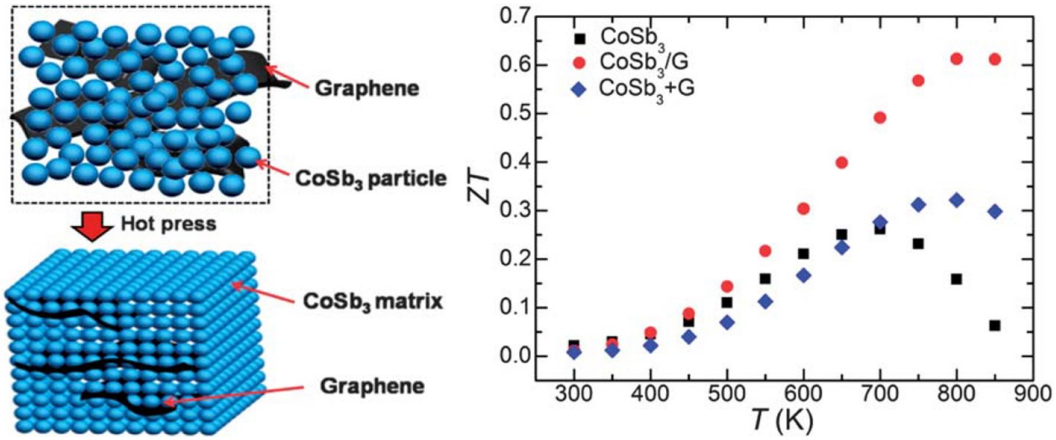

Figure 14: Material illustration and figure of merit (ZT) for $CoSb_3$ samples. Adapted from Feng et al. (2013) [99]

Certain TE materials, such as lanthanum strontium titanium oxide (LSTO), are limited in their application due to their high operating temperatures above 700 °C. Lin *et al*. [100] have been not only able to reduce the operating temperature by the addition of graphene but also demonstrated a small (0.6 wt.%) enhances the ZT by more than 280%. Figure 15 illustrates the ZT for different composites of LSTO with graphene.

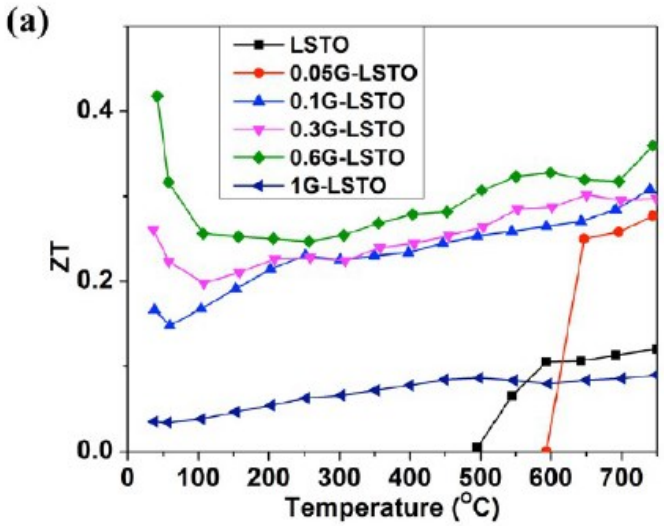

Figure 15: Variation of ZT with temperature for LSTO-Graphene composites. The peak value of ZT is reached at room temperature, for the composite with 0.6 wt% graphene. Adapted from Lin et al. (2015) [100]

The addition of graphene improves the TE properties due to several reasons. The lattice thermal conductivity of several materials, for example, Bi_2Te_3, $CoSb_3$, LSTO, and PbTe, was found to have decreased due to a reduction in the grain size, which increases the phonon scattering [67, 96, 99-101]. Phonon scattering was further enhanced due to the introduction of interfaces within the crystal structure, promoting a decrease in the lattice thermal conductivity. As the contribution to the overall thermal conductivity from lattice thermal conductivity is higher than the electronic contribution, the overall thermal conductivity decreases [98]. Graphene used as a filler also enhances the electrical conductivity, by either increasing the carrier concentration or carrier mobility [98, 99]. The thermal stability of composites can also be improved by the addition of graphene [101].

Due to the enhancement of the performance of TE materials upon the addition of graphene, it will be added to the materials prepared in this research to form nanocomposites and possibly further improve the properties of pure bismuth telluride and tin selenide. Doping will also be performed after the composites are synthesized to enhance the performance.

3. RESEARCH OBJECTIVES

The objective of this thesis research is to synthesize bismuth telluride and tin selenide-based graphene composites that could have potentially enhanced thermoelectric properties by using solution methods.

The goal of this research will be met by accomplishing the following objectives:

1. Preparing pure tin selenide and tin selenide nanocomposites with different concentration of graphene
2. Preparing pure bismuth telluride and bismuth telluride nanocomposites with different concentrations of graphene
3. Characterization of the prepared thermoelectric materials and their nanocomposites to establish the correlation between graphene content and the material properties.
4. Analyze the properties of the materials for possible thermoelectric applications.

4. METHODOLOGY

The general methodology of for this project can be seen in Figure 16:

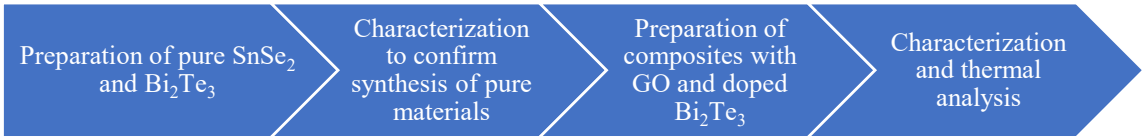

Figure 16: Flow chart of the methodology

4.1 Tin Selenide Fabrication

For the preparation of tin selenide, tin (II) chloride, $SnCl_2.2H_2O$, and selenium dioxide, SeO_2, were used as the precursors. The precursors were mixed in Sn: Se ratio of 1:2. 7 grams of $SnCl_2.2H_2O$, and 4.44 g of SeO_2 were added to a 250 mL beaker containing 150 mL deionized (DI) water. The solution was stirred for 30 minutes using a magnetic stirrer to ensure no clumps of the precursors remained. It was then bath sonicated for 30 minutes, and probe sonicated for 5 minutes (30 seconds on, 30 seconds off). The sonication was done to ensure the solution was homogenous before the reducing agent was added. The reducing agent used for this process was hydrazine hydrate, $N_2H_4.H_2O$. 20 mL of the reducing agent was added to the prepared precursor mixture. This solution was then transferred to a 200 mL Teflon liner, placed in an autoclave, and kept in the oven at 180 ˚C for 9 hours.

The autoclave was then removed from the oven, and the material obtained was centrifuged at 1500 rpm for 10 minutes and repeated five times, and the material was washed with DI water in between to ensure the reducing agent was removed. The material was then dried at 80 ˚C.

The hydrazine acts as the reducing agent, reducing both the Sn^{2+} and Se^{4+}, combining $SnSe_2$. The reaction mechanism can be described as follows [102]:

$$SeO_2 + H_2O \rightarrow H_2SeO_3 \quad (4.1)$$

$$H_2SeO_3 + N_2H_4.H_2O \rightarrow Se + N_{2(g)} + 4H_2O \quad (4.2)$$

$$2SnCl_2.2H_2O + N_2H_4.H_2O \rightarrow 2Sn + N_{2(g)} + 5H_2O + 4HCl \quad (4.3)$$

$$Sn + 2Se \rightarrow SnSe_2 \quad (4.4)$$

4.1.1 Tin Selenide-Graphene Composite Fabrication

For the preparation of tin selenide-carbon composite, a similar procedure to pure tin selenide preparation was followed. The preparation of the precursor mixture was unchanged, but 50 mL DI water was used instead. For the carbon, a graphene oxide (GO) precursor was used. Different concentrations of graphene oxide were used, as shown in Table 6. The graphene oxide solution was made in 100 mL DI water for all the different masses. It was bath sonicated for 15 minutes, followed by probe sonication for 5 minutes (30 seconds on, 30 seconds off). The precursor solution, the graphene oxide solution, and 20 mL hydrazine were added to a 200 mL Teflon liner. The liner was then placed in an autoclave and kept in the oven at 180 ˚C for 9 hours. A Similar centrifugation and drying procedures were followed for these composites as for the pure tin selenide.

Table 6: Mass of the precursors used for the synthesis of $SnSe_2$ and $SnSe_2$-graphene nanocomposites

Precursor	Mass (g)				
	% GO				
	0	**0.05%**	**0.1%**	**0.25%**	**0.5%**
$SnCl_2.2H_2O$	7.01	7.01	7.01	7.01	7.01
SeO_2	4.44	4.44	4.44	4.44	4.44
GO	0	0.0045	0.009	0.018	0.036

4.2 Bismuth Telluride Fabrication

The precursors used for the preparation of bismuth telluride were bismuth chloride, $BiCl_3$, and pure tellurium powder, Te. In a Teflon lined with 160 mL mixed solution of water and ethanol (50:50), 0.8 g of Hexadecyltrimethylammonium bromide (CTAB) was dissolved, followed by the addition of 8 mmol of $BiCl_3$ and 12 mmol Te. Sodium hydroxide, NaOH, was added to the solution until the pH was 11. For the Ag-doped Bi_2Te_3, $Ag_{0.011}$-Bi_2Te_3 was prepared, and a stoichiometric amount of silver precursor ($AgNO_3$) was added. This mixture was stirred for 15 minutes at room temperature. 32 mmol of sodium borohydride, $NaBH_4$, was then added to the mixture. The solution was sealed in an autoclave and was kept in the oven. The oven was maintained at 210 °C for, and the autoclave was removed after 24 hours. The products obtained were filtered in a dead-end cell and washed using distilled water and ethanol, followed by drying at 80 °C.

The reaction mechanism followed by the precursors to form Bi_2Te_3 can be described by the equations written below. Both ions and atoms can combine to form the material (following equations 4.7 and 4.8) [103].

$$Bi^{3+} + OH^- + BH_4^- \rightarrow Bi + H_2BO_3^- + H_2 \quad (4.5)$$

$$Te + BH_4^- \rightarrow Te^{2-} + H_2BO_3^- + H_2 \quad (4.6)$$

$$2Bi + 3Te \rightarrow Bi_2Te_3 \quad (4.7)$$

$$2Bi^{3+} + 3Te^{2-} \rightarrow Bi_2Te_3 \quad (4.8)$$

4.2.1 Bismuth Telluride-Graphene Composites

For the preparation of tin selenide-carbon composite, a similar procedure to pure tin selenide preparation was followed. The preparation of the precursor mixture was unchanged – the mass used for the precursors and the reducing agent remain the same. For the carbon, a graphene oxide (GO) precursor was used. A GO solution of concentration 1 mg/mL was prepared - an equivalent volume of the GO solution was used as the required mass. It was bath sonicated for 15 minutes, followed by probe sonication for 5 minutes (30 seconds on, 30 seconds off). Different concentrations of graphene oxide were used, as shown in Table 7.

Based on the required volume of the graphene solution, the volume of the precursors' solution was adjusted to ensure the total volume did not exceed 160 mL. The liner was then placed in an autoclave and kept in the oven at 180 ˚C for 24 hours. The autoclave was allowed to cool to room temperature naturally. The products obtained were filtered in a dead-end cell and washed using distilled water and ethanol, followed by drying at 80 °C.

Table 7: Mass of the precursors used for the synthesis of Bi_2Te_3-based materials

Precursor	Mass (g)			
	Sample			
	Pure	**Doped**	**0.25%**	**0.5%**
$BiCl_3$	2.52	2.52	2.52	2.52
Te	1.53	1.53	1.53	1.53
GO	0	0	8.02	16.04
$NaBH_4$	1.21	1.21	1.21	1.21
CTAB	0.8	0.8	0.8	0.8
$Ag(NO_3)$	0	0.0075	0	0

4.3 Characterization

Several characterization tests have been and will be performed for this research, summarised in Table 8. They are described in the sections below.

Table 8: Characterization tests performed on the synthesized materials

Materials	Tests							
	XRD	XPS	SEM	TEM	TGA	DSC	k	Hardness
$SnSe_2$	✓	✓	✓	✓	✓	✓	✓	✓
Bi_2Te_3	✓	✓	✓		✓	✓		

4.3.1 Chemical and Structural Properties

4.3.1.1 X-Ray Diffraction (XRD)

X-Ray Diffraction (XRD) is used to reveal the crystal structure and chemical composition of materials. It is a non-destructive test, and structural parameters, such as

the average grain size, the crystallinity, the strain, and the crystal defects, can also be obtained. X-rays are scattered by the different lattice planes within a sample. Peaks are obtained due to the constructive interference of x-rays scattered at specific angles [104]. The diffraction from a crystal can be described by Bragg's law, which is given as $\lambda = 2d\sin\theta$, where d is the interplanar spacing, λ is the wavelength of the x-rays, and θ is the diffraction angle or the Bragg angle.

Scherrer's equation is usually used to determine the crystal size [105]:

$$D = \frac{0.9\lambda}{\beta_d} . \frac{1}{\cos\theta} \tag{4.9}$$

where λ and θ are the same as in Bragg's law, and β is the full width at half maximum (FWHM).

However, the Scherrer equation assumes that only the size of the crystals affects the peak broadening, which is inaccurate because the ambient temperature and the lattice strain also affect the width of the peak [106]. Several methods can be used to overcome this, including :

- The **Modified Scherrer** equation can be used, which used a logarithmic model to calculate the crystallite size. This approach reduces the error in the calculation [107].
- The **Williamson-Hall (W-H)** approach employs a uniform deformation model, a uniform stress deformation model, and a uniform deformation energy density model to obtain the lattice stress and strain parameters yielding a more accurate prediction of the crystallite size [105].

- The **Warren-Averbach (W-A)** approach uses Fourier-coefficient analysis model and can be applied to a curve of any shape if the tails are correctly truncated. It yields a crystallite size in a good agreement with that obtained experimentally [108].
- The **Size-Strain Plot (SSP)** method models the size broadening as a Lorentzian function and the strain broadening as a Gaussian function. This method gives more importance to the lower angle peaks as they have more accuracy and precision compared to higher diffractions angles, where the peaks generally overlap [105].
- The **Halder-Wagner (HW)** method follows the peak broadening as a Voight function. The Voight function is a convolution of Lorentzian and Gaussian functions. XRD peak profiles do not match either fully but have elements of both, which make the HW method accurate as well [105].

In this research, the XRD was carried using Ultima IV X-ray Diffractometer in a scan range of 10˚ to 80˚, with a speed of 1˚/minute. CuK (alpha) (0.1542 nm) radiation at 40 kV and 20 mA was used in this analysis.

4.3.1.2 X-ray Photoelectron Spectroscopy (XPS)

In X-ray Photoelectron Spectroscopy (XPS), the surface of the material is hit with X-rays under vacuum, causing electrons to be released from the surface. The elemental composition can be obtained for the material as every element will release specific electrons. Additionally, the chemical state of the elements in the material can also be obtained – this can be used to determine what bonds are present in the material. The information obtained from the binding energy of the various elements is compared to the binding energy of the C-C bond, which is always present in the results. It is a non-

destructive technique [104]. For this thesis research, XPS was used to determine the chemical state of bismuth, tellurium, tin, and selenium in their compounds. XPS is also used to quantify the elemental composition

4.3.1.3 Scanning Electron Microscopy (SEM)

Scanning Electron Microscopy (SEM) is used to obtain images of the surface of a material. Unlike XRD and XPS, in SEM, an electron beam is used in this technique. A focused beam of electrons strikes the surface of the material, resulting in the emission of electrons and photons. This interaction produces an image of the surface. The emitted particles are collected by different detectors to yield the results, one of which is used for EDS, discussed in the next section. SEM is performed in a vacuum environment [104, 109]. For this project, the analysis was performed the FEI Quanta 400 Environmental SEM, in high vacuum and on 30 kV.

4.3.1.4 Energy Dispersive X-ray Spectroscopy (EDS)

Energy-dispersive X-ray Spectroscopy (EDS) gives the composition of a small area on the surface of the material. It is performed in combination with SEM analysis. When an electron beam strikes a surface, x-rays are also emitted. These x-rays have specific wavelengths that are attributed to different elements. As a result, the elemental composition of the area studied can be obtained [109]. The EDS was performed in conjunction with the SEM, using the EDAX Octane Elect EDS System.

4.3.1.5 Transmission Electron Microscopy (TEM)

Transmission Electron Microscopy (TEM) is a powerful technique that can give the crystal structure, deformations within the structure, and morphology of the material.

In TEM, imaging of structures at the atomic scale is possible. Similar to SEM, TEM employs electrons. However, in TEM, the electrons are transmitted through the material, and the image is formed using the transmitted electrons collected on a fluorescent screen, as shown in Figure 17. The orientation of the crystal planes can also be determined using TEM.

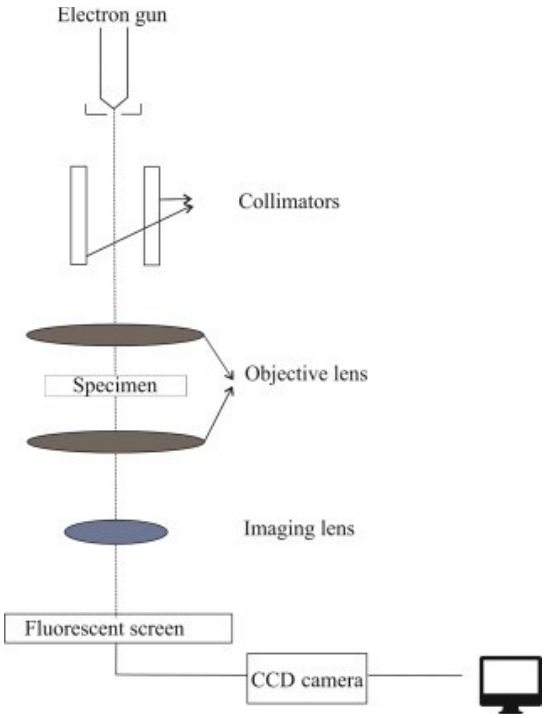

Figure 17: Working principle of a TEM

4.3.2 Thermal Properties

4.3.2.1 Thermogravimetric Analysis (TGA)

Thermogravimetric analysis is carried out to analyze the thermal stability of materials and also the content of the volatile compound, by monitoring the weight change of the material as it is heated at a constant heating rate. The temperature range in which TGA is conducted depends on the material used. The obtained thermogram of weight versus temperature can also be used to determine the presence of decomposition, oxidation, or dehydration that may occur during heating. TGA can be carried under several environments, including nitrogen, oxygen, air, or vacuum [110]. In this thesis research, TGA was carried out using Discovery TGA (TA Instruments) at the temperature range of 50 °C to 600 ˚C and a heating rate of 10˚ C/minute under nitrogen environment.

4.3.2.2 Differential Scanning Calorimetry (DSC)

Differential scanning calorimetry (DSC) is a thermal analysis technique in which the difference in the amount of heat required to maintain the temperature of the sample and the reference to follow the programmed temperature scan is recorded. Both materials are maintained at the same temperature throughout the experiment. The melting point, specific heat capacity, heat of fusion, and heat of vaporization of a material can be obtained from this technique [111]. For this research, DSC was carried out from ambient temperature to 450 ˚C. This test was used for obtaining the heat capacity of the synthesized materials, so calculations for the thermal conductivity could be carried out.

4.3.2.3 Thermal Conductivity

The thermal conductivity of thermoelectric materials is an essential property. The thermal conductivity was measured using a LINSEIS LFA 500 Laser Flash, shown in Figure 18. The LFA-500 measures the thermal diffusivity (α) of the sample, and the thermal conductivity is determined from the following relation:

$$\lambda = \alpha \rho C_p \tag{4.10}$$

where, C_p is the specific heat capacity and ρ is the density.

The specimens for measurement were pressed in 25.4 mm disks with a thickness of 0.5 – 2 mm.

Figure 18: Thermal conductivity testing equipment

4.3.3 Mechanical Properties

4.3.3.1 Hardness Measurement

To analyze the mechanical properties of the synthesized materials, the microhardness of these materials was measured. For these measurements, the nanopowders were pressed into small disks. A pyramidal indenter with a square base makes an indentation on the surface of the disk. The hardness of the material is determined by the prediction size of the indentation and the used load [112]. Figure 19 shows an illustration of the indenter and indentation.

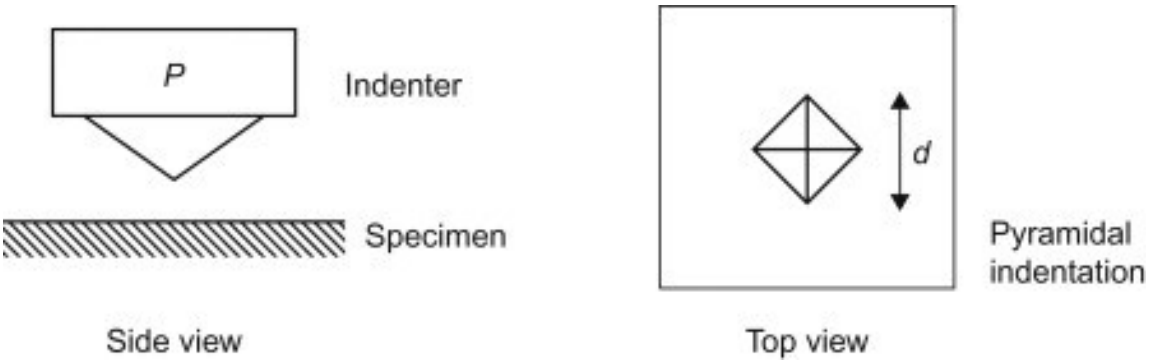

Figure 19: Indenter and indentation made for the microhardness measurements. Adapted from Smallman & Ngan (2014) [113]

5. RESULTS AND DISCUSSION

5.1 Tin Selenide and Tin Selenide-Graphene Nanocomposites

Pure tin selenide and tin selenide-graphene nanocomposites with different graphene concentrations were synthesized via a hydrothermal approach. A yield higher than 90% was obtained for all materials. The structure and morphology of the pure and nanocomposite samples are analyzed using XRD SEM, TEM, and XPS. The hardness of these materials was also measured, and the results are discussed in the following section.

5.1.1 Chemical and Structural Properties

Figure 20 shows the XRD patterns for the pure $SnSe_2$ synthesized material and the GO composites. The peaks correspond to $SnSe_2$, confirming its presence. The diffracted lattice planes are identified in Figure 20, with the $(10\overline{1})$ plane having the highest intensity. The XRD patterns for the composites show a broader peak near 28° reported for $SnSe_2$ [114]. The intensities for the peak differ for the composite. However, the peak corresponding to the $(10\overline{1})$plane has the highest intensity. Although most peaks in the diffraction pattern correspond to $SnSe_2$ (JCPDS No. 89-3197), there are peaks at 27.5 and 34.8°, which are not consistent with the $SnSe_2$ patterns. This extra peak could be due to the presence of oxides within the material. SnO_2 has a peak at 26.5° and 34°, which could correspond to the observed peaks [115]. For the composite samples, the presence of selenium is identified by the peaks at 23.5°, 29.7°, and 51.8° in the XRD patterns and it was also confirmed by the XPS analysis of the composites.

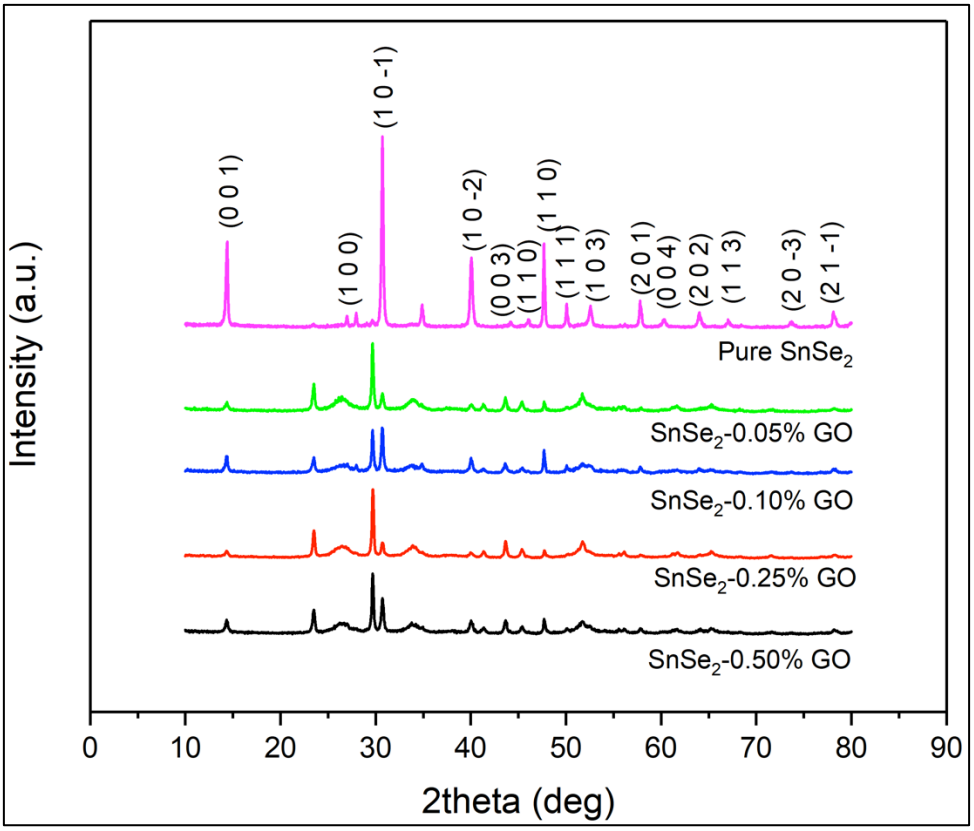

Figure 20: XRD of $SnSe_2$ and $SnSe_2$ Composites

An interplanar spacing of 0.29 nm was obtained for the $(10\bar{1})$ plane, using Bragg's law. The grain size for the crystals was determined using the Williamson-Hall Method. The equation used was:

$$\beta \cos\theta = 4\varepsilon \sin\theta + \frac{k\lambda}{D} \qquad (5.1)$$

where, β represents the peak broadening due to the crystal size and the strain, ε represents the strain, and θ is the diffraction angle. Figure 21 shows the linear fit for βcosθ vs 4sinθ. The grain size obtained using this method was 31.54 nm.

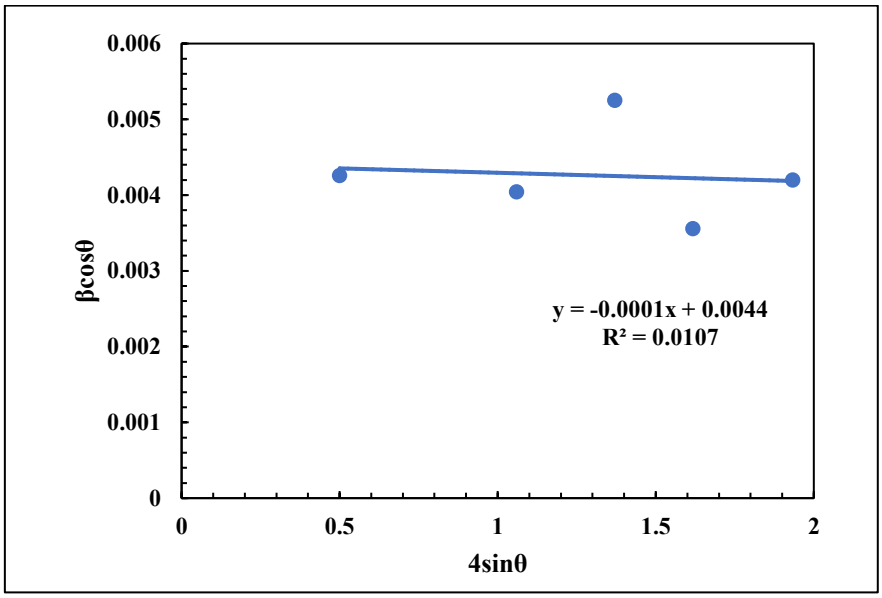

Figure 21: Williamson-Hall linear fit for pure $SnSe_2$ nanopowders

However, as the R^2 squared value obtained from the Williamson-Hall method did not suggest a good fit, the data were also analyzed using the Warren-Averbach method. The equation for the Warren-Averbach method is as follows:

$$\frac{\beta^2}{\tan^2\theta} = \frac{\lambda}{D}\left(\frac{\beta}{\tan\theta \sin\theta}\right) + 25e^2 \qquad (5.2)$$

Figure 22 shows a linear fit for $\frac{\beta^2}{\tan^2\theta}$ vs $\frac{\beta\lambda}{\tan\theta \sin\theta}$, The grain size and strain were obtained from the slope and the intercept, respectively. The R^2 for the Warren-Averbach method is higher, suggesting that this method is a better fit. The grain size was 36.5 nm, and the strain was 0.04 %.

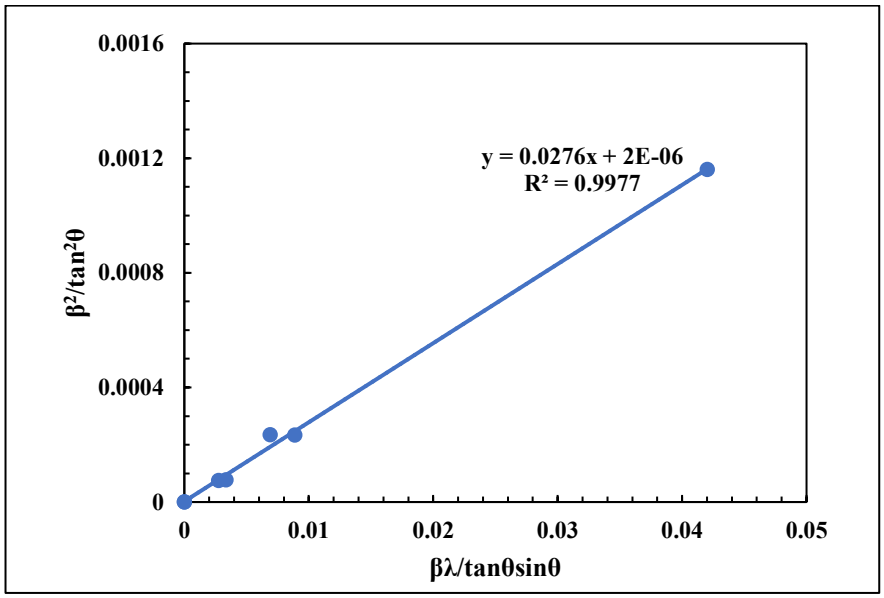

Figure 22: Warren-Averbach linear fit for pure $SnSe_2$ nanopowders

The procedure mentioned earlier was followed to obtain the grain sizes of the $SnSe_2$ composites with graphene, and the results are summarised in Table 9. The results show that the addition of graphene reduces the grain size of the materials, with the smallest grain size of 25.1 nm for the 0.5% GO nanocomposite. The lack of a clear trend in the grain size calculations could be due to the presence of selenium within the graphene nanocomposites, which could have affected the grain size of our obtained products. Nevertheless, there was a decrease of 31.3% upon the addition of 0.5% GO. The Warren-Averbach model suggested a better fit for the composites, similar to the pure $SnSe_2$ linear fits. The linear fits for the composites can be found in Appendix A.1.

Table 9: Grain sizes for pure $SnSe_2$ and $SnSe_2$-Graphene composites obtained using Scherrer, Williamson-Hall, and Warren-Averbach methods

GO Concentration (%)	Grain Size (nm)		
	Scherrer's Method	**Williamson-Hall**	**Warren-Averbach**
0 (Pure)	33.1	31.5	36.5
0.05	26.7	33.00	25.4
0.1	28.9	23.9	29.3
0.25	27.2	29.5	35.07
0.5	27.6	22.3	25.1

In addition to XRD, XPS was carried out to investigate the chemical states of the elements and their composition. Figure 23 (a) and (b) show the spectra for Sn 3d and Se 3d. The Se spectrum has only two peaks at 54.5 eV, 55.4 eV, corresponding to $SnSe_2$, and 487 eV and 495.4 eV, corresponding to SnO_2. Table 10 summarises the elemental quantification of the materials, showing a large amount of oxygen due to the presence of the oxides.

Figure 24 shows the spectra obtained for $SnSe_2$-0.50% GO verifies what was observed in the XRD – the presence of two phases, both $SnSe_2$ and Se. The binding energies of 53.6 and 54.5 eV correspond to Se^{2-} in $SnSe_2$, and the binding energy of 55.5 eV corresponds to pure selenium. The presence of tin oxide is once again observed in the tin spectra – the 3d peaks for tin appeared at 486 eV and 494.4 eV, and 488 eV and 496.4 eV. The former corresponds to Sn^{4+} in $SnSe_2$, while the latter corresponds to its presence SnO_2. The peak for oxygen at 532 eV corresponds to moisture absorbed on the surface [116], and the peak at 529.7 corresponds to oxygen in the Sn-O bond.

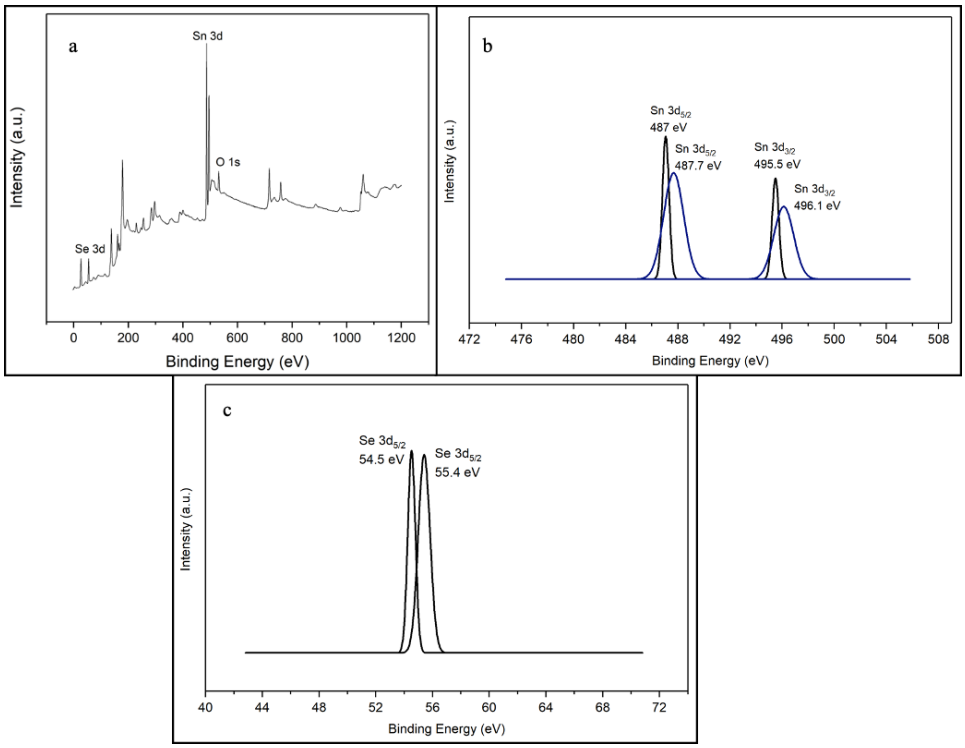

Figure 23: (a) Survey spectra of the pure $SnSe_2$, (b) Sn 3d scan, (c) Se 3d scan

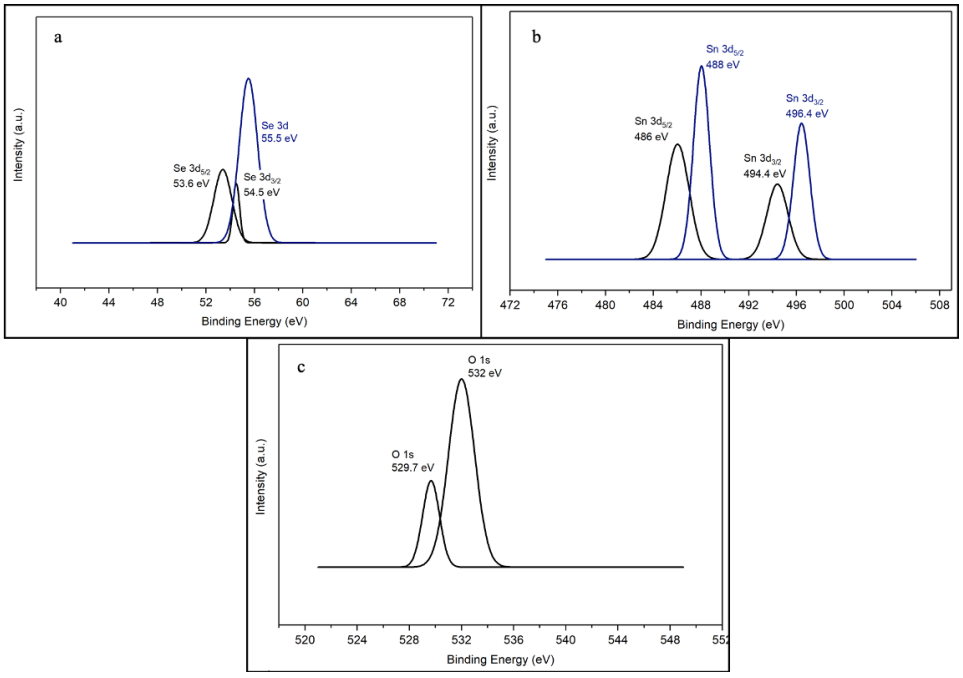

Figure 24: $SnSe_2$-0.50% GO: XPS spectra of (a) Se 3d, (b) Sn 3d, and (c) O 1s

Table 10: Composition of $SnSe_2$ and $SnSe_2$-Graphene composites

Graphene	0 wt.%	0.05 wt.%	0.1 wt.%	0.25 wt.%	0.5 wt.%
	Composition (at. %)				
Sn	20.7	22.2	23.9	18.7	20.5
Se	8.1	5.8	5.0	6.6	7.1
C	29.8	26.5	23.5	33.5	33.5
O	41.9	45.5	47.5	41.3	38.9

Figure 25 shows the SEM images for $SnSe_2$ and its composites. Hexagonal plates are visible in all images. However, rod-like structures are also observed. The nanoparticles had an irregular shape for all the composites, with the $SnSe_2$-0.25% GO composite having the most irregular structure (Figure 25 (j,k,l)). The presence of sphere-like structures was also observed. The thickness of the plates was 450.9 nm in the pure $SnSe_2$, but with the presence of large agglomerates. The thickness of the plates in the $SnSe_2$-0.50% GO composite was 89 nm. The size of the sphere-shaped nanoparticles was estimated to be between 5 to 20 nm.

To further analyze the structure of the synthesized compounds, TEM analysis was performed. Figure 26 shows the results for the TEM. The interplanar spacing obtained from the TEM images was 0.34 nm for all materials. It was also visible that the materials formed had a hexagonal shape, with the images of 0.10% GO composite showing some more irregular shapes. It is not easy to differentiate between the reduced graphene oxide and tin selenide phases, and there is a high amount of agglomeration observed due to the powder not being appropriately dispersed before running the analysis.

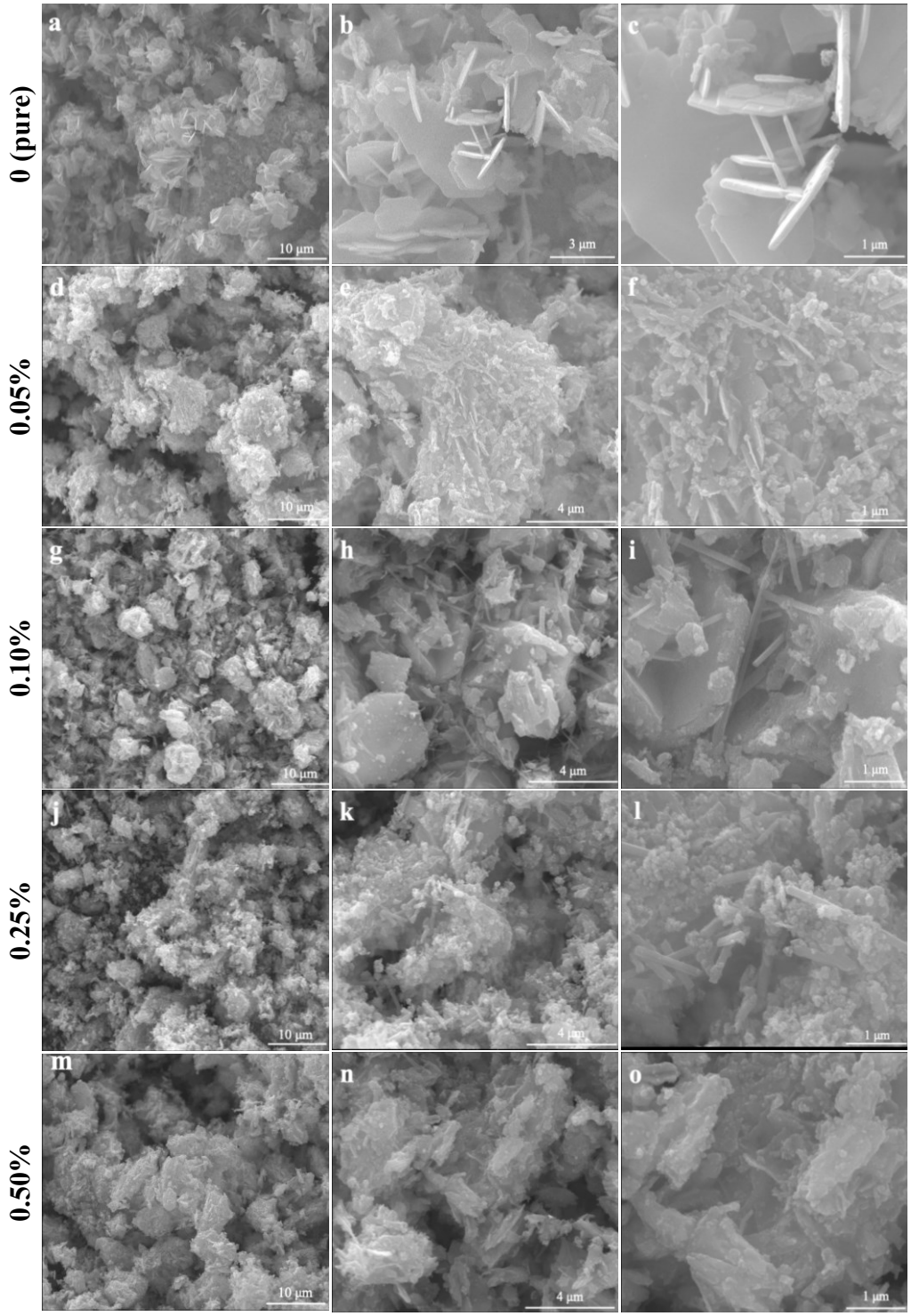

Figure 25: SEM images of $SnSe_2$ and $SnSe_2$-Graphene composites

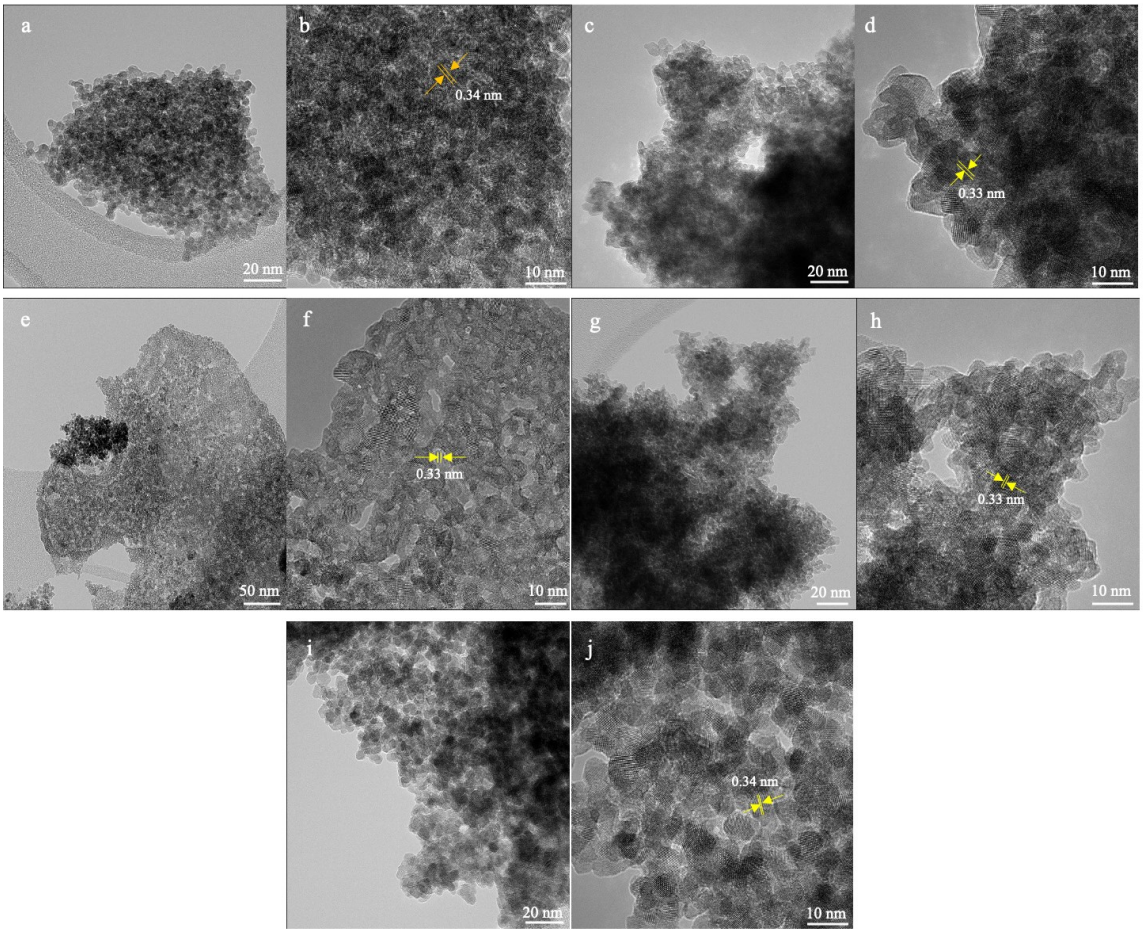

Figure 26: TEM images of (a,b) pure $SnSe_2$, (c,d) $SnSe_2$-0.05% GO, (e,f) $SnSe_2$-0.10% GO, (g,h) $SnSe_2$-0.25% GO, and (i,j) $SnSe_2$-0.50% GO

5.1.2 Thermal Properties

As shown in Figure 27, DSC was performed for the $SnSe_2$-GO composites. DSC is an essential thermal analysis technique as it can provide the melting temperature of a material, which is an essential factor to consider when the material is sintered for TE testing. It can be used to obtain the maximum service temperature of a material. The analysis was done from ambient temperature to a temperature of 450 ˚C. This test was also

performed so the specific heat capacity, Cp, could be determined for the material, as required for the measurement of thermal conductivity.

An endothermic peak was observed around 215 ˚C for all samples, correlating to the melting point of Se (220 ˚C). No exothermic phase transformations were present near the same temperature for the composites. An endothermic peak was also observed below 100 ˚C for all composites, attributed to the evaporation of residual water or ethanol. Table 11 summarises all thermal parameters obtained from the DSC analysis.

Table 11: Thermal parameters for $SnSe_2$ and $SnSe_2$-GO composites obtained from DSC analysis

Material	**Onset Temperature, T_o (°C)**	**Peak Temperature, T_p (°C)**	**ΔH_{fusion} (J/g)**
Pure $SnSe_2$	195.3	211.7	9.79
$SnSe_2$-0.05% GO	203.7	216.7	20.1
$SnSe_2$-0.10% GO	208.3	216.7	8.55
$SnSe_2$-0.25% GO	208.8	216.8	18.5
$SnSe_2$-0.50% GO	195.3	214.7	15.0

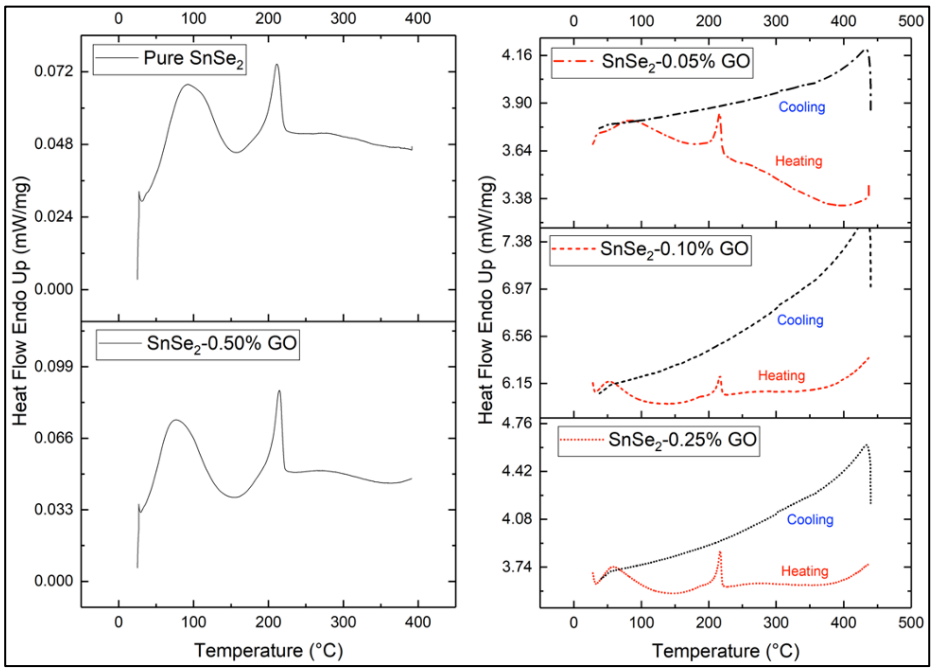

Figure 27: DSC thermograms of $SnSe_2$-GO composites, performed from ambient to 450 ˚C under N_2 atmosphere

The thermal stability of pure $SnSe_2$ and $SnSe_2$-graphene composites was evaluated using TGA. The materials showed poor thermal stability, as evident in Figure 28. The mass of the tested samples decreased to around 59%, with the highest GO loading composites losing the most mass (0.25% and 0.5%). No clear pattern was observed, as the composite with 0.1% GO lost the least mass. The composites with 0.25% and 0.50% GO appear to stabilize after a temperature of 500 ˚C, while the rest do not. A decrease in mass starts at 300 ˚C, but the simultaneous DSC signal does not show any thermal transformations at this temperature. This trend was not previously reported for $SnSe_2$.

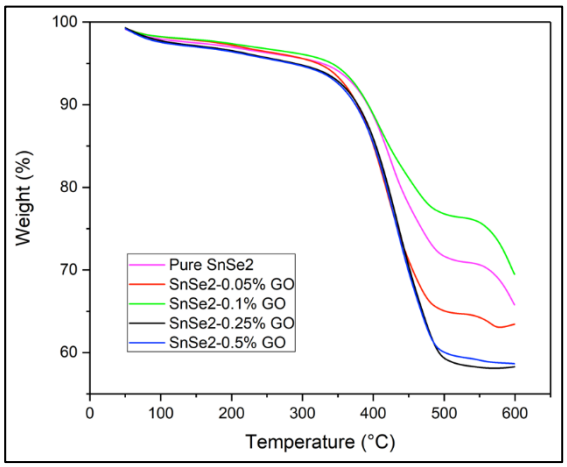

Figure 28: TGA for $SnSe_2$ and $SnSe_2$-Graphene composites heated at 10 ˚C/min under N_2 atmosphere

Thermal conductivity testing was carried at room temperature for the pure $SnSe_2$ and the $SnSe_2$-graphene nanocomposites. The Cp was 0.41 J/g.°C and 0.36 J/g.˚C for the pure SnSe2 and the composite sample, respectively, as measured by DSC. The thermal diffusivity measured by the laser flash technique is used to calculate the thermal conductivity using $\kappa = \alpha\rho C_p$ was used to calculate the thermal conductivity. The thermal conductivity is the lower for $SnSe_2$ having graphene oxide loading of 0.5%. This value is 0.41 ± 0.01 W m^{-1} K^{-1}. The thermal conductivity of the pure $SnSe_2$ sample was determined to be 0.60 ± 0.01 W m^{-1} K^{-1}. Compared to the thermal conductivity of the pure $SnSe_2$, there was a 31.7% decrease. The results can be seen in Figure 29.

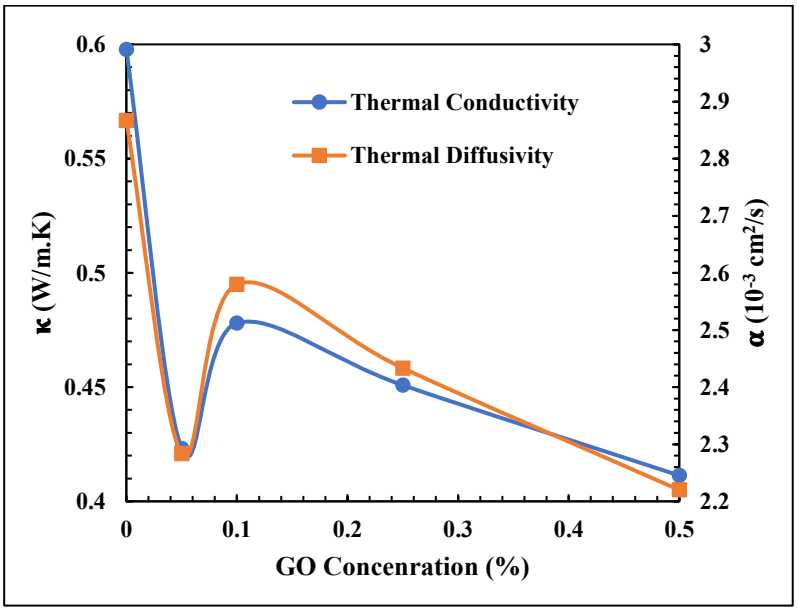

Figure 29: Thermal conductivity, k, and thermal diffusivity, α, for the $SnSe_2$-graphene nanocomposites

The trend followed by the samples is decreasing thermal conductivity as the GO concentration increases. The thermal diffusivity follows the same trend. The thermal diffusivity showed a decrease of 26% at the highest graphene loading, decreasing from 0.003 cm^2/s to 0.0022 cm^2/s. There is a minimum in κ at 0.05% graphene loading.

Although the lowest κ is obtained for the 0.50% GO nanocomposite, a similar κ was also observed for the 0.05% GO nanocomposite, attributed to the significant grain size reduction in the 0.05% GO nanocomposite, as observed in Table 9. Both nanocomposites showed a similar trend in the grain size reduction, with the decrease in the grain size for the 0.50% GO being higher. To better understand the effect of graphene on the thermal conductivity, more nanocomposites with lower graphene concentration should be formed, and their thermal conductivities measured.

The thermal conductivity for the synthesized $SnSe_2$ is lower than that is reported for $SnSe_2$ nanomaterials, shown in Table 12. This lower thermal conductivity is particularly significant compared with that of $SnSe_2$ prepared using hydrothermal methods, as the thermal conductivity obtained in this study is the lowest for the pure $SnSe_2$. Additionally, the reported thermal conductivity of the doped $SnSe_2$ is also higher than both the pure $SnSe_2$ and the $SnSe_2$-graphene nanocomposites prepared in this study, which is a very promising result. A further decrease in κ could be obtained by doping the graphene nanocomposites and optimizing the dopant and the doping concentration.

Table 12: Thermal conductivities of $SnSe_2$-based materials from literature

Preparation Technique	**Filler**	**$\kappa_{undoped}$, κ_{doped} (W/m.K)**	**Ref.**
Solution-based synthesis and hot pressing	No filler	0.44, -	[78]
Solution-based synthesis and hot pressing	Chlorine	0.42, 0.67	[83]
Vacuum melting and hot pressing	Chlorine	1.9, 2.05	[84]
Hydrothermal synthesis and SPS	Ag introduction and chlorine doping	1.65, 1.22	[85]
Hydrothermal synthesis and SPS	AgCl	1.15, 1.05	[86]
Solid-state method and SPS	Chlorine	1.53, 1.39	[87]
Ball milling	Silver	2.98, 2.60	[88]
Hydrothermal synthesis and SPS	Chlorine	1.18, 1.24	[89]
Melting, quenching, and hot pressing	Bromine	1.10, 1.40	[90]
Vacuum melting and hot pressing	Chlorine	1.0, 1.10	[91]

5.1.3 Mechanical Properties

The hardness of pure $SnSe_2$ (0.69 GPa) is consistent with reported cross-plane hardness in the of 0.71 GPa, which is twice the in-plane hardness of 0.35 GPa [117].

Figure 30 shows that the hardness increases as the concentration of graphene increases with a 26% increase in hardness with 0.5 wt.% graphene, revealing the excellent reinforcing effect of graphene and suggesting good dispersion in the $SnSe_2$ matrix.

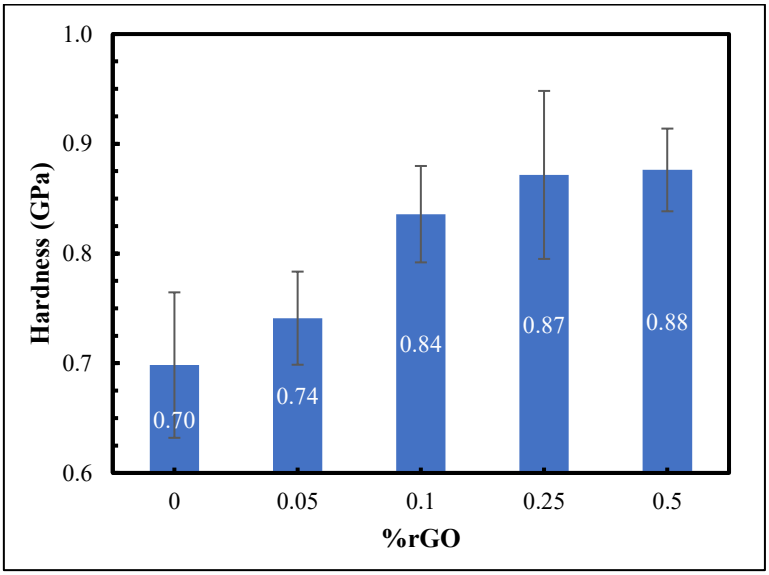

Figure 30: Effect of graphene loading on the hardness of $SnSe_2$

5.2 Bismuth Telluride Based Materials

Bismuth telluride and its composites were synthesized via a solvothermal approach. So far, the following materials have been synthesized for Bi_2Te_3:

- Pure Bi_2Te_3,

- Doped pure Bi_2Te_3,
- Bi_2Te_3-graphene composites (0.5% and 0.25% GO).

A yield higher than 95% was obtained for all four materials. Their structure was studied by performing XRD and XPS, and the thermal behavior of these materials was studied using TGA.

5.2.1 Chemical and Structural Properties

Figure 31 shows the XRD patterns of the synthesized pure Bi_2Te_3 and the composites with GO. The peaks confirm the synthesis of Bi_2Te_3. Bi_2Te_3 has a characteristic peak at 27.6˚, which represents the (1 0 4) plane. The composite spectrum shows two extra peaks at 30.48˚ and 32.26˚, attributed to Bi_2O_3 [118, 119]. The presence of oxides can be confirmed with XPS analysis.

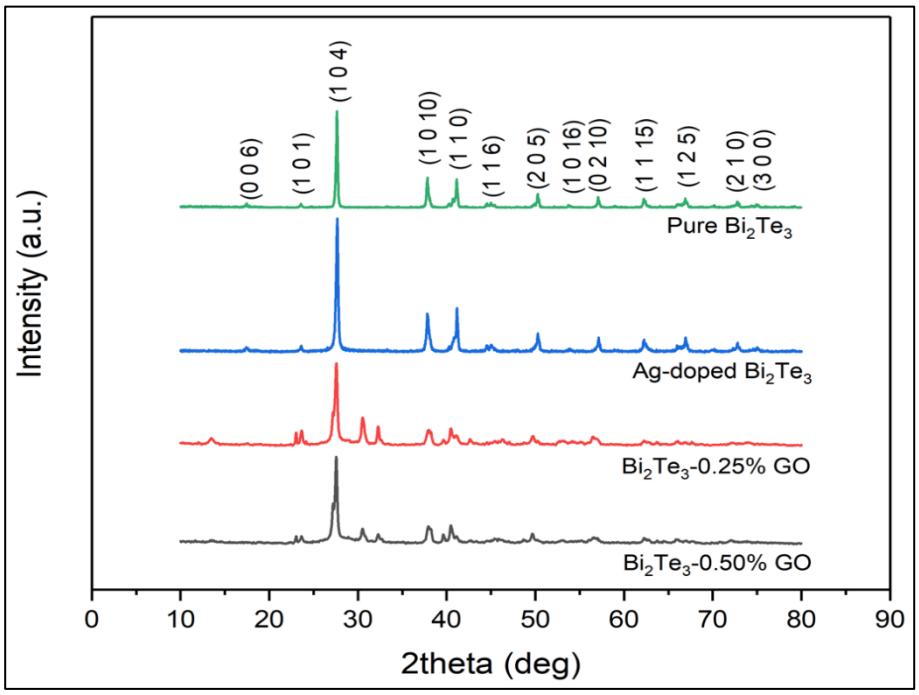

Figure 31: XRD patterns of pure Bi_2Te_3 and Bi_2Te_3-graphene composites.

For pure Bi_2Te_3, further analysis was carried out. The interplanar distance of the (1 0 4) plane was 0.322 nm, obtained using Bragg's Law. The grain size was calculated using the Williamson-Hall method, and the same procedure as detailed in Section 5.1.1 Chemical and Structural Properties was followed. The average grain size for the crystals was found to 36.5 nm. The linear fit plot can be seen in Figure 32. A strain of 0.46% was determined.

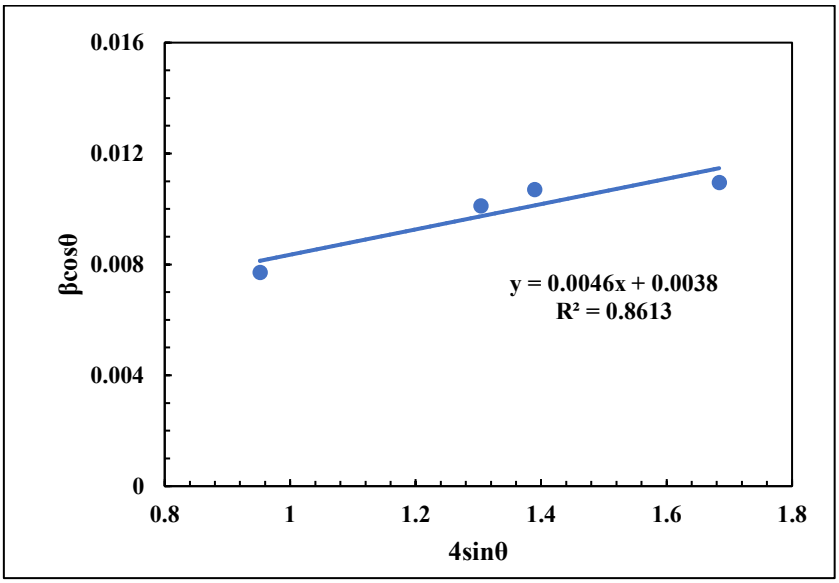

Figure 32: Williamson-Hall linear fit for pure Bi_2Te_3 crystals

The R^2 value suggests a good fit for the data. However, the analysis was also repeated using the Warren-Averbach method as it was a more accurate model for $SnSe_2$. Figure 33 shows a linear fit for $\frac{\beta^2}{\tan^2\theta}$ vs $\frac{\beta\lambda}{\tan\theta\sin\theta}$,. The grain size and strain were obtained from the slope and the intercept, respectively. The R^2 value for the Warren-Averbach method is lower, suggesting that the Williamson-Hall method is a better fit. The grain size was 33 nm, and the strain was 0.44 %.

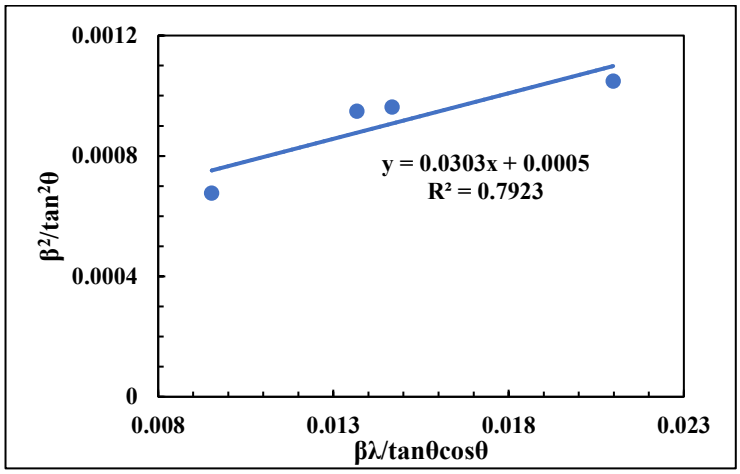

Figure 33: Warren-Averbach linear fit for pure Bi_2Te_3 crystals

Similarly, the grain size for the doped Bi_2Te_3 and the GO composites were also calculated. Unlike the pure crystals, the Warren-Averbach method was found to be a better fit. The grain size decreased significantly upon the addition of graphene and upon doping with silver. The smallest grain size was found for the 0.50% GO nanocomposites, showing a decrease of 54.7% as compared to the size of the pure Bi_2Te_3.

Table 13 summarises the strain and grain sizes calculated by the Scherrer, Williamson-Hall, and Warren-Averbach methods.

Table 13: Grain size of pure Bi_2Te_3 and Bi_2Te_3-based materials obtained using Scherrer, Williamson-Hall, and Warren-Averbach methods

Description	**Grain Size (nm)**		
	Scherrer's Method	**Williamson-Hall**	**Warren-Averbach**
Pure Bi_2Te_3	14.35	36.52	33.00
Ag-doped Bi_2Te_3	23.68	21.03	15.34

Table 13 Continued

Description	Grain Size (nm)		
	Scherrer's Method	Williamson-Hall	Warren-Averbach
Bi_2Te_3-0.25% GO	20.28	27.76	19.16
Bi_2Te_3-0.50% GO	17.29	9.64	14.99

However, the Ag-doped material also showed a significant decrease, suggesting an even smaller grain size could be obtained upon combining the doping and graphene nanocompositing techniques. The graphs for all composites can be found in Appendix A.2.

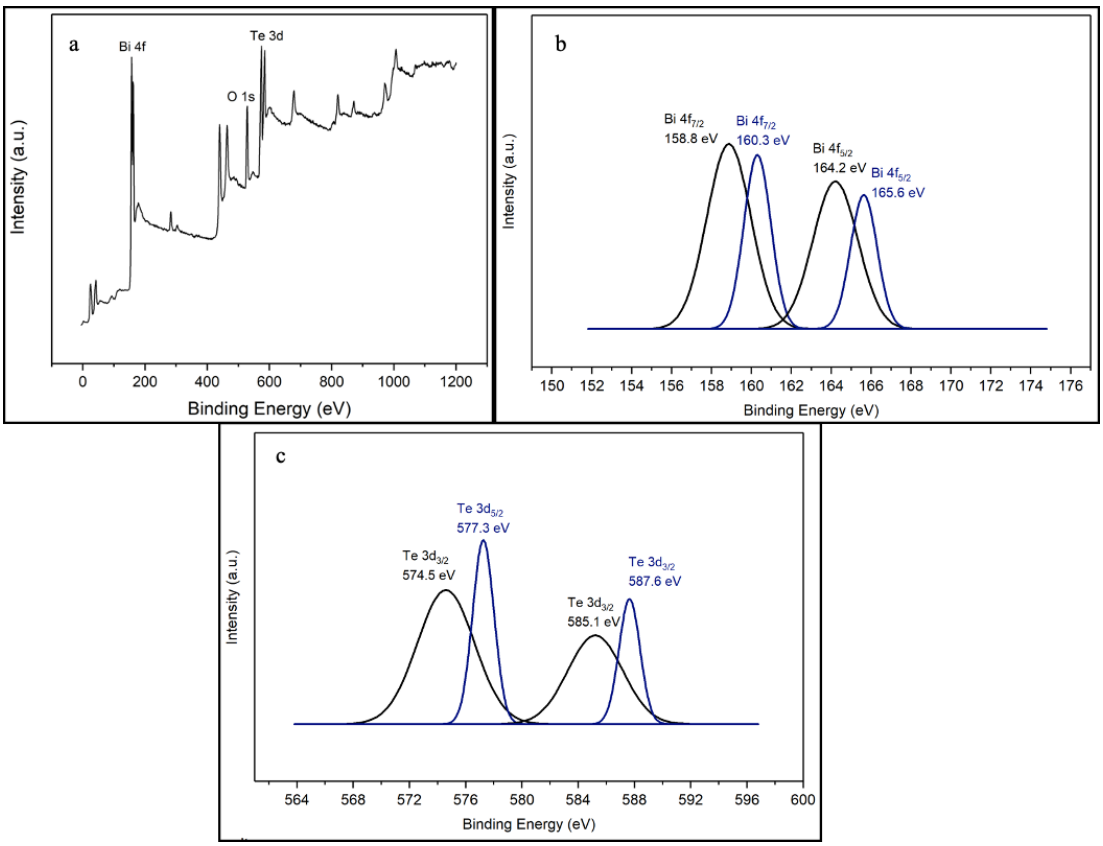

Figure 34: (a) Survey spectra of the pure Bi_2Te_3, (b) Bi 4f scan, (c) Te 3d scan

XPS confirmed the synthesis of Bi_2Te_3, with both Bi and Te spectra showing peaks that correspond to Bi_2Te_3. Figure 34 (b) and (c) show the spectra obtained for Bi 4f and Te 3d, respectively. Four peaks were observed for Bi 4f – two at 157.8 eV and 163.1 eV, which can be attributed to Bi_2Te_3. The peaks at 158.8 eV and 164 eV correspond to bismuth oxide, Bi_2O_3 [120]. Similarly, four peaks were also observed for Te 3d. The peaks at 574.7 eV and 584 eV can be attributed to Te $3d_{5/2}$ and Te $3d_{3/2}$, respectively. They correspond to Bi_2Te_3. The peaks at 577.2 eV and 587.6 eV correspond to tellurium oxide, TeO_2 [120]. Table 14 summarises the elemental composition results. It can also be observed that for the composites, the composition of bismuth and tellurium is lower.

The XPS spectra for the GO composites are similar, showing the peaks observed in Figure 35. The Bi 4f scan shows similar peaks like the ones obtained for the pure Bi_2Te_3. However, the tellurium scan differs. In addition to the Bi_2Te_3, Te, and tellurium oxide (TeO_3) peaks, there are also peaks at 572.2 eV and 582.6 eV, corresponding to pure Te.

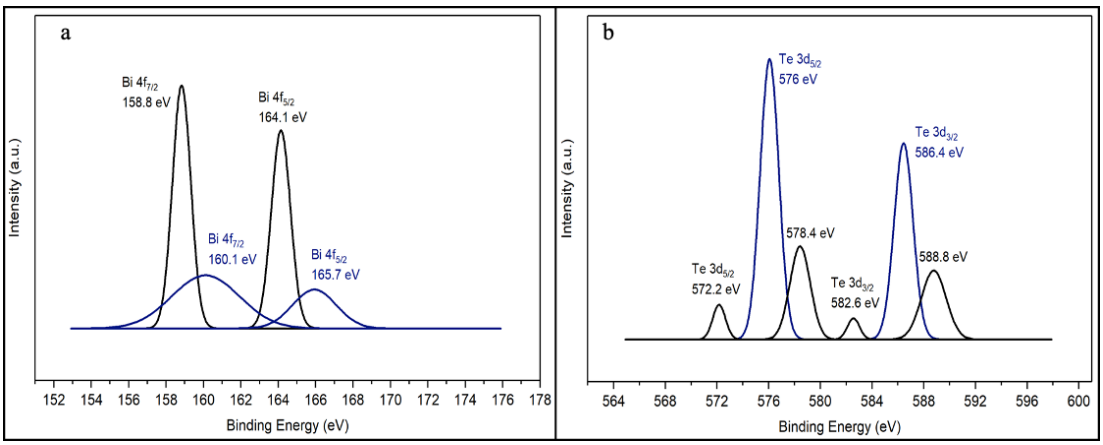

Figure 35: XPS analysis of Bi_2Te_3-0.25% GO (a) Bi 4f scan, (b) Te 3d scan

Table 14: Elemental quantification of Bi_2Te_3 and Bi_2Te_3 composites

Material	Composition (at. %)			
	Bi	**Te**	**C**	**O**
Pure Bi_2Te_3	22.07	15.03	-	62.3
Ag-doped Bi_2Te_3	19.99	18.57	-	61.44
Bi_2Te_3-0.25% GO	10.8	7.53	43.36	38.31
Bi_2Te_3-0.50% GO	11.05	7.54	40.36	41.04

Figure 36 shows the SEM images for all Bi_2Te_3-based samples that were synthesized. The images all show hexagonal plates, along with wood-like structures observed for the GO composites. The pure and doped samples show more plates than the composites. The composites show more irregular structures than the pure samples, also showing needle-like structures.

The needle-like structure observed in the SEM images for the Bi_2Te_3-graphene composites was further studied. The elemental mapping for the structure can be seen in Figure 37 (b) and (c) for the structure in Bi_2Te_3-0.25% GO (seen in Figure 36 (j)). As observed in Figure 37 (b), the structure contained mainly tellurium, with low bismuth, consistent with the elemental mapping of these needles in Bi_2Te_3-0.5% GO as well.

A wood-like structure was observed for all of the samples. The structures were further studied using EDS. Figure 38 (a) shows the SEM image for the structure in Bi_2Te_3 with 0.50% graphene loading. The elemental mapping of Te in Figure 38 (b) indicates that the structures contain high tellurium and confirmed by the EDS chemical analysis, which was 81.64%. The XPS scans for the composites also showed the presence of free Te within

the nanopowders. The composition of oxygen and carbon is homogenous through the surface, as seen in Figure 38 (d) and (e). However, this was not constant across all samples, with other samples showing a more uniform distribution. EDS studies and elemental mapping of the Bi_2Te_3-0.25% GO and pure Bi_2Te_3 samples showed that the composition of this structure also had high amounts of bismuth.

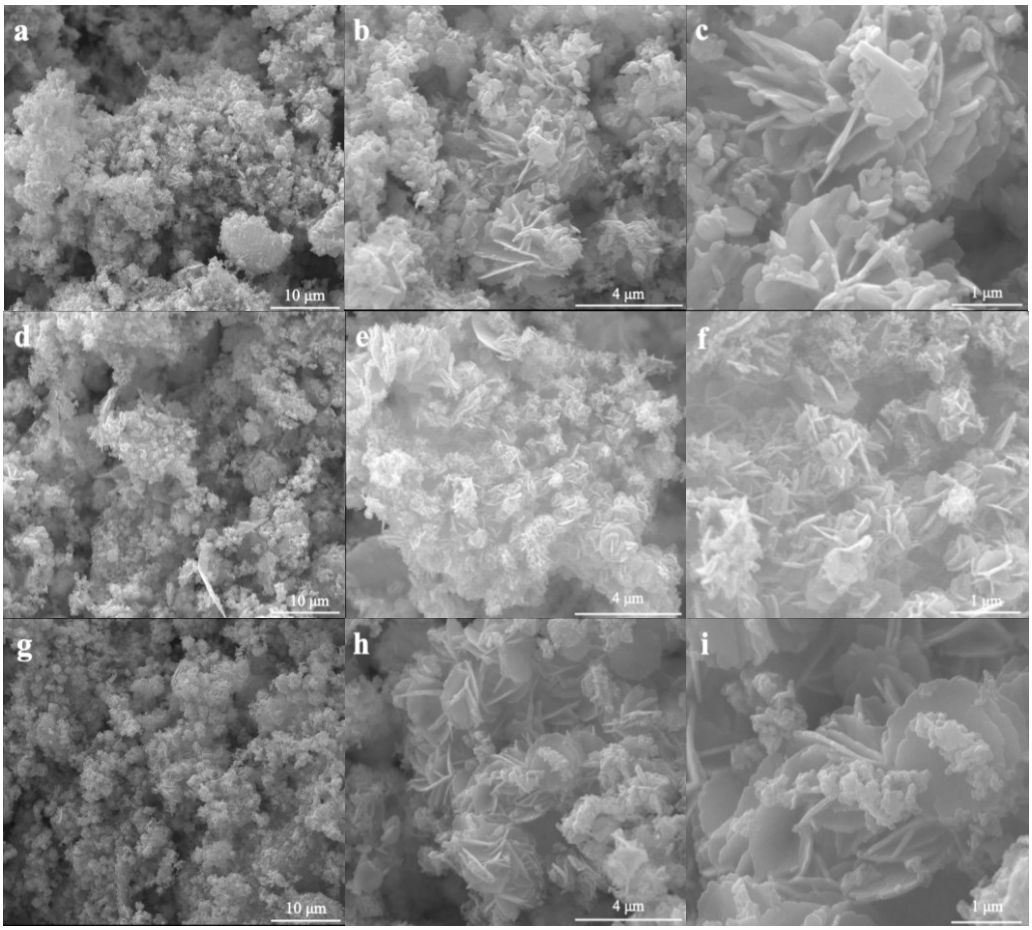

Figure 36: SEM images of (a-c) pure Bi_2Te_3 with CTAB, (d-f) pure Bi_2Te_3 without CTAB, (g-i) Ag-doped Bi_2Te_3, (j-l) Bi_2Te_3-0.25% GO, and (m-o) Bi_2Te_3-0.25% GO

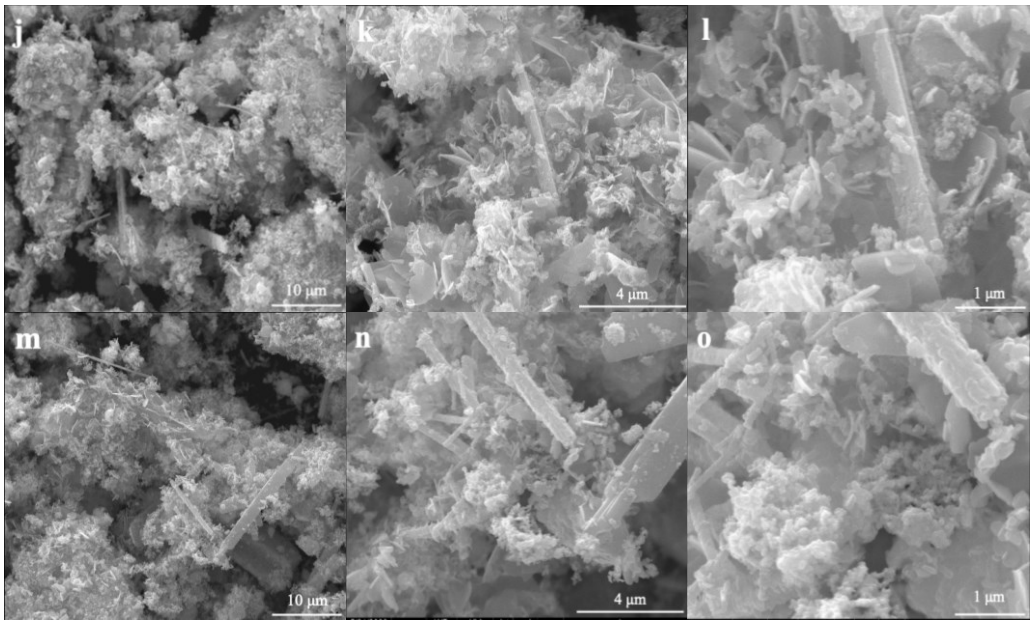

Figure 36 Continued

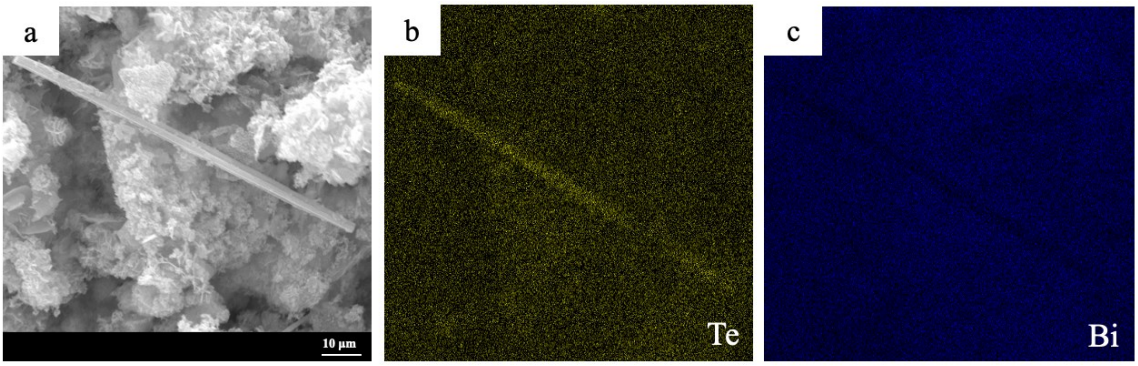

Figure 37: (a) SEM image of the needle-like structure in Bi_2Te_3-0.25% GO and corresponding EDS mapping on the surface for (b) Te, and (c) Bi.

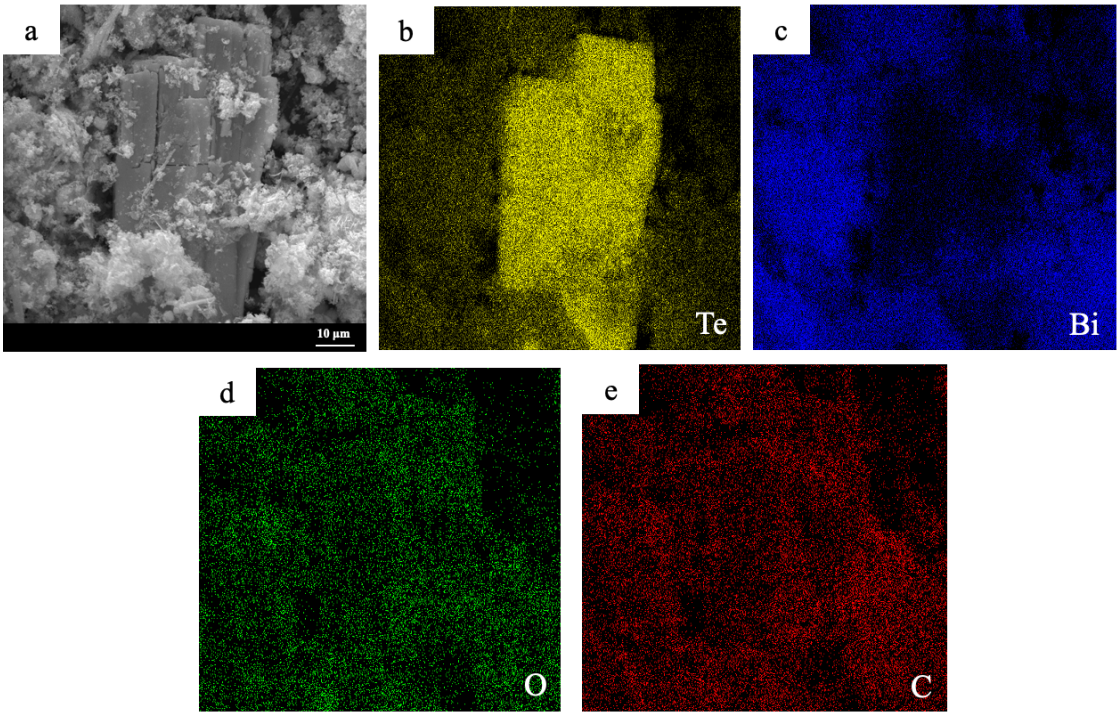

Figure 38: (a) SEM image of the wood-like structure in Bi_2Te_3, and corresponding EDS mapping on the surface for (b) Te, (c) Bi, (d) O, and (e) C

5.2.2 Thermal Properties

As shown in Figure 39, DSC was performed on the various synthesized Bi_2Te_3 nanopowders. An endothermic melting peak is observed for all variants (excluding doped Bi_2Te_3) at an onset temperature of 417.7 ˚C, which can be attributed to a eutectic peak for Bi_2Te_3 and Te as reported in the literature [121]. An exothermic phase transformation is observed at a temperature of around 400 ˚C for the materials that gave an endothermic peak. The curves for pure Bi_2Te_3 show several thermal events. An endothermic peak was observed at an onset temperature of 95 ˚C, which could be due to the evaporation of water. Melting and consequent fusion peaks were also observed at onset temperatures of 265.94

and 269.17 ˚C, respectively. The melting can be attributed to the melting of any free bismuth present within the sample. Peaks at an onset temperature of ~265 ˚C were also observed for the GO composites. Conversely, no significant peaks were observed in the curves for Ag-doped Bi_2Te_3. Multiple cycles should be performed in the DSC to assess the thermal stability of the synthesized materials properly. Table 15 summarises all thermal parameters obtained from the DSC analysis.

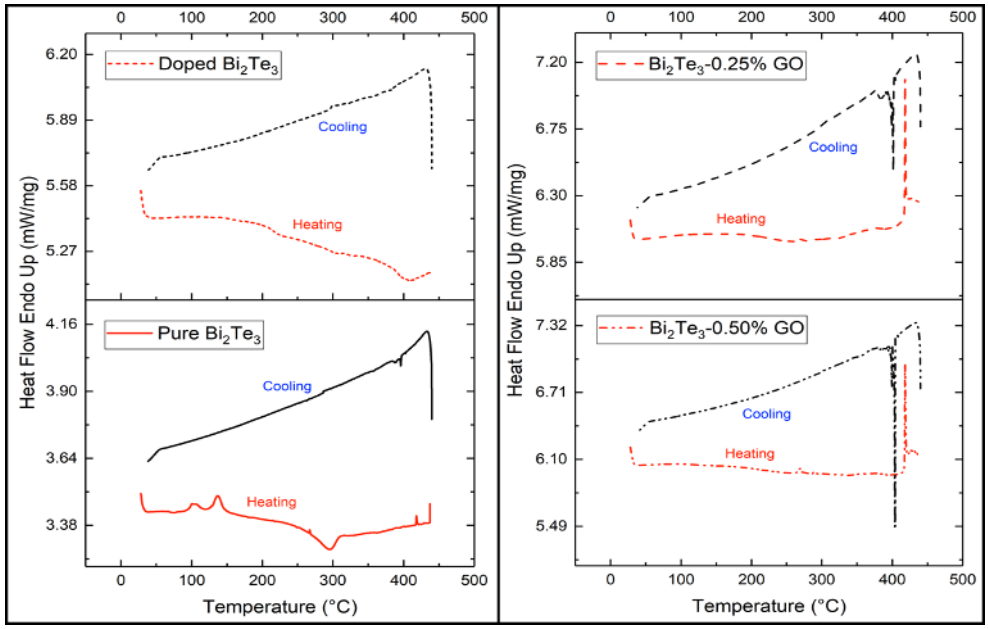

Figure 39: DSC of various Bi_2Te_3 nanopowders, performed from ambient to 450 ˚C under N_2 atmosphere

Table 15: Thermal parameters for Bi_2Te_3-based materials obtained from DSC analysis

Material	Heating		Cooling	
	T_m (°C)	Enthalpy (J/g)	Onset. (°C)	Enthalpy (J/g)
Bi_2Te_3-0.25% GO	265.2	0.58	401.5	-18.9
	417.6	13.02		
Bi_2Te_3-0.50% GO	264.8	1.55	404.2	-23.2
	417.7	15.09		
Pure Bi_2Te_3	95.4	2.19	396.4	-18.9
	127.5	4.83		
	265.94	0.12		
	269.17	-7.98		
	417.3	0.28		

The thermal stability of the Bi_2Te_3 materials was also investigated by conducting TGA. Figure 40 depicts how weight changes with an increase in temperature. An increase in the mass is observed for the three samples, which can be attributed to the reaction of an intermediate product with nitrogen consistent with previously reported [122]. The Ag-doped sample shows a decrease in weight at ~ 100 ˚C, followed by constant weight at 150 ˚C and another increase in weight at 300 ˚C with a spike at 400 ˚C. This behavior was not previously reported.

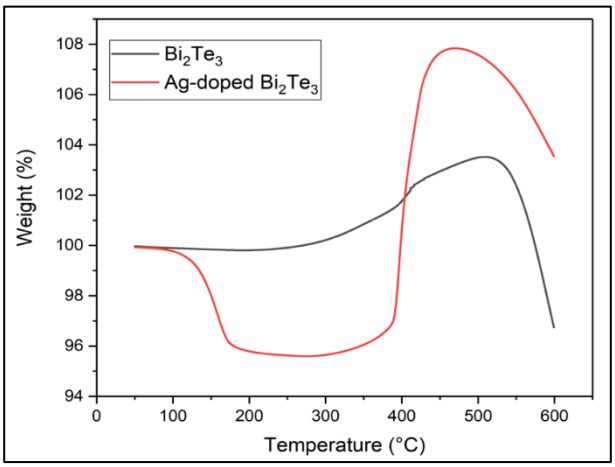

Figure 40: TGA of Bismuth Telluride samples heated at 10 ˚C/min, under N_2 atmosphere

6. CONCLUSION AND FUTURE WORK

In this research, pure tin selenide and bismuth telluride and their composites with GO were synthesized using a scalable solution method. Tin selenide synthesis used tin chloride and selenium dioxide as the precursors, with hydrazine used as the reducing agent. The synthesis of the thermoelectric materials was confirmed by XRD analysis. The presence of pure selenium was also detected in the composites, confirmed by XRD and XPS. Thermal conductivity testing carried out for $SnSe_2$ gave a low value (0.60 W/m.K), favorable for TE applications. The addition of GO reduced the thermal conductivity further, giving a minimum value of 0.41 $Wm^{-1}K^{-1}$ at 0.50% GO loading. The hardness measurements carried out for $SnSe_2$ gave results agreeable with the literature. XPS detected the presence of oxides within the sample. However, the TGA and DSC curves of the materials showed that their thermal stability requires improvement, as a high amount of weight loss was observed in the TGA, along with melting in the DSC analysis.

Bismuth telluride and the composites with graphene oxide were prepared using bismuth chloride and pure tellurium powder, with sodium borohydride used as the reducing agent. An Ag-doped sample of bismuth telluride was also prepared. XRD confirmed the successful synthesis of the material, and XPS for the materials indicated a high amount of oxygen in the materials, with oxides of both bismuth and tellurium present. Ag-doped Bi_2Te_3 was also synthesized. TGA for the bismuth telluride samples showed low to no loss in mass, suggesting good stability. However, the DSC analysis showed melting around 269 ˚C for the samples, suggesting a free bismuth present.

The low thermal conductivity of the tin selenide samples suggest favorable TE properties can be obtained from these materials, and the reduction of the thermal conductivity due to the addition of graphene is also promising. Moreover, graphene also enhanced the mechanical properties, as demonstrated by a 26% increase in hardness. For the bismuth telluride-based materials, the thermal stability of the nanopowders is favorable for applications within the tested temperature range. A reduction in grain size was also observed for both systems upon the addition of graphene.

Despite the promising properties in the preliminary analysis, both the tin selenide and bismuth telluride samples could not be sintered successfully due to melting during the heating process. To correct this, the synthesis must be repeated to ensure no free metals are present so that the TE performance testing can be performed, and the impact of adding graphene to the pure materials can be studied. The effect of premixing, synthesis time, and temperature, and the amount of the reducing agent used must be tuned to ensure no impurities are present. In addition to optimizing the synthesis process, doped graphene nanocomposites should also be produced to analyze any effect that coupling the three methods (nanostructuring, nanocompositing, and doping) could have on the thermal and electrical properties of these materials.

REFERENCES

[1] C. Forman, I. K. Muritala, R. Pardemann, and B. Meyer, "Estimating the global waste heat potential," *Renewable and Sustainable Energy Reviews,* vol. 57, pp. 1568-1579, 2016, doi: 10.1016/j.rser.2015.12.192.

[2] R. Freer and A. V. Powell, "Realising the potential of thermoelectric technology: a Roadmap," *Journal of Materials Chemistry C,* vol. 8, no. 2, pp. 441-463, 2020, doi: 10.1039/c9tc05710b.

[3] J. He and T. M. Tritt, "Advances in thermoelectric materials research: Looking back and moving forward," *Science,* vol. 357, no. 6358, Sep 29 2017, doi: 10.1126/science.aak9997.

[4] X. Zhang and L. D. Zhao, "Thermoelectric materials: Energy conversion between heat and electricity," *Journal of Materiomics,* vol. 1, no. 2, pp. 92-105, 2015, doi: 10.1016/j.jmat.2015.01.001.

[5] A. J. Minnich, M. S. Dresselhaus, Z. F. Ren, and G. Chen, "Bulk nanostructured thermoelectric materials: Current research and future prospects," *Energy and Environmental Science,* vol. 2, no. 5, pp. 466-479, 2009, doi: 10.1039/b822664b.

[6] D. M. Rowe, *Thermoelectrics Handbook: Macro to Nano*. Boca Raton: Taylor & Francis Group, 2006.

[7] P. Brinks and M. Huijben, *Thermoelectric oxides*. Elsevier Ltd, 2015, pp. 397-441.

[8] G. S. Nolan, J. Sharp, and H. J. Goldsmid, *Thermoelectrics: Basic Principles and New Materials Developments*. Berlin: Springer, 2001, pp. 293-293.

[9] R. Saidur, M. Rezaei, W. K. Muzammil, M. H. Hassan, S. Paria, and M. Hasanuzzaman, "Technologies to recover exhaust heat from internal combustion

engines," *Renewable and Sustainable Energy Reviews,* vol. 16, no. 8, pp. 5649-5659, 2012, doi: 10.1016/j.rser.2012.05.018.

[10] M. Zebarjadi *et al.*, "Power Factor Enhancement by Modulation Doping in Bulk Nanocomposites," *Nano Letters,* vol. 11, no. 6, pp. 2225-2230, 2011, doi: 10.1021/nl201206d.

[11] A. V. da Rosa and A. V. da Rosa, *Chapter 5 – Thermoelectricity*. 2009, pp. 153-218.

[12] J. P. Heremans, B. Wiendlocha, and A. M. Chamoire, "Resonant levels in bulk thermoelectric semiconductors," *Energy Environ. Sci.,* vol. 5, no. 2, pp. 5510-5530, 2012, doi: 10.1039/c1ee02612g.

[13] C. Wan, Y. Wang, N. Wang, W. Norimatsu, M. Kusunoki, and K. Koumoto, "Development of novel thermoelectric materials by reduction of lattice thermal conductivity," *Sci Technol Adv Mater,* vol. 11, no. 4, p. 044306, Aug 2010, doi: 10.1088/1468-6996/11/4/044306.

[14] X. Zhou *et al.*, "Routes for high-performance thermoelectric materials," *Materials Today,* vol. 21, no. 9, pp. 974-988, 2018, doi: 10.1016/j.mattod.2018.03.039.

[15] S. Hooshmand Zaferani, R. Ghomashchi, and D. Vashaee, "Strategies for engineering phonon transport in Heusler thermoelectric compounds," *Renewable and Sustainable Energy Reviews,* vol. 112, pp. 158-169, 2019, doi: 10.1016/j.rser.2019.05.051.

[16] G. Tan, L. D. Zhao, and M. G. Kanatzidis, "Rationally Designing High-Performance Bulk Thermoelectric Materials," *Chem Rev,* vol. 116, no. 19, pp. 12123-12149, Oct 12 2016, doi: 10.1021/acs.chemrev.6b00255.

[17] D. Beretta *et al.*, "Thermoelectrics: From history, a window to the future," *Materials Science and Engineering R: Reports,* vol. 138, no. July, 2019, doi: 10.1016/j.mser.2018.09.001.

[18] J. Munro, *The Story of Electricity* (Start Classics). Start Classics, 2014.

[19] P. Pichanusakorn and P. Bandaru, "Nanostructured thermoelectrics," *Materials Science and Engineering R: Reports,* vol. 67, no. 2-4, pp. 19-63, 2010, doi: 10.1016/j.mser.2009.10.001.

[20] S. M. Pourkiaei *et al.*, "Thermoelectric cooler and thermoelectric generator devices: A review of present and potential applications, modeling and materials," *Energy,* vol. 186, pp. 115849-115849, 2019, doi: 10.1016/j.energy.2019.07.179.

[21] Y. Sun, C. A. Di, W. Xu, and D. Zhu, "Advances in n-Type Organic Thermoelectric Materials and Devices," *Advanced Electronic Materials,* vol. 5, no. 11, pp. 1-27, 2019, doi: 10.1002/aelm.201800825.

[22] H. M. Elmoughni, A. K. Menon, R. M. W. Wolfe, and S. K. Yee, "A Textile-Integrated Polymer Thermoelectric Generator for Body Heat Harvesting," *Advanced Materials Technologies,* vol. 4, no. 7, pp. 1-6, 2019, doi: 10.1002/admt.201800708.

[23] J. P. Heremans, M. S. Dresselhaus, L. E. Bell, and D. T. Morelli, "When thermoelectrics reached the nanoscale," *Nature Nanotechnology,* vol. 8, no. 7, pp. 471-473, 2013, doi: 10.1038/nnano.2013.129.

[24] Y. Pei, H. Wang, and G. J. Snyder, "Band engineering of thermoelectric materials," *Advanced Materials,* vol. 24, no. 46, pp. 6125-6135, 2012, doi: 10.1002/adma.201202919.

[25] J. P. Heremans *et al.*, "Enhancement of Thermoelectric Efficiency in PbTe by Distortion of the Electronic Density of States," *Science,* vol. 321, no. 5888, pp. 554 LP-557, 2008, doi: 10.1126/science.1159725.

[26] L. D. Hicks and M. S. Dresselhaus, "Effect of quantum-well structures on the thermoelectric figure of merit," *Physical Review B,* vol. 47, no. 19, pp. 12727-12731, 1993, doi: 10.1103/PhysRevB.47.12727.

[27] L. D. Hicks and M. S. Dresselhaus, "Thermoelectric figure of merit of a one-dimensional conductor," *Physical Review B,* vol. 47, no. 24, pp. 16631-16634, 1993, doi: 10.1103/PhysRevB.47.16631.

[28] M. S. Dresselhaus *et al.*, "New directions for low-dimensional thermoelectric materials," *Advanced Materials,* vol. 19, no. 8, pp. 1043-1053, 2007, doi: 10.1002/adma.200600527.

[29] K. Biswas *et al.*, "High-performance bulk thermoelectrics with all-scale hierarchical architectures," *Nature,* vol. 489, no. 7416, pp. 414-418, 2012, doi: 10.1038/nature11439.

[30] J. R. Szczech, J. M. Higgins, and S. Jin, "Enhancement of the thermoelectric properties in nanoscale and nanostructured materials," *Journal of Materials Chemistry,* vol. 21, no. 12, pp. 4037-4055, 2011, doi: 10.1039/c0jm02755c.

[31] X. Chen, Z. Zhou, Y. H. Lin, and C. Nan, "Thermoelectric thin films: Promising strategies and related mechanism on boosting energy conversion performance," *Journal of Materiomics,* vol. 6, no. 3, pp. 494-512, 2020, doi: 10.1016/j.jmat.2020.02.008.

[32] G. J. Snyder and E. S. Toberer, "Complex thermoelectric materials," *Materials for Sustainable Energy: A Collection of Peer-Reviewed Research and Review Articles*

from Nature Publishing Group, vol. 7, no. February, pp. 101-110, 2010, doi: 10.1142/9789814317665_0016.

[33] X. Sun *et al.*, "Experimental study of the effect of the quantum well structures on the thermoelectric figure of merit in Si/Si1-xGex system," *International Conference on Thermoelectrics, ICT, Proceedings,* vol. 53, no. 16, pp. 652-655, 1999, doi: 10.1557/proc-545-369.

[34] G. Tan *et al.*, "High Thermoelectric Performance SnTe-In2Te3 Solid Solutions Enabled by Resonant Levels and Strong Vacancy Phonon Scattering," *Chemistry of Materials,* vol. 27, no. 22, pp. 7801-7811, 2015, doi: 10.1021/acs.chemmater.5b03708.

[35] L. Yang, Z. G. Chen, G. Han, M. Hong, Y. Zou, and J. Zou, "High-performance thermoelectric Cu2Se nanoplates through nanostructure engineering," *Nano Energy,* vol. 16, pp. 367-374, 2015, doi: 10.1016/j.nanoen.2015.07.012.

[36] S. K. Bux, J. P. Fleurial, and R. B. Kaner, "Nanostructured materials for thermoelectric applications," *Chemical Communications,* vol. 46, no. 44, pp. 8311-8324, 2010, doi: 10.1039/c0cc02627a.

[37] M. G. Kanatzidis, "Nanostructured thermoelectrics: The new paradigm?," *Chemistry of Materials,* vol. 22, no. 3, pp. 648-659, 2010, doi: 10.1021/cm902195j.

[38] B. Poudel *et al.*, "High-thermoelectric performance of nanostructured bismuth antimony telluride bulk alloys," *Science,* vol. 320, no. 5876, pp. 634-638, 2008, doi: 10.1126/science.1156446.

[39] G. Joshi *et al.*, "Enhanced thermoelectric figure-of-merit in nanostructured p-type silicon germanium bulk alloys," *Nano Letters,* vol. 8, no. 12, pp. 4670-4674, 2008, doi: 10.1021/nl8026795.

[40] G. S. Nolas, J. L. Cohn, and G. A. Slack, "Effect of partial void filling on the lattice thermal conductivity of skutterudites," *Physical Review B,* vol. 58, no. 1, 1998.

[41] Y. Pei *et al.*, "Stabilizing the optimal carrier concentration for high thermoelectric efficiency," *Advanced Materials,* vol. 23, no. 47, pp. 5674-5678, 2011, doi: 10.1002/adma.201103153.

[42] L. Yang, Z. G. Chen, M. S. Dargusch, and J. Zou, "High Performance Thermoelectric Materials: Progress and Their Applications," *Advanced Energy Materials,* vol. 8, no. 6, pp. 1-28, 2018, doi: 10.1002/aenm.201701797.

[43] X. Li *et al.*, "Synergistic band convergence and endotaxial nanostructuring: Achieving ultralow lattice thermal conductivity and high figure of merit in eco-friendly SnTe," *Nano Energy,* vol. 67, no. November 2019, 2020, doi: 10.1016/j.nanoen.2019.104261.

[44] X. B. Zhao, X. H. Ji, Y. H. Zhang, T. J. Zhu, J. P. Tu, and X. B. Zhang, "Bismuth telluride nanotubes and the effects on the thermoelectric properties of nanotube-containing nanocomposites," *Applied Physics Letters,* vol. 86, no. 6, pp. 1-3, 2005, doi: 10.1063/1.1863440.

[45] H. Sevinçli, C. Sevik, T. Çağın, and G. Cuniberti, "A bottom-up route to enhance thermoelectric figures of merit in graphene nanoribbons," *Scientific Reports,* vol. 3, no. 1, pp. 1228-1228, 2013, doi: 10.1038/srep01228.

[46] H. Mamur, M. R. A. Bhuiyan, F. Korkmaz, and M. Nil, "A review on bismuth telluride (Bi 2 Te 3) nanostructure for thermoelectric applications," *Renewable and Sustainable Energy Reviews,* vol. 82, no. November 2017, pp. 4159-4169, 2018, doi: 10.1016/j.rser.2017.10.112.

[47] K. F. Samat, N. H. Trung, and T. Ono, "Enhancement in thermoelectric performance of electrochemically deposited platinum-bismuth telluride

nanocomposite," *Electrochimica Acta,* vol. 312, pp. 62-71, 2019, doi: 10.1016/j.electacta.2019.04.139.

[48] J. An, M. K. Han, and S. J. Kim, "Synthesis of heavily Cu-doped Bi2Te3 nanoparticles and their thermoelectric properties," *Journal of Solid State Chemistry,* vol. 270, no. November 2018, pp. 407-412, 2019, doi: 10.1016/j.jssc.2018.11.024.

[49] A. K. Bohra *et al.*, "Transition from n- to p-type conduction concomitant with enhancement of figure-of-merit in Pb doped bismuth telluride: Material to device development," *Materials and Design,* vol. 159, pp. 127-137, 2018, doi: 10.1016/j.matdes.2018.08.035.

[50] J. Yang, F. Wu, Z. Zhu, L. Yao, H. Song, and X. Hu, "Thermoelectrical properties of lutetium-doped Bi2Te3bulk samples prepared from flower-like nanopowders," *Journal of Alloys and Compounds,* vol. 619, pp. 401-405, 2015, doi: 10.1016/j.jallcom.2014.09.024.

[51] B. Trawiński, B. Bochentyn, N. Gostkowska, M. Łapiński, T. Miruszewski, and B. Kusz, "Structure and thermoelectric properties of bismuth telluride—Carbon composites," *Materials Research Bulletin,* vol. 99, no. May 2017, pp. 10-17, 2018, doi: 10.1016/j.materresbull.2017.10.043.

[52] J. M. Lin *et al.*, "Annealing effects on the thermoelectric properties of silver-doped bismuth telluride thin films," *Microelectronic Engineering,* vol. 148, pp. 51-54, 2015, doi: 10.1016/j.mee.2015.08.008.

[53] Y. Wu, R. Zhai, T. Zhu, and X. Zhao, "Enhancing room temperature thermoelectric performance of n-type polycrystalline bismuth-telluride-based alloys via Ag doping and hot deformation," *Materials Today Physics,* vol. 2, pp. 62-68, 2017, doi: 10.1016/j.mtphys.2017.09.001.

[54] J. B. Vaney, S. Aminorroaya Yamini, H. Takaki, K. Kobayashi, N. Kobayashi, and T. Mori, "Magnetism-mediated thermoelectric performance of the Cr-doped bismuth telluride tetradymite," *Materials Today Physics,* vol. 9, pp. 100090-100090, 2019, doi: 10.1016/j.mtphys.2019.03.004.

[55] Q. Lognoné and F. Gascoin, "Reactivity, stability and thermoelectric properties of n-Bi 2Te3 doped with different copper amounts," *Journal of Alloys and Compounds,* vol. 610, pp. 1-5, 2014, doi: 10.1016/j.jallcom.2014.04.166.

[56] K. T. Kim, H. Y. Koo, G. G. Lee, and G. H. Ha, "Synthesis of alumina nanoparticle-embedded-bismuth telluride matrix thermoelectric composite powders," *Materials Letters,* vol. 82, no. X, pp. 141-144, 2012, doi: 10.1016/j.matlet.2012.05.053.

[57] H. Pang, Y. Y. Piao, Y. Q. Tan, G. Y. Jiang, J. H. Wang, and Z. M. Li, "Thermoelectric behaviour of segregated conductive polymer composites with hybrid fillers of carbon nanotube and bismuth telluride," *Materials Letters,* vol. 107, pp. 150-153, 2013, doi: 10.1016/j.matlet.2013.06.008.

[58] Y. Zhou, L. Li, Q. Tan, and J. F. Li, "Thermoelectric properties of Pb-doped bismuth telluride thin films deposited by magnetron sputtering," *Journal of Alloys and Compounds,* vol. 590, pp. 362-367, 2014, doi: 10.1016/j.jallcom.2013.12.136.

[59] S. Li *et al.*, "Graphene quantum dots embedded in Bi2Te3 nanosheets to enhance thermoelectric performance," *ACS Applied Materials and Interfaces,* vol. 9, no. 4, pp. 3677-3685, 2017, doi: 10.1021/acsami.6b14274.

[60] H. j. Wu, B. Y. Chen, and H. Y. Cheng, "The p-n conduction type transition in Ge-incorporated Bi2Te3 thermoelectric materials," *Acta Materialia,* vol. 122, pp. 120-129, 2017, doi: 10.1016/j.actamat.2016.09.043.

[61] H. J. Wu and W. T. Yen, "High thermoelectric performance in Cu-doped Bi2Te3 with carrier-type transition," *Acta Materialia,* vol. 157, pp. 33-41, 2018, doi: 10.1016/j.actamat.2018.07.022.

[62] F. Wu, H. Song, J. Jia, and X. Hu, "Effects of Ce, Y, and Sm doping on the thermoelectric properties of Bi2Te3 alloy," *Progress in Natural Science: Materials International,* vol. 23, no. 4, pp. 408-412, 2013, doi: 10.1016/j.pnsc.2013.06.007.

[63] F. Wu, W. Wang, X. Hu, and M. Tang, "Thermoelectric properties of I-doped n-type Bi2Te3-based material prepared by hydrothermal and subsequent hot pressing," *Progress in Natural Science: Materials International,* vol. 27, no. 2, pp. 203-207, 2017, doi: 10.1016/j.pnsc.2017.02.009.

[64] L. Hu, T. Zhu, X. Liu, and X. Zhao, "Point defect engineering of high-performance bismuth-telluride-based thermoelectric materials," vol. 24, ed, 2014, pp. 5211-5218.

[65] D. Li *et al.*, "Thermoelectric properties of hydrothermally synthesized Bi 2Te 3-xSe x nanocrystals," *Scripta Materialia,* vol. 67, no. 2, pp. 161-164, 2012, doi: 10.1016/j.scriptamat.2012.04.005.

[66] Y. H. Zhang, T. J. Zhu, J. P. Tu, and X. B. Zhao, "Flower-like nanostructure and thermoelectric properties of hydrothermally synthesized La-containing Bi2Te3 based alloys," *Materials Chemistry and Physics,* vol. 103, no. 2-3, pp. 484-488, 2007, doi: 10.1016/j.matchemphys.2007.02.059.

[67] K. Ahmad, C. Wan, M. A. Al-Eshaikh, and A. N. Kadachi, "Enhanced thermoelectric performance of Bi 2 Te 3 based graphene nanocomposites," *Applied Surface Science,* vol. 474, no. October, pp. 2-8, 2019, doi: 10.1016/j.apsusc.2018.10.163.

[68] S. Kumar, S. Singh, P. K. Dhawan, R. R. Yadav, and N. Khare, "Effect of graphene nanofillers on the enhanced thermoelectric properties of Bi2Te3 nanosheets: Elucidating the role of interface in de-coupling the electrical and thermal characteristics," *Nanotechnology,* vol. 29, no. 13, 2018, doi: 10.1088/1361-6528/aaa99e.

[69] S. Kumar, D. Chaudhary, P. Kumar Dhawan, R. R. Yadav, and N. Khare, "Bi2Te3-MWCNT nanocomposite: An efficient thermoelectric material," *Ceramics International,* vol. 43, no. 17, pp. 14976-14982, 2017, doi: 10.1016/j.ceramint.2017.08.017.

[70] Y. Zhang, Q. Zhou, J. Zhu, Q. Yan, S. X. Dou, and W. Sun, "Nanostructured Metal Chalcogenides for Energy Storage and Electrocatalysis," *Advanced Functional Materials,* vol. 27, no. 35, pp. 1702317-1702317, 2017, doi: 10.1002/adfm.201702317.

[71] F. K. Butt *et al.*, "Synthesis of mid-infrared SnSe nanowires and their optoelectronic properties," *CrystEngComm,* vol. 16, no. 17, pp. 3470-3473, 2014, doi: 10.1039/c4ce00267a.

[72] L.-D. Zhao *et al.*, "Ultralow thermal conductivity and high thermoelectric figure of merit in SnSe crystals," *Nature,* vol. 508, pp. 373-373, 2014. [Online]. Available: https://doi.org/10.1038/nature13184 http://10.0.4.14/nature13184.

[73] J. D. Wasscher, W. Albers, and C. Haas, "Simple evaluation of the maximum thermoelectric figure of merit, with application to mixed crystals SnS1-xSex," *Solid State Electronics,* vol. 6, no. 3, pp. 261-264, 1963, doi: 10.1016/0038-1101(63)90083-2.

[74] W. J. Baumgardner, J. J. Choi, Y.-F. Lim, and T. Hanrath, "SnSe Nanocrystals: Synthesis, Structure, Optical Properties, and Surface Chemistry," *Journal of the*

American Chemical Society, vol. 132, no. 28, pp. 9519-9521, 2010, doi: 10.1021/ja1013745.

[75] J. J. Meléndez and R. L. González-Romero, "zT factors in Ag- and Na-doped SnSe: Chemical potentials, relaxation times and predictions for other dopant species," *Journal of Alloys and Compounds,* vol. 757, pp. 70-78, 2018, doi: 10.1016/j.jallcom.2018.05.042.

[76] K. Peng *et al.*, "Broad temperature plateau for high ZTs in heavily doped p-type SnSe single crystals," *Energy and Environmental Science,* vol. 9, no. 2, pp. 454-460, 2016, doi: 10.1039/c5ee03366g.

[77] M. Gharsallah *et al.*, "Giant Seebeck effect in Ge-doped SnSe," *Scientific Reports,* vol. 6, no. May, pp. 1-9, 2016, doi: 10.1038/srep26774.

[78] J. Sun *et al.*, "Interface tuning charge transport and enhanced thermoelectric properties in flower-like SnSe2 hierarchical nanostructures," *Applied Surface Science,* vol. 510, no. January, pp. 145478-145478, 2020, doi: 10.1016/j.apsusc.2020.145478.

[79] X. He and H. Shen, "Ab initio calculations of band structure and thermophysical properties for SnS 2 and SnSe 2," *Physica B: Condensed Matter,* vol. 407, no. 7, pp. 1146-1152, 2012, doi: 10.1016/j.physb.2012.01.102.

[80] E. P. Mukhokosi, S. B. Krupanidhi, and K. K. Nanda, "Band Gap Engineering of Hexagonal SnSe2 Nanostructured Thin Films for Infra-Red Photodetection," *Sci Rep,* vol. 7, no. 1, p. 15215, Nov 9 2017, doi: 10.1038/s41598-017-15519-x.

[81] B. Z. Sun, Z. Ma, C. He, and K. Wu, "Anisotropic thermoelectric properties of layered compounds in SnX2 (X = S, Se): A promising thermoelectric material," *Physical Chemistry Chemical Physics,* vol. 17, no. 44, pp. 29844-29853, 2015, doi: 10.1039/c5cp03700j.

[82] Y. Ding, B. Xiao, G. Tang, and J. Hong, "Transport properties and high thermopower of SnSe2: A full ab-initio investigation," *Journal of Physical Chemistry C,* vol. 121, no. 1, pp. 225-236, 2017, doi: 10.1021/acs.jpcc.6b11467.

[83] S. Saha, A. Banik, and K. Biswas, "Few-Layer Nanosheets of n-Type SnSe2," *Chemistry - A European Journal,* vol. 22, no. 44, pp. 15634-15638, 2016, doi: 10.1002/chem.201604161.

[84] Y. Luo *et al.*, "n-Type SnSe2 Oriented-Nanoplate-Based Pellets for High Thermoelectric Performance," *Advanced Energy Materials,* vol. 8, no. 8, pp. 2-7, 2018, doi: 10.1002/aenm.201702167.

[85] C. Liu *et al.*, "Dynamic Ag+-intercalation with AgSnSe2 nano-precipitates in Cl-doped polycrystalline SnSe2 toward ultra-high thermoelectric performance," *Journal of Materials Chemistry A,* vol. 7, no. 16, pp. 9761-9772, 2019, doi: 10.1039/c9ta01678c.

[86] S. Wu *et al.*, "Realizing tremendous electrical transport properties of polycrystalline SnSe2 by Cl-doped and anisotropy," *Ceramics International,* vol. 45, no. 1, pp. 82-89, 2019, doi: 10.1016/j.ceramint.2018.09.136.

[87] Y. Shu *et al.*, "Modification of Bulk Heterojunction and Cl Doping for High-Performance Thermoelectric SnSe2/SnSe Nanocomposites," *ACS Applied Materials and Interfaces,* vol. 10, no. 18, pp. 15793-15802, 2018, doi: 10.1021/acsami.8b00524.

[88] F. Li *et al.*, "Ag-doped SnSe2 as a promising mid-temperature thermoelectric material," *Journal of Materials Science,* vol. 52, no. 17, pp. 10506-10516, 2017, doi: 10.1007/s10853-017-1238-8.

[89] S. Wu *et al.*, "Enhancement of Thermoelectric Performance of Layered SnSe2 by Synergistic Modulation of Carrier Concentration and Suppression of Lattice

Thermal Conductivity," *ACS Applied Energy Materials,* vol. 2, no. 12, pp. 8481-8490, 2019, doi: 10.1021/acsaem.9b01399.

[90] Y. Wu *et al.*, "Promising thermoelectric performance in van der Waals layered SnSe2," *Materials Today Physics,* vol. 3, pp. 127-136, 2017, doi: https://doi.org/10.1016/j.mtphys.2017.10.001.

[91] P. Xu *et al.*, "Anisotropic thermoelectric properties of layered compound SnSe2," *Science Bulletin,* vol. 62, no. 24, pp. 1663-1668, 2017, doi: 10.1016/j.scib.2017.11.015.

[92] K. Kakaei, M. D. Esrafili, and A. Ehsani, *Graphene-Based Metal Particles*. 2019, pp. 153-202.

[93] C. H. A. Tsang, H. Huang, J. Xuan, H. Wang, and D. Y. C. Leung, "Graphene materials in green energy applications: Recent development and future perspective," *Renewable and Sustainable Energy Reviews,* vol. 120, no. November 2019, pp. 109656-109656, 2020, doi: 10.1016/j.rser.2019.109656.

[94] F. Domínguez-Adame, M. Martín-González, D. Sánchez, and A. Cantarero, "Nanowires: A route to efficient thermoelectric devices," *Physica E: Low-Dimensional Systems and Nanostructures,* vol. 113, no. December 2018, pp. 213-225, 2019, doi: 10.1016/j.physe.2019.03.021.

[95] Y. Du, S. Z. Shen, W. Yang, R. Donelson, K. Cai, and P. S. Casey, "Simultaneous increase in conductivity and Seebeck coefficient in a polyaniline/graphene nanosheets thermoelectric nanocomposite," *Synthetic Metals,* vol. 161, no. 23-24, pp. 2688-2692, 2012, doi: 10.1016/j.synthmet.2011.09.044.

[96] S. Yang, J. Si, Q. Su, and H. Wu, "Enhanced thermoelectric performance of SnSe doped with layered MoS2/graphene," *Materials Letters,* vol. 193, pp. 146-149, 2017, doi: 10.1016/j.matlet.2017.01.079.

[97] B. Liang, Z. Song, M. Wang, L. Wang, and W. Jiang, "Fabrication and thermoelectric properties of graphene/Bi2Te 3 composite materials," *Journal of Nanomaterials,* vol. 2013, 2013, doi: 10.1155/2013/210767.

[98] H. Ju and J. Kim, "Preparation and structure dependent thermoelectric properties of nanostructured bulk bismuth telluride with graphene," *Journal of Alloys and Compounds,* vol. 664, pp. 639-647, 2016, doi: 10.1016/j.jallcom.2016.01.002.

[99] B. Feng, J. Xie, G. Cao, T. Zhu, and X. Zhao, "Enhanced thermoelectric properties of p-type CoSb3/graphene nanocomposite," *Journal of Materials Chemistry A,* vol. 1, no. 42, pp. 13111-13119, 2013, doi: 10.1039/c3ta13202a.

[100] Y. Lin *et al.*, "Thermoelectric Power Generation from Lanthanum Strontium Titanium Oxide at Room Temperature through the Addition of Graphene," *ACS Applied Materials and Interfaces,* vol. 7, no. 29, pp. 15898-15908, 2015, doi: 10.1021/acsami.5b03522.

[101] H. Tang *et al.*, "Graphene network in copper sulfide leading to enhanced thermoelectric properties and thermal stability," *Nano Energy,* vol. 49, no. March, pp. 267-273, 2018, doi: 10.1016/j.nanoen.2018.04.058.

[102] K. Liu, H. Liu, J. Wang, and L. Feng, "Synthesis and characterization of SnSe2 hexagonal nanoflakes," *Materials Letters,* vol. 63, no. 5, pp. 512-514, 2009, doi: 10.1016/j.matlet.2008.10.054.

[103] Y. Xu, Z. Ren, G. Cao, W. Ren, K. Deng, and Y. Zhong, "Fabrication and characterization of Bi2Te3 nanoplates via a simple solvothermal process," *Physica B: Condensed Matter,* vol. 404, no. 21, pp. 4029-4033, 2009, doi: 10.1016/j.physb.2009.07.153.

[104] R. Kohli, *Methods for Monitoring and Measuring Cleanliness of Surfaces*. Elsevier, 2012, pp. 107-178.

[105] D. Nath, F. Singh, and R. Das, "X-ray diffraction analysis by Williamson-Hall, Halder-Wagner and size-strain plot methods of CdSe nanoparticles- a comparative study," *Materials Chemistry and Physics,* vol. 239, no. July 2019, pp. 122021-122021, 2020, doi: 10.1016/j.matchemphys.2019.122021.

[106] Y. Shahmoradi and D. Souri, "Growth of silver nanoparticles within the tellurovanadate amorphous matrix: Optical band gap and band tailing properties, beside the Williamson-Hall estimation of crystallite size and lattice strain," *Ceramics International,* vol. 45, no. 6, pp. 7857-7864, 2019, doi: 10.1016/j.ceramint.2019.01.094.

[107] A. Monshi, M. R. Foroughi, and M. R. Monshi, "Modified Scherrer Equation to Estimate More Accurately Nano-Crystallite Size Using XRD," *World Journal of Nano Science and Engineering,* vol. 02, no. 03, pp. 154-160, 2012, doi: 10.4236/wjnse.2012.23020.

[108] S. Mahadevan, S. P. Behera, G. Gnanaprakash, T. Jayakumar, J. Philip, and B. P. C. Rao, "Size distribution of magnetic iron oxide nanoparticles using Warren-Averbach XRD analysis," *Journal of Physics and Chemistry of Solids,* vol. 73, no. 7, pp. 867-872, 2012, doi: 10.1016/j.jpcs.2012.02.017.

[109] S. Ebnesajjad, "Surface and Material Characterization Techniques," in *Surface Treatment of Materials for Adhesive Bonding*, 2014, pp. 39-75.

[110] R. B. Prime, H. E. Bair, S. Vyazovkin, P. K. Gallagher, and A. Riga, "Thermogravimetric Analysis (TGA)," in *Thermal Analysis of Polymers*, J. D. Menczel and R. B. Prime Eds. New Jersey: Wiley, 2009, p. 241.

[111] J. D. Menczel, L. Judovits, R. B. Prime, H. E. Bair, M. Reading, and S. Swier, "Differential Scanning Calorimetry (DSC)," in *Thermal Analysis of Polymers*, J. D. Menczel and R. B. Prime Eds. New Jersey: Wiley, 2009, ch. 7-9.

[112] V. Tebaldo and G. Gautier, "Influences of evaluation methods and testing load on microhardness and Young's modulus of ZTA and ATZ ceramics," *Ceramics International,* vol. 39, no. 3, pp. 2683-2693, 2013, doi: 10.1016/j.ceramint.2012.09.035.

[113] R. E. Smallman and A. H. W. Ngan, "Chapter 5 - Characterization and Analysis," in *Modern Physical Metallurgy (Eighth Edition)*, R. E. Smallman and A. H. W. Ngan Eds. Oxford: Butterworth-Heinemann, 2014, pp. 159-250.

[114] H. Chen *et al.*, "Hydrothermal synthesis of Cu-doped SnSe2 nanostructure for efficient lithium storage," *Journal of Electroanalytical Chemistry,* vol. 847, no. June, pp. 113205-113205, 2019, doi: 10.1016/j.jelechem.2019.113205.

[115] H. E. Garrafa-Galvez, O. Nava, C. A. Soto-Robles, A. R. Vilchis-Nestor, A. Castro-Beltrán, and P. A. Luque, "Green synthesis of SnO2 nanoparticle using Lycopersicon esculentum peel extract," *Journal of Molecular Structure,* vol. 1197, no. August, pp. 354-360, 2019, doi: 10.1016/j.molstruc.2019.07.052.

[116] H. Lim and S. B. Rawal, "Integrated Bi 2 O 3 nanostructure modified with Au nanoparticles for enhanced photocatalytic activity under visible light irradiation," *Progress in Natural Science: Materials International,* vol. 27, no. 3, pp. 289-296, 2017, doi: 10.1016/j.pnsc.2017.04.003.

[117] M. Popescu *et al.*, "Structure, properties and gas sensing effect of SnSe2 films prepared by pulsed laser deposition method," *Journal of Non-Crystalline Solids,* vol. 353, no. 18-21, pp. 1865-1869, 2007, doi: 10.1016/j.jnoncrysol.2007.02.055.

[118] R. He, J. Zhou, H. Fu, S. Zhang, and C. Jiang, "Room-temperature in situ fabrication of Bi 2 O 3 /g-C 3 N 4 direct Z-scheme photocatalyst with enhanced photocatalytic activity," *Applied Surface Science,* vol. 430, no. April 2019, pp. 273-282, 2018, doi: 10.1016/j.apsusc.2017.07.191.

[119] Y. Yang, L. Xu, C. Su, J. Che, W. Sun, and H. Gao, "Electrospun ZnO/Bi2O3 nanofibers with enhanced photocatalytic activity," *Journal of Nanomaterials,* vol. 2014, no. July, 2014, doi: 10.1155/2014/130539.

[120] Y. M. Cho, K. T. Kim, G. S. Lee, and S. H. Kim, "The role of edge-oxidized graphene to improve the thermopower of p-type bismuth telluride-based thick films," *Applied Surface Science,* vol. 476, pp. 533-538, 2019, doi: 10.1016/j.apsusc.2019.01.026.

[121] G. Zheng *et al.*, "High thermoelectric performance of mechanically robust n-type Bi2Te3−xSex prepared by combustion synthesis," *Journal of Materials Chemistry A,* vol. 3, no. 12, pp. 6603-6613, 2015, doi: 10.1039/c5ta00470e.

[122] E. Požega *et al.*, "Identification and characterization of single crystal Bi2Te3-xSex alloy," *Transactions of Nonferrous Metals Society of China (English Edition),* vol. 25, no. 10, pp. 3279-3285, 2015, doi: 10.1016/S1003-6326(15)63964-4.

APPENDIX A

Appendix A.1

This section provides additional details for the tin selenide analyses.

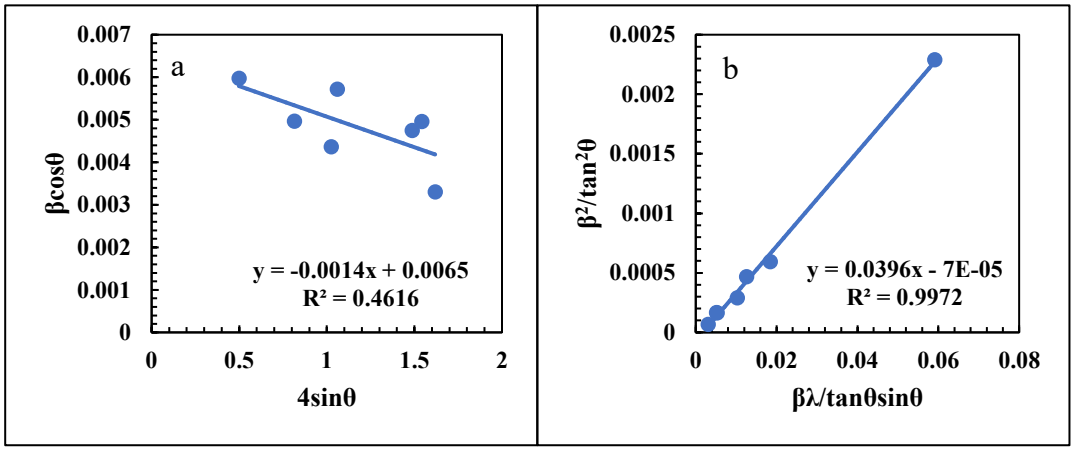

Figure A. 1: Linear fits of (a) Williamson-Hall and (b) Warren-Averbach models for $SnSe_2$-0.05% GO composite. The R^2 value for (b) is higher, suggesting Warren-Averbach is a better fit.

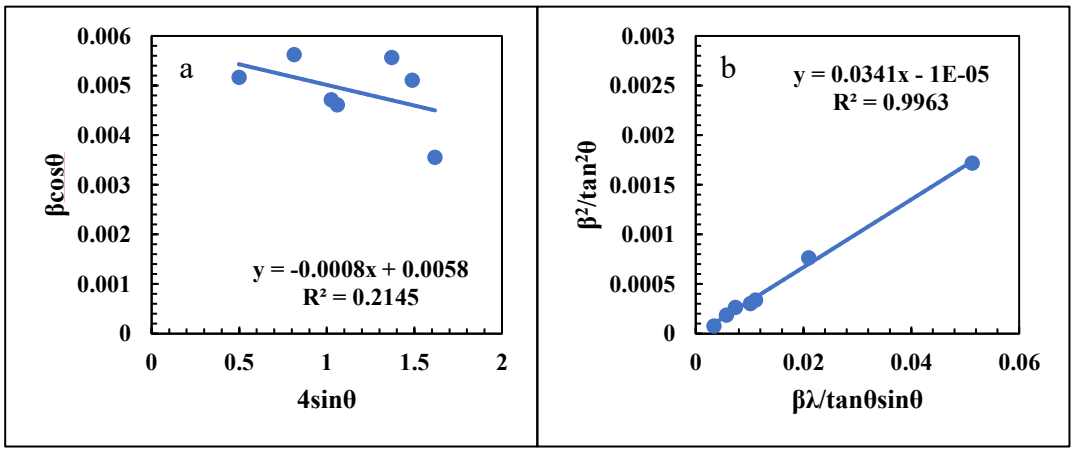

Figure A. 2: Linear fits of (a) Williamson-Hall and (b) Warren-Averbach models for SnSe2-0.10% GO composite. The R^2 value for (b) is higher, suggesting Warren-Averbach is a better fit.

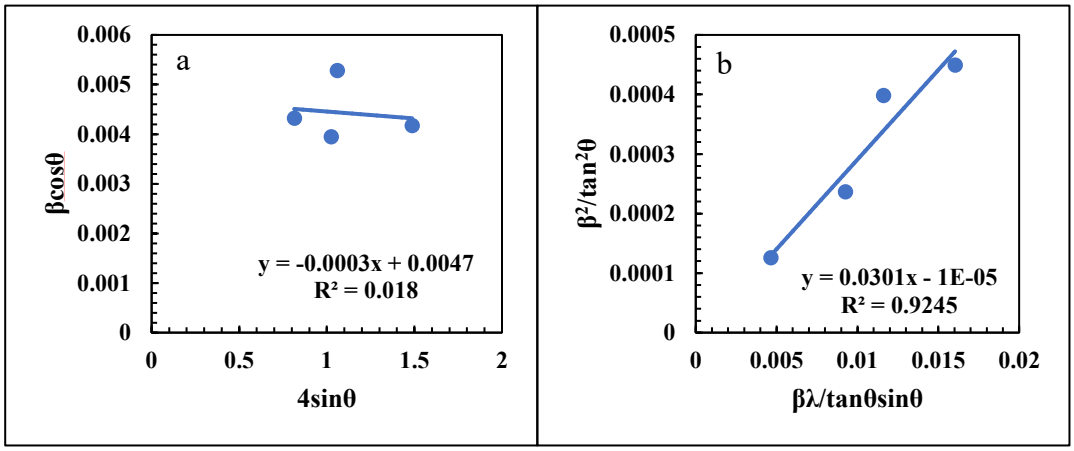

Figure A. 3: Linear fits of (a) Williamson-Hall and (b) Warren-Averbach models for SnSe2-0.25% GO composite. The R^2 value for (b) is higher, suggesting Warren-Averbach is a better fit.

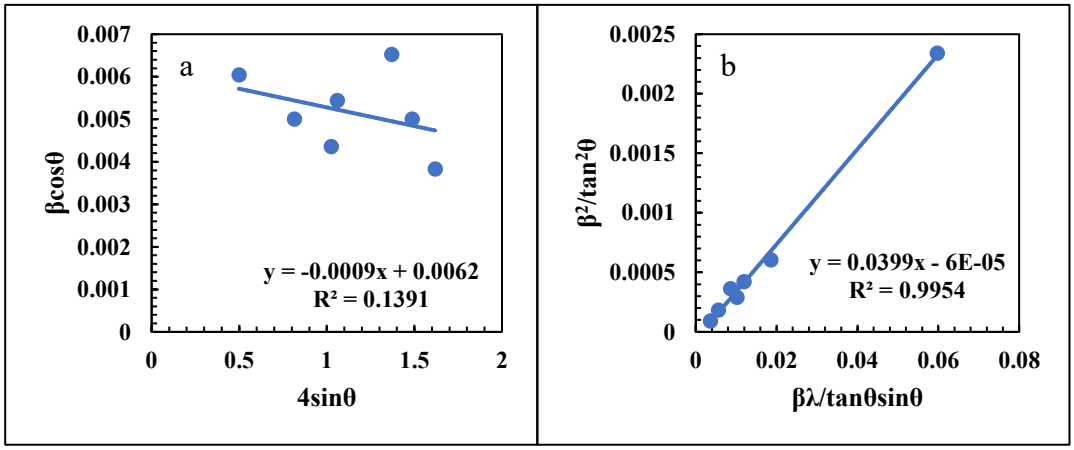

Figure A. 4: Linear fits of (a) Williamson-Hall and (b) Warren-Averbach models for SnSe2-0.25% GO composite. The R^2 value for (b) is higher, suggesting Warren-Averbach is a better fit.

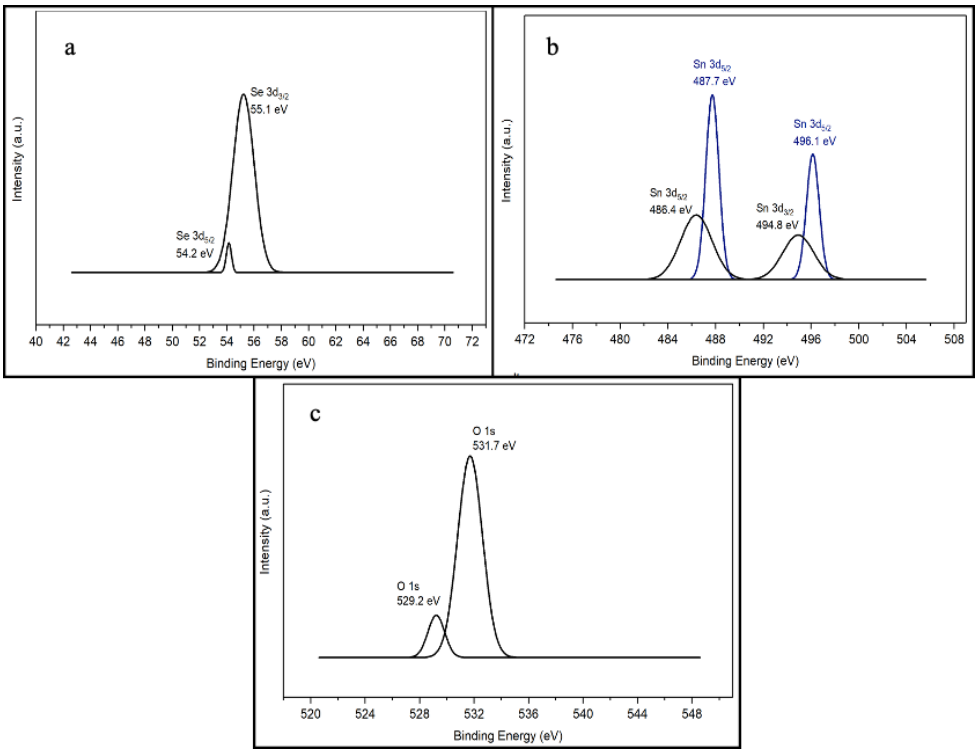

Figure A. 5: $SnSe_2$-0.05% GO: XPS spectra of (a) Se 3d, (b) Sn 3d, and (c) O 1s

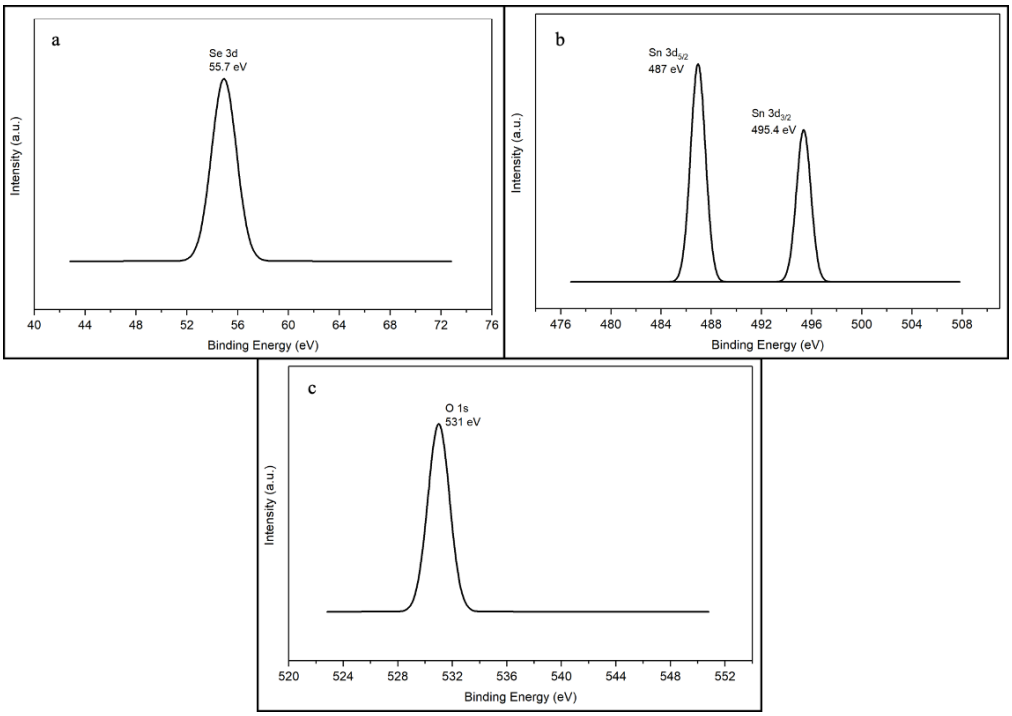

Figure A. 6: $SnSe_2$-0.10% GO: XPS spectra of (a) Se 3d, (b) Sn 3d, and (c) O 1s

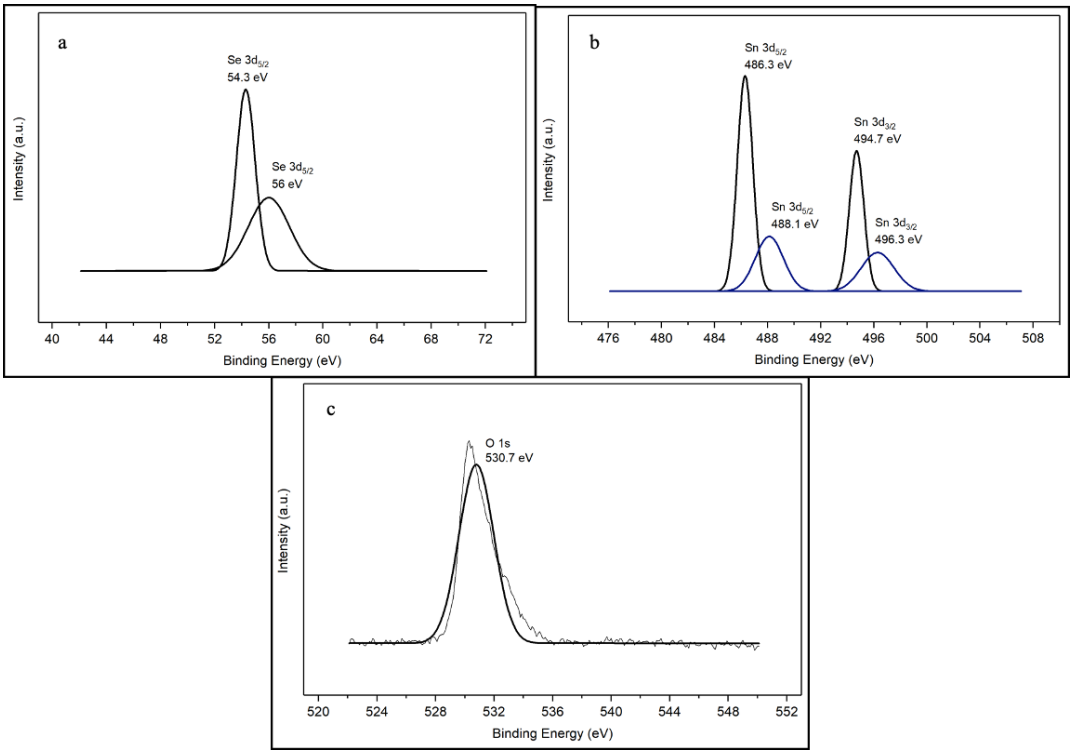

Figure A. 7: $SnSe_2$-0.25% GO: XPS spectra of (a) Se 3d, (b) Sn 3d, and (c) O 1s

Appendix A.2

This section provides additional details for the bismuth telluride analyses.

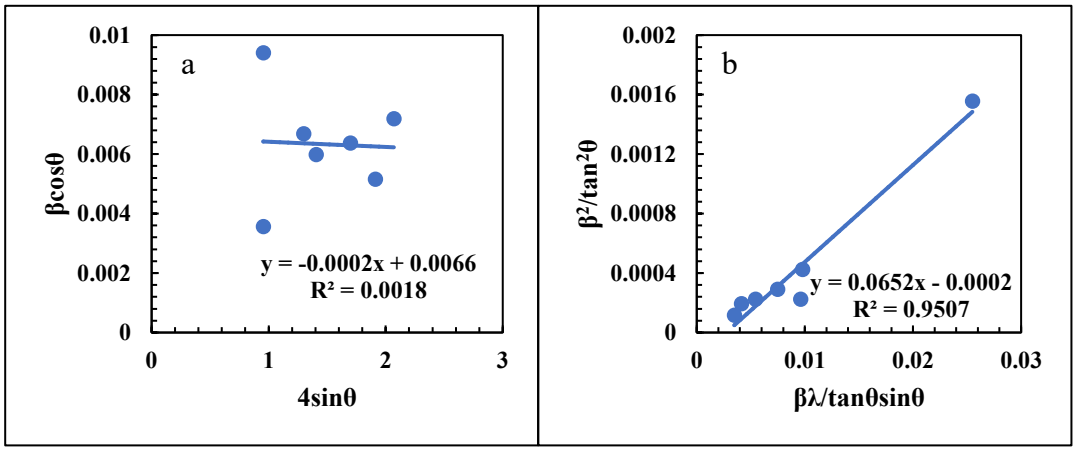

Figure A. 8: Linear fits of (a) Williamson-Hall and (b) Warren-Averbach models for Ag-doped Bi_2Te_3. The R^2 value for (b) is higher, suggesting Warren-Averbach is a better fit.

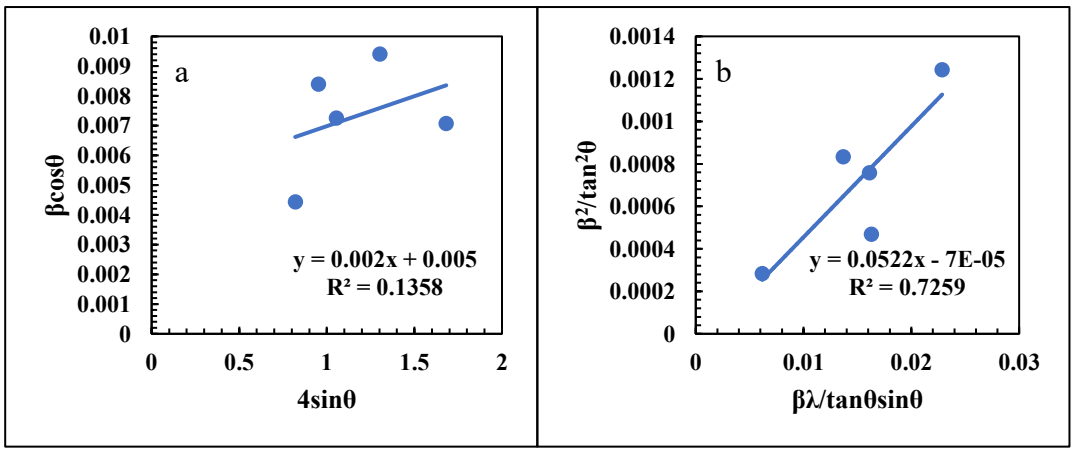

Figure A. 9: Linear fits of (a) Williamson-Hall and (b) Warren-Averbach models for Bi_2Te_3-0.25% GO. The R^2 value for (b) is higher, suggesting Warren-Averbach is a better fit.

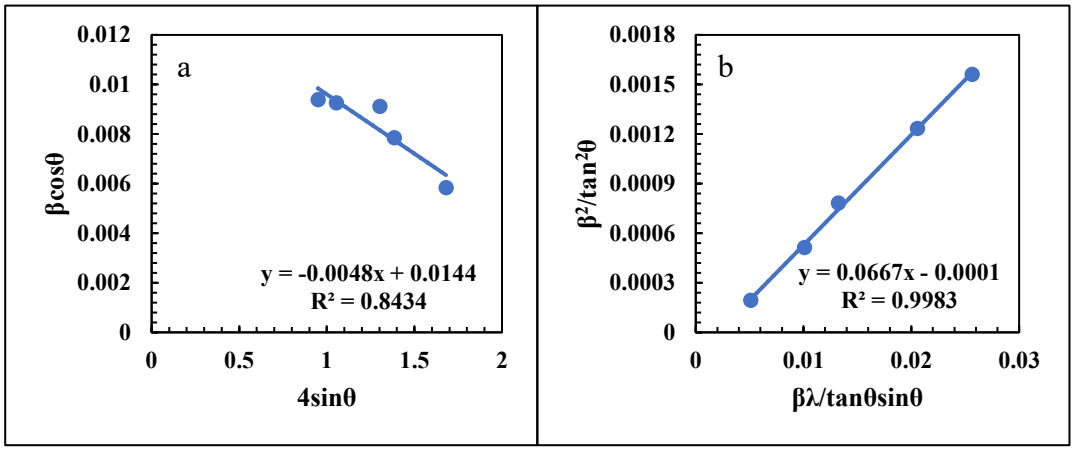

Figure A. 10: Linear fits of (a) Williamson-Hall and (b) Warren-Averbach models for Bi_2Te_3-0.50% GO. The R^2 value for (b) is higher, suggesting Warren-Averbach is a better fit.

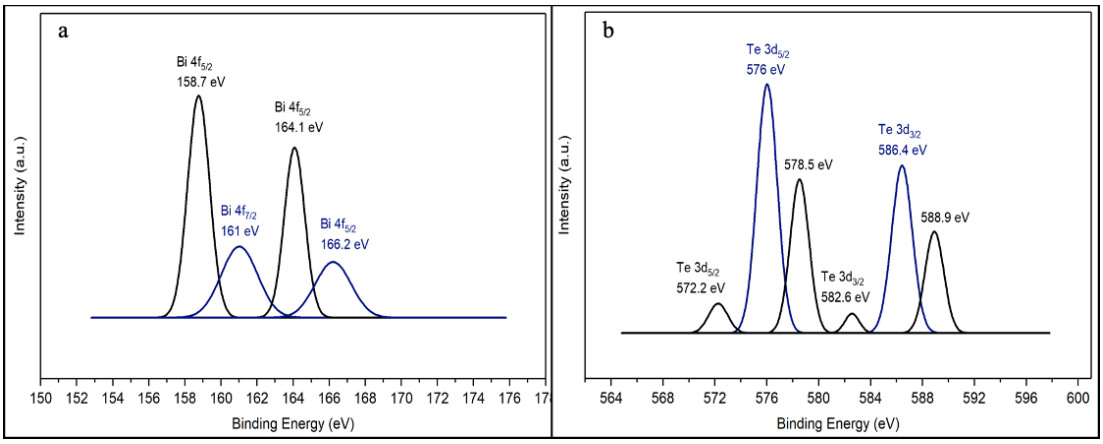

Figure A. 11: XPS analysis of Bi_2Te_3-0.50% GO (a) Bi 4f scan, (b) Te 3d scan